Facile Synthesis and Characterization of $SnO_2/Bi_5Nb_3O_{15}$/Polyaniline Nanocomposite for Supercapacitor Application

Niguss Awoke Kassie

A Dissertation Submitted to the Department of Applied Physics
College of Applied Natural Science

Presented in Partial Fulfillment of the Requirement for the Degree
of Doctor of Philosophy in Applied Physics
(Material Physics)

School of Graduate Studies
Adama Science and Technology University

January, 2026
Adama, Ethiopia

Facile Synthesis and Characterization of $SnO_2/Bi_5Nb_3O_{15}$/Polyaniline Nanocomposite for Supercapacitor Application

Niguss Awoke Kassie
Supervisor: Dr. Fekadu Tolessa (Ph.D)
Co-Supervisor: Dr. Gashaw Beyene (Ph.D)

A Dissertation Submitted to the Department of Applied Physics
College of Applied Natural Science

Presented in Partial Fulfillment of the Requirement for the Degree
of Doctor of Philosophy in Applied Physics
(Material Physics)

School Graduate Studies
Adama Science and Technology University

January, 2026
Adama, Ethiopia

DECLARATION

I hereby declare that this PhD Dissertation entitled "**Facile Synthesis and Characterization of SnO_2/$Bi_5Nb_3O_{15}$/Polyaniline Nanocomposite for Supercapacitor Application "** is my original work and has not been submitted the award of any academic degree, diploma or certificate in any other university. All sources of material used for this dissertation have been duly acknowledged through appropriate citations.

(Name of Candidate)	Signature	Date

RECOMMENDATION OF SUPERVISORS

We, the supervisors of this dissertation, hereby certify that we have read and revised the dissertation entitled "**Facile Synthesis and Characterization of SnO_2/$Bi_5Nb_3O_{15}$/Polyaniline Nanocomposite for Supercapacitor Application**" prepared under our guidance by **Niguss Awoke Kassie** submitted in partial fulfillment of the requirements for the degree of Doctor of Philosophy in Applied Physics. Therefore, we recommend the submission of the dissertation to the department for further review and defense.

Supervisor	Signature	Date
Co-Supervisor	Signature	Date

APPROVAL SHEET

We hereby certify that the recommendations and suggestions made by the board of examiners are appropriately incorporated into the final version of the dissertation entitled "**Facile Synthesis and Characterization of SnO_2/$Bi_5Nb_3O_{15}$/Polyaniline Nanocomposite for Supercapacitor Application**" by Niguss Awoke Kassie.

Main Supervisor	Signature	Date
Co-Supervisor	Signature	Date

We, the undersigned, members of the Board of Examiners of the dissertation open defense by **Niguss Awoke Kassie** have read and evaluated the dissertation entitled "**Facile Synthesis and Characterization of SnO_2/$Bi_5Nb_3O_{15}$/Polyaniline Nanocomposite for Supercapacitor Application**" and examined the candidate during open defense. This is, therefore, to certify that the dissertation is accepted for partial fulfillment of the requirement of the degree of Doctor of Philosophy in Applied Physics (Material Physics).

Chairperson	Signature	Date
External Examiner 1	Signature	Date
External Examiner 2	Signature	Date
Internal Examiner 1	Signature	Date
Internal Examiner 2	Signature	Date

Finally, approval and acceptance of the dissertation is contingent upon submission of its final copy to the School of Graduate Studies (SGS) through the candidate's Department Graduate Council (DGC) and College Graduate Committee (CGC).

Department Head	Signature	Date
College Dean	Signature	Date
School of Graduate Studies, Dean	Signature	Date

ACKNOWLEDGMENTS

First and foremost, I give all glory, honor, and praise to the Almighty God, whose grace, wisdom, and unfailing love continue to guide me throughout my Ph.D journey. His blessings and strength have sustained me at every stage of my research and academic pursuit.

Next, I would like to express my deepest gratitude to my supervisors, Dr. Fekadu Tolessa and Dr. Gashaw Beyene, for their ongoing guidance, encouragement, and insightful advice during my study. Their patience, expertise, and commitment are invaluable in shaping my research and professional development.

I am sincerely thankful to Adama Science and Technology University, where I am currently pursuing my Ph.D. program and to Mizan Tepi University for granting me the opportunity to undertake my doctoral studies. I also wish to acknowledge the staff members of the Applied Physics Department at Adama Science and Technology University for their support, encouragement, and assistance throughout my academic journey.

I am deeply grateful to Dr. Mesfin Asfaw for his exceptional support and commitment in helping me obtain the scholarship for my research work at the University of Nigeria. His continuous encouragement and efforts played a vital role in making this opportunity a reality, and I sincerely appreciate his contribution to my academic journey.

I would like to thank also Dr. Girum Ayalneh, Addis Ababa University, Coordinator of the ESIMSAD program, for his valuable support and assistance, particularly in facilitating my travel to Nigeria, which significantly contributed to this work.

Furthermore, I extend my profound appreciation to the University of Nigeria, where I carried out part of my experimental work, and to Prof. Fabian I. Ezema, Prof. Paul Ejikeme, and Dr. Chinwe for their invaluable assistance, technical guidance, and warm hospitality during my stay. Their contributions have greatly enriched my research progress and academic experience. I am also grateful to the Electrochemical Science and Innovative Materials for Sustainable Africa Development (ESIMSAD) program for its financial support and for facilitating the collaboration with the University of Nigeria, which greatly enhanced the success of my experimental research.

My heartfelt appreciation also goes to my beloved family, my wife Mingzem Mengistu, my children Yordanos, Dawit, Luelseged, my father Awoke Kassie and my mother Minbiyew Zeleke, and also my brothers and sisters, for their unconditional love, patience, and constant support. They have been my greatest source of motivation and strength throughout this journey.

TABLE OF CONTENTS

LIST OF TABLES

LIST OF FIGURES

ABBREVIATIONS AND ACRONYMS

AC	Activated Carbon
APS	Ammonium Peroxydisulfate
ASC	Asymmetric Supercapacitor
CE	Counter Electrode
CV	Cyclic Voltammetry
CNTs	Carbon Nanotubes
CPE	Constant Phase Element
D. Water	Distilled Water
EDLCs	Electric Double Layer Capacitors
EDX	Energy Dispersive X-ray
EES	Electrochemical Energy Storage
ECs	Electrochemical Capacitors
Eg	Energy Band gap
EIS	Electrochemical Impedance Spectroscopy
ESR	Equivalent Series Resistance
FTIR	Fourier Transform Infrared Spectroscopy
FWHM	Full Width at Half Maximum
GCD	Galvano Charge-Discharge
HR-TEM	High Resolution Transmission Electron Microscopy
JCPDs	Joint Committee on Powder Diffraction
NPs	Nanoparticles
PANI	Polyaniline
PVDF	Polyvinylidene Difluoride
PC	Pseudocapacitor
RE	Reference Electrode
SAED	Selected Area Electron Diffraction
SCs	Supercapacitors
SEM	Scanning Electron Microscopy
TEM	Transmission Electron Microscopy
WE	Working Electrode
XRD	X-ray Diffraction

ABSTRACT

This Ph.D. dissertation investigates the ternary SnO_2/$Bi_5Nb_3O_{15}$/PANI nanocomposites, which were developed and evaluated for their potential as advanced electrode materials for supercapacitor applications. SnO_2 and $Bi_5Nb_3O_{15}$ (BNO) nanoparticles were synthesized using an environmentally friendly method, while polyaniline (PANI) was synthesized through chemical polymerization. The fabrication of both binary and ternary composites were carried out using ultrasonication with optimized mass proportions. SnO_2-based composites suffer from poor ion transport, volume changes, and low conductivity. To overcome these issues, a novel SnO_2/BNO/PANI ternary nanocomposite was developed via a simple and eco-friendly synthesis by integrating BNO and the conducting polymer PANI to SnO_2. XRD analysis confirmed the formation of tetragonal SnO_2 and orthorhombic BNO phases, and also presence of PANI in the binary, and ternary nanocomposites did not alter their crystal structures. FTIR analysis confirmed the binding of PANI to the synthesized pristine nanoparticle and nanocomposites surfaces, while TEM imaging displayed well-integrated nanostructures. Electrochemical performance was investigated in 1 M H_2SO_4 electrolyte using cyclic voltammetry, galvanostatic charge-discharge, and electrochemical impedance spectroscopy, revealed a significant enhancement in performance due to the incorporation of PANI. The SnO_2/BNO/PANI electrode achieved an impressive specific capacitance of 424 $F.g^{-1}$ at a scan rate of 5 $mV.s^{-1}$, outperforming as compared to SnO_2, BNO, SnO_2/BNO, and SnO_2/PANI electrodes. Asymmetric supercapacitors (ASCs), utilizing activated carbon (AC) as the negative electrode, demonstrated exceptional device-level performance. The AC//SnO_2/BNO/PANI, AC//SnO_2/PANI-30%, and AC//BNO/PANI-30% devices provided specific capacitances of 247.52 $F.g^{-1}$ at 0.2 $A.g^{-1}$, 237.38 $F.g^{-1}$ at 0.3 $A.g^{-1}$, and 475.44 $F.g^{-1}$ at 0.1 $A.g^{-1}$, respectively. The corresponding long-term cycling tests of these devices were confirmed remarkable stability with average Coulombic efficiencies of 98.76% at 2 $A.g^{-1}$, 99.85% at 1 $A.g^{-1}$ and 100% at 1 $A.g^{-1}$, after 5000, 2000, and 5000 cycles, respectively. Additionally, the ternary nanocomposite exhibited capacitance retention of up to 73.03% after 5000 cycles. Overall, this dissertation demonstrates that the synergistic integration of SnO_2, BNO, and PANI enhances specific capacitance, energy, and power density, confirming that the facile-synthesized SnO_2/BNO/PANI ternary nanocomposite is a promising and durable electrode material for high-performance supercapacitors.

KEYWORDS: Bismuth Niobate, Energy storage, Nanocomposite, Polyaniline, Supercapacitors, Tin Dioxide, Vernonia amygdalina

CHAPTER 1

INTRODUCTION

1.1 Background of the Study

The history of energy storage devices dates back to the early 19^{th} century with the invention of the voltaic pile by Alessandro Volta in 1800, which marked the first true battery capable of producing a steady electric current (De Santillana, 1965). Over time, advancements in electrochemistry led to the development of various types of batteries, including lead-acid (1859), nickel-cadmium (1899), and lithium-ion (1991) systems, each improving upon energy density, rechargeability, and lifespan (Rand, 1997). These innovations have played a crucial role in powering industrial, transportation, and electronic technologies, yet the growing demand for rapid energy delivery and long cycle life has driven the search for alternative storage systems (Karthikeyan et al., 2021).

In recent times, the global energy crisis has intensified due to the low reserves of fossil fuels and the increasing issues of environmental pollution. The rapid expansion of the global economy, coupled with population growth, has led to a significant rise in energy consumption, further intensifying the problem. These challenges have created an urgent need to explore clean, renewable energy resources alongside high-performance energy storage solutions that are environmentally friendly, efficient, and sustainable. Consequently, both academic and industrial researchers are increasingly focusing on the development of stable, efficient, and flexible energy storage devices, as well as advanced energy conversion technologies (Asaithambi et al., 2021; Ginley et al., 2008). Addressing the challenges of energy storage is now recognized as a critical step in mitigating global warming and ensuring the stability of power systems worldwide. Recently, substantial efforts have been made to create new energy storage solutions such as supercapacitors, which offer greater energy density compared to traditional capacitors and higher power density than batteries (Cheng et al., 2011). The increasing need for modern digital communications, portable electronic devices, and hybrid electric vehicles is driving the advancement of energy conversion and storage technologies, along with electrochemical energy storage (EES) devices that possess high energy and power density (Karden et al., 2007). The intermittent nature of renewable energy sources requires advanced storage technologies to capture excess energy during peak production times and release it when needed. Modern society demands low-cost, environmentally friendly energy solutions that can support sustainable development and reduce dependence on traditional non-renewable sources like fossil fuels. The

development of high-performance energy storage devices, such as supercapacitors and batteries, is critical to meeting the growing energy demands of the 21^{st} century and ensuring a cleaner, more sustainable future (Yu & Chen, 2020). Addressing energy storage will play a pivotal role in ensuring the long-term health of the planet and the well-being of its inhabitants.

Supercapacitors have unique characteristics, such as their long life cycle, quick energy delivery capacity. Supercapacitors have attracted great research interest because they serve as a bridge between rechargeable batteries and conventional capacitors in many emerging technologies. Supercapacitors are particularly helpful for extending battery life and are utilized in a variety of applications, including heavy machinery, hybrid cars, and small-scale electronic equipment fabrication (Pipitone & Vitale, 2020). Supercapacitor has also outstanding features such as quick storage/release of energy, about one million charge/discharge life cycles, and eco-friendliness. The power density of a supercapacitor (100kW.kg^{-1}) is much higher than that of a conventional battery; however, the energy density (10 Wh.kg^{-1}) is an order of magnitude less than battery (100 Wh.kg^{-1}). The power density (specific power) and energy density (specific energy) of different energy storage or conversion technologies are given in the Ragone plot as shown in Fig. (1.1) (Saleem et al., 2016).

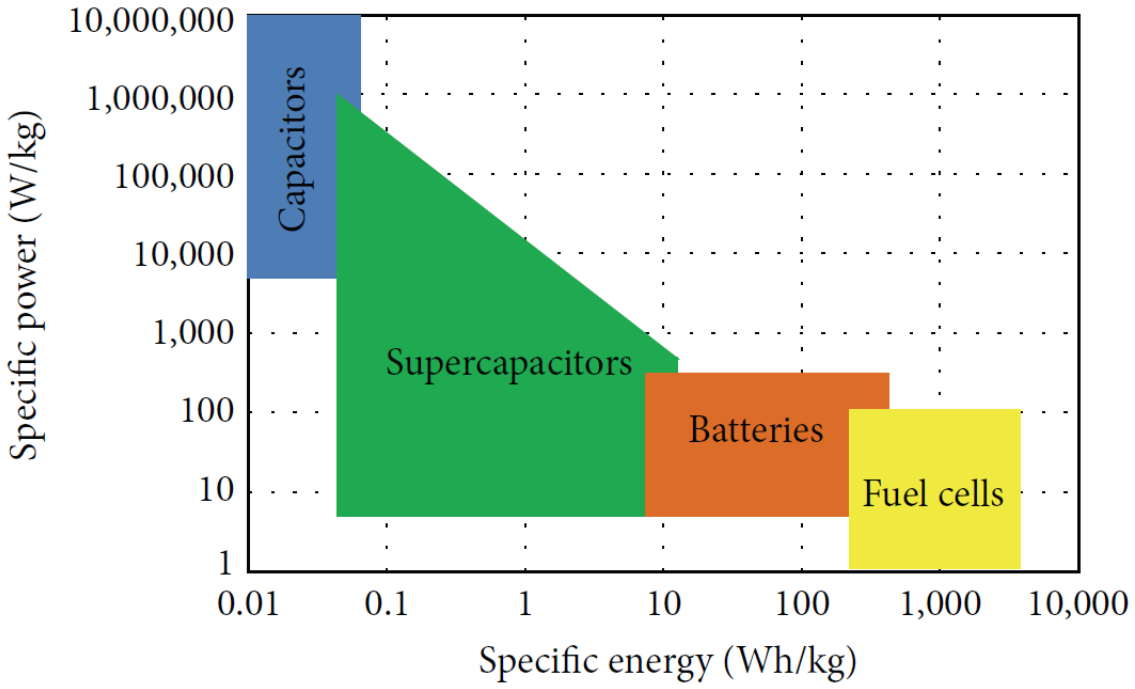

Figure 1.1: Specific energy and specific power plot of energy storage and conversion devices.

Nanotechnology significantly improves energy storage systems via a variety of methods, including greater surface area, enhanced charge transfer, and electrode stability (Vaghela et al., 2023). Nanomaterials, including nanowires, nanotubes, and nanoparticles, have a greater sur-

face area than related materials. This provides more active sites for energy storage reactions, resulting in higher energy densities and faster charging and discharging. Nanomaterials' unique features promote charge transport within energy storage devices, enhancing the efficiency and performance of batteries and supercapacitors (Alonzo et al., 2023).

Nanocomposites have emerged as promising electrode materials for supercapacitor applications due to their ability to integrate all the complementary properties of multiple components into one functional system (D. Yang, 2012). A combination of metal oxides, conductive polymers, carbon-based materials, or 2D structures in nanocomposites offers enhanced electrical conductivity, abundant electroactive sites, improved ion diffusion pathways, and increased structural stability during repeated charge/discharge cycles (Soam et al., 2025). High specific capacitance, good rate capability, and long cycling life, which cannot be achieved by individual components, are realized through the synergistic interactions between the constituents. Moreover, the nanoscale architecture of the composites offers a huge surface area with tunable porosity for effective accessibility of the electrolyte and fast redox reactions (Jariwala et al., 2023).

For energy storage applications, various synthesis methods, including chemical, physical, and green synthesis methods, have been developed to provide electrode materials with tailored structures and enhanced electrochemical characteristics. The green synthesis method is an eco-friendly, cost-effective, biocompatible, energy-efficient, and scalable approach to synthesize materials, particularly nanoparticles, using biological entities like plants (Iravani, 2011), bacteria (Bahrulolum et al., 2021), fungi (Maliszewska et al., 2014), and algae (Khan et al., 2022), or using environmentally benign chemicals and processes. This method minimizes the use of hazardous substances, reduces energy consumption, and often employs renewable resources. Green synthesis provides a sustainable alternative to traditional chemical and physical methods by using natural reducing and stabilizing agents found in plant extracts. This approach reduces the environmental impact and improves the biocompatibility and functionality of the synthesized materials. This approach is gaining attraction in various fields, including medicine, environmental science, and energy, for its potential to produce safer and more sustainable nanomaterials.

Among the various electrode materials studied, transition metal oxides are regarded as promising options because of their significant capacity stemming from pseudocapacitance (Wang et al., 2014). Metal oxides such as RuO_2, Co_3O_4, NiO (Jayakumar et al., 2024), and SnO_2 are considered as promising electrode materials in pseudocapacitors due to their high theoretical specific capacitance (Jayakumar et al., 2024). Among the different metal oxide nanomaterials, tin oxide has garnered considerable interest due to its possible use as electrode materials in energy storage systems and photo-electrochemical devices becuase of high theoretical capacity, natural abundance, cost-effective, environmental friendliness, favorable band gap, and chemically stable at

high temperatures (Abdelkader et al., 2015; Deng & Lee, 2008; Sakaushi et al., 2010). Recent developments in nanostructured SnO_2 have also enabled improved performance in supercapacitors and hybrid energy storage devices, owing to enhanced surface area and electrochemical activity at the nanoscale (Soam et al., 2020).

Bismuth-based nanomaterials have emerged as promising candidates for supercapacitor applications due to their unique electrochemical properties, high theoretical specific capacitance, and environmental benignity. Bismuth oxide has been studied for a variety of uses, such as solid oxide fuel cells (Lee et al., 2013), gas sensors (Shinde et al., 2019), catalysts (Selvamani et al., 2018), electrochemical capacitors (Chitrada & Raja, 2014), optical materials (Kaky et al., 2024), and biosensors (Shan et al., 2009), because of its non-toxic and biocompatible properties, wide band gap, high refractive index, and strong oxygen ion conductivity and dielectric permittivity (Dunn et al., 2011). Among bismuth-based materials, $Bi_5Nb_3O_{15}$ (BNO) has attracted significant attention for its potential in electrochemical energy storage due to its high theoretical capacity (Li et al., 2022; Yin et al., 2017).

Polyaniline (PANI) is one of the most thoroughly investigated electrode material for supercapacitor application. The chemical synthesis of PANI through chemical oxidation primarily involves three key reagents: an acidic medium (either aqueous or organic), aniline, and an oxidizing agent (Rahman et al., 2021). PANI in the form of emeraldine salt has strong electrical conductivity and stores energy via the EDLC (Electric Double Layer Capacitance) mechanism, but it can also store energy via the pseudocapacitor mechanism since it can oxidize and reduce under certain electrochemical conditions. PANI, polypyrrole, and polythiophene are among the most extensively researched conducting polymers (Prasanna et al., 2019). PANI is an attractive conducting polymer known for its straightforward and affordable production, as well as its stability in air and high electrical conductivity. PANI is a potential material for supercapacitor application in an advanced energy storage system because of its unique combination of high conductivity, pseudocapacitive behavior, high surface area, and chemical stability. PANI and its composite materials are utilized in various fields such as light-emitting diodes (H. Wang et al., 1996), solar cells (AbdulAlmohsin et al., 2012), gas sensors (Virji et al., 2004), memory devices, catalysis (J. Huang, 2006), and electrochemical energy storage (Navale et al., 2017; Rajkumar, 2022). Nanostructured conducting PANI possesses high surface area and porosity, hence demonstrating excellent potential in energy storage devices due to its unique properties related to conducting pathways, and surface interactions (Nwanya et al., 2014).

1.2 Statement of the Problem

Semiconducting metal oxides have demonstrated remarkable physical and chemical characteristics for energy storage applications, including a high surface area, enhanced surface reaction activity, biocompatibility, efficient electron transport, a large number of active sites, and excellent cycle stability (Dubal et al., 2017). Among the diverse range of metal oxides (such as RuO_2, MnO, NiO, Fe_2O_3, CeO_2, etc.), SnO_2 stands out as an n-type semiconductor that plays a vital role in energy storage technologies, including supercapacitors, lithium-ion batteries, fuel cells, and energy conversion devices like solar cells, due to high theoretical capacity, natural abundance, environmental friendliness, and high electrochemical activity (Deng & Lee, 2008; Sakaushi et al., 2010; Z. Zhang et al., 2014). The SnO_2 exhibits remarkable characteristics, such as a high theoretical capacity, a suitable energy band gap, high energy density, significant surface activity, abundant availability, excellent ionic conductivity, non-toxicity, affordability, and favorable electrical, optical, and electrochemical properties (Abernathy et al., 2011; Bhardwaj & Mohapatra, 2016; Trindade & Silva, 2018). There are different SnO_2-based composites to improve electrochemical energy storage activities, like SnO_2/g-C_3N_4 (R. Kumar et al., 2024; Nguyen-Dinh et al., 2021), SnO_2/ZnO (Lopa et al., 2023), grapheme-TiO_2-SnO_2 (Zamiri et al., 2022), and SnO_2/PANI (Prasanna et al., 2019) and also $Bi_5Nb_3O_{15}$-based composites like Carbon-coated@$Bi_5Nb_3O_{15}$ (Y. Li et al., 2018), and $Bi_5Nb_3O_{15}$/CeO_2 (T.-T. Wei et al., 2021), widely used for electrochemical applications. However, its practical application in a supercapacitor is hindered by several limitations, including weak ion extraction and insertion during charge/discharge cycles, substantial volume expansion, high resistivity, and poor conductivity (Asaithambi et al., 2021). To address these challenges, various approaches and strategies have been employed to improve the conductivity and electrochemical performance of SnO_2. These strategies include the addition of semiconducting metal oxides ($Bi_5Nb_3O_{15}$) introduces additional reversible redox-active sites, increasing the overall pseudocapacitance of the composite electrode (Garima et al., 2025), and highly conductive polymer (PANI) materials incorporating into SnO_2 can enhance its physicochemical properties and boost its electrochemical performance. So we developed a nanocomposite by incorporating $Bi_5Nb_3O_{15}$, and PANI polymer with SnO_2, aiming to improve the materials overall performance. In this study, a facile synthesis method was employed, which proved to be straightforward, non-toxic, cost-effective, and environmentally benign for the fabrication of nanoparticles. Prior to this work, the synthesis of SnO_2/$Bi_5Nb_3O_{15}$/PANI ternary nanocomposites for electrochemical applications had not been reported yet.

1.3 Objectives of the Study

1.3.1 General Objective

The main aim of this study is to investigate a novel ternary nanocomposite SnO_2/BNO/PANI as electrodes for supercapacitor application using a facile synthesis method.

1.3.2 Specific Objectives

The specific objectives of this study are:

- to synthesize SnO_2 and BNO nanomaterials using *Vernonia amygdalina* leaf extract
- to synthesize SnO_2/BNO, SnO_2/PANI, BNO/PANI, and SnO_2/BNO/PANI nanocomposites using ultrasonication assisted method
- to characterize the optical, structural, elemental composition, morphological, functional group of the composites using appropraite characterization tools
- to evaluate the specific capacitance of SnO_2, BNO, SnO_2/BNO, SnO_2/PANI, BNO/PANI, and SnO_2/BNO/PANI nanocomposites, by cyclic voltammetry (CV), and Galvanostatic charge-discharge (GCD).
- to determine the cyclic stability of the synthesized nanomaterials of their electrochemical performance
- to determine the supercapacitor performance of SnO_2/BNO/PANI nanocomposite using a two-electrode system.

1.4 Scope of the Study

This study is confined to the experimental synthesis, characterization, and electrochemical evaluation of SnO_2/BNO/PANI nanocomposites for supercapacitor application. The research involves the facile synthesis of SnO_2/PANI, BNO/PANI and SnO_2/BNO/PANI nanocomposites, followed by detailed structural, morphological, and electrochemical characterization. All synthesized electrodes were initially examined in a three-electrode configuration using a 1 M H_2SO_4 aqueous electrolyte. Their electrochemical performance, including cyclic stability up to 5000 cycles, was systematically assessed. Based on the highest specific capacitance values obtained in the three-electrode setup, the best-performing composites SnO_2/PANI-30%, BNO/PANI-30% as well as the ternary composite, were evaluated for further investigation in a two-electrode system, which better reflects practical device performance. The potential window for the two-electrode

measurements was limited to 0.9V for BNO/PANI-30%, and 1.4V for both SnO_2/PANI-30% and the ternary (SnO_2/BNO/PANI) nanocomposite. The scope of the study is restricted to only experimental work, acidic aqueous electrolyte, and does not include theoretical modeling, long-term aging beyond the performed stability tests. The focus remains on optimizing material composition and electrochemical configuration to develop efficient, environmentally friendly, and cost-effective energy storage materials.

1.5 Significance of the Study

This study on the facile synthesis and characterization of SnO_2/BNO/PANI nanocomposite for supercapacitor applications holds substantial environmental and technological importance. By employing green, sustainable synthesis approaches, the research minimizes environmental impact by using eco-friendly, cost-effective, and biocompatible materials and processes. The resulting nanocomposite is expected to exhibit enhanced electrochemical properties, including high specific capacitance, excellent cyclic stability, and efficient charge transport, which are essential for the development of next-generation energy storage devices. Furthermore, this work contributes valuable insights into the design of environmentally sustainable supercapacitor materials, supporting global efforts toward renewable and clean energy technologies. It also serves as a useful reference and foundation for future research focused on facile, green synthesis methods for advanced energy storage systems.

1.6 Organization of the Dissertation

This dissertation investigates the electrochemical properties of various nanomaterials, including pristine SnO_2 and BNO, as well as their binary (BNO/PANI, SnO_2/PANI, SnO_2/BNO) and ternary (SnO_2/BNO/PANI) nanocomposites, with a focus on their potential applications in supercapacitors. The dissertation is structured to guide the reader through the progression of the research. Chapter 1 provides an overview of the study, outlining the background, problem statement, research questions, and objectives, along with a roadmap of the dissertation organization. Chapter 2 presents a detailed review of relevant literature, covering energy storage mechanisms in metal oxides and conductive polymers, synthesis techniques for nanomaterials, and recent advancements in binary and ternary composites for supercapacitor applications. Chapter 3 outlines the experiment methodology, including the green synthesis of pristine SnO_2 and BNO, chemical synthesis of PANI, and the preparation of the binary and ternary nanocomposites. It also details the electrode fabrication process and the procedures used for material characterization and electrochemical testing. Chapter 4 presents and discusses the results, including structural, morphological, compositional, and optical characterization of the synthesized materials. It fur-

ther explores the electrochemical behavior of each sample, both in three-electrode systems and in fabricated asymmetric supercapacitor (ASC) devices. Special attention is given to analyzing the specific energy and power densities of the assembled devices, highlighting the improved performance of the ternary SnO_2/BNO/PANI composite. Finally, Chapter 5 summarizes the key findings of the research, concluding that the developed nanocomposites, especially the ternary SnO_2/BNO/PANI, exhibit promising characteristics for energy storage applications. As a recommendation, future research should explore the photocatalytic potential of these nanomaterials, particularly their application in the degradation of organic pollutants in wastewater, due to their suitable band gap structures and surface reactivity.

CHAPTER 2

REVIEW OF RELATED LITRATURE

2.1 Energy Storage Devices

The growing environmental concerns associated with the continuous use of non-renewable energy resources and the increasing complexity of power distribution networks have accelerated the global shift toward renewable and sustainable energy sources, such as wind and solar. However, the intermittent nature of these resources needs effective management of their varying power output. Consequently, the development of advanced energy storage devices capable of delivering energy on demand has become a key focus (San Martin et al., 2011). Currently, energy storage systems are applied across various large-scale sectors and are broadly categorized into four main types: mechanical, chemical, electrical, and electrochemical. Among these, mechanical storage through pumped hydroelectric systems remains the most established method. Nevertheless, electrochemical energy storage (EES) systems particularly electrochemical capacitors (ECs) and batteries have shown remarkable potential for powering portable electronic devices and supporting the electrification of transportation (Sagadevan et al., 2021). This is primarily due to their high round-trip efficiency, long cycle life, versatility with diverse chemistries based on inexpensive and recyclable materials, and relatively low maintenance requirements (Choudhary et al., 2016; Du et al., 2017). Additionally, advanced energy storage technologies, like batteries and supercapacitors, play a crucial role in storing renewable energy for times when the primary sources are not available, ensuring a stable and reliable energy supply (L. Liu et al., 2025). Consequently, a wide range of electrochemical energy storage technologies, including batteries, supercapacitors (SCs), and fuel cells, are currently undergoing extensive research. Energy storage devices, such as batteries, supercapacitors, and fuel cells, are composed of various components that work together to store and release energy. (B.-H. Xiao et al., 2024).

2.2 Types of Supercapacitors

Electrochemical capacitors (ECs), also known as supercapacitors (SCs), have attracted a lot of interest from a variety of new EES technologies due to their high-rate capability, high coulombic efficiencies, high power density, rapid charging and discharging, long-life stability, and safe operation (G. Yu et al., 2013; L. L. Zhang et al., 2010). Unlike a battery, a supercapacitor immediately accumulates and stores charges, eliminating energy expenditure during energy conversion. The specific capacitance of the supercapacitive electrode materials can be readily increased by

increasing the surface area of the electrode materials (Veerakumar et al., 2020). Supercapacitor (SC) was divided into three groups based on the mechanism of energy storage, as shown in Fig. 2.1, and Fig. 2.2(b).

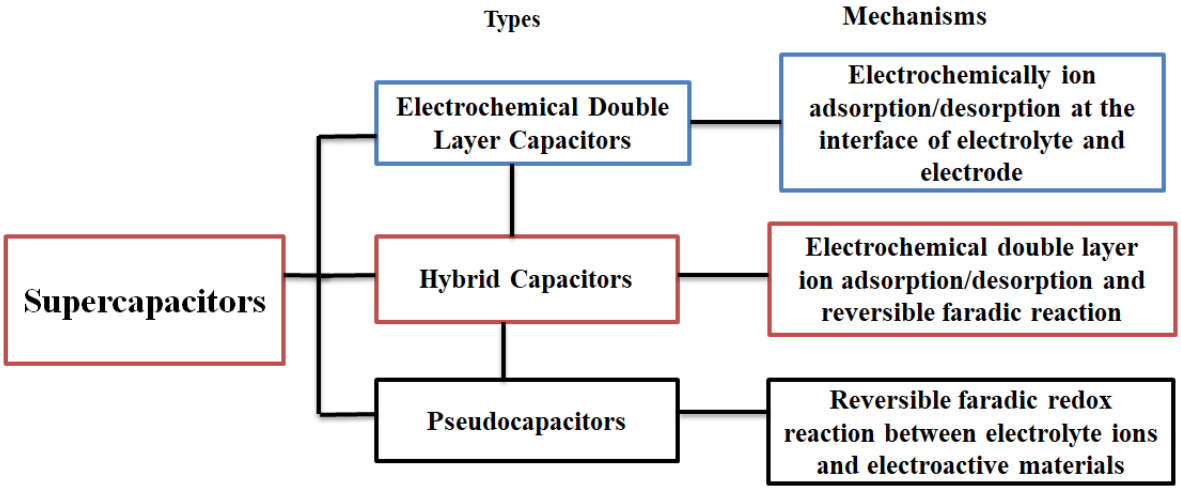

Figure 2.1: Illustration of types of supercapacitors based on the mechanism of energy storage.

Electric double-layer capacitors (EDLCs) and pseudocapacitors are the two groups into which supercapacitors are divided according to the energy storage mechanism they exhibit (Obodo et al., 2021).

2.2.1 Electric Double-Layer Capacitors (EDLCs)

EDLCs store energy through ion adsorption and the interaction of polar solvent molecules or ions with the electrode material and electrolyte in a non-faradaic process, involving electron accumulation without chemical reactions, as shown in Fig.2.2(c). These capacitors, typically made from porous carbon, are known for their cycle stability and long lifespan, with electrostatic interaction being the primary mechanism of energy storage (Nasir & Mohammad, 2020; Sk et al., 2023). The operating principle of an EDLC relies on charges that are stored electrostatically. The essential formula applicable to all capacitors is expressed as

$$C = \frac{\varepsilon_o \varepsilon_r A}{d}. \tag{2.1}$$

In this equation, A represents the electrode surface area; ε_o denotes the permittivity of free space; ε_r indicates the relative permittivity of the dielectric material, and d is the separation between two electrodes with opposite biases.

Based on the core relation presented in Eq. 2.1, the capacitance of a conventional capacitor can

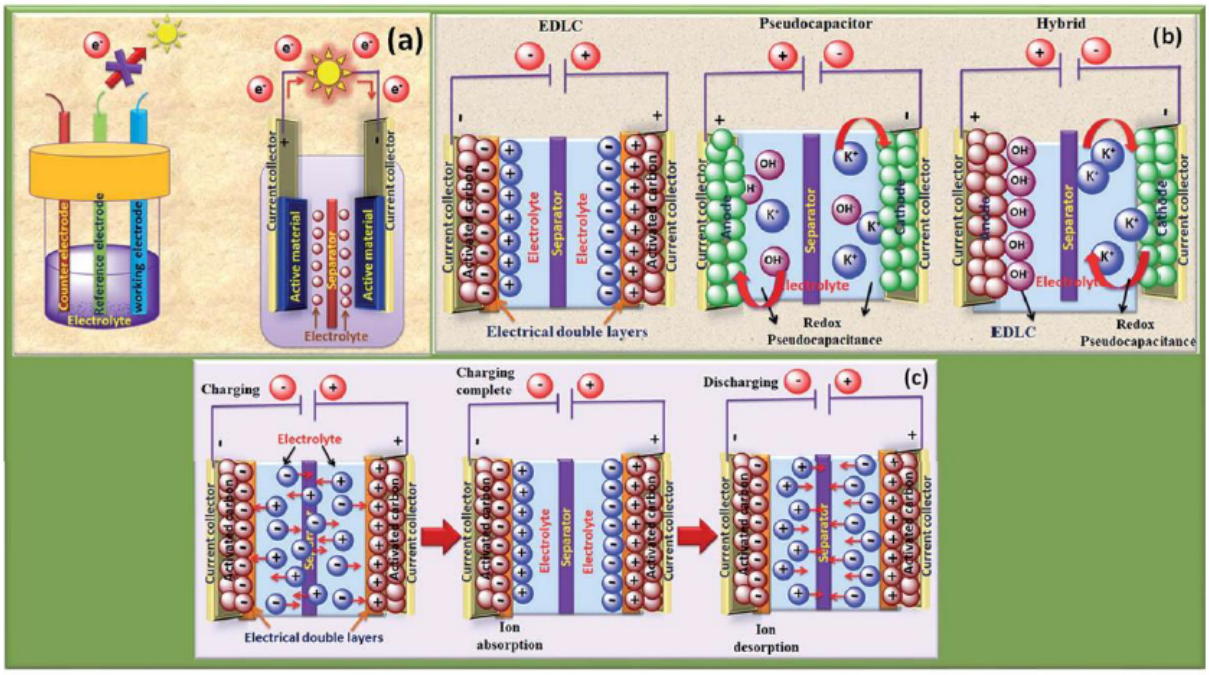

Figure 2.2: (a) illustration of the three- and two-electrode configurations, (b) Supercapacitor types: EDLC, pseudocapacitor, and hybrid, (c) Charge storage process in EDLCs and ion absorption and desorption on the surface (Jalal et al., 2021; Lokhande et al., 2020).

be enhanced by increasing the dielectric constant of the material, enlarging the surface area, and reducing the thickness between the plates. Nevertheless, achieving such enhancements requires further alterations to the material system and the design of the capacitor. For example, one might reduce the particle size to the sub-nanometer range, where quantum confinement effects are nearly attained. This adjustment results in the material exhibiting remarkable electrochemical performance.

Alternatively, doping with metal ions such as Fe, Mn, Cr, and Co can enhance the electrical conductivity of the electrode material, which in turn boosts the capacitance, relevant to capacitor design. For example, a supercapacitor featuring symmetric electrodes or operating based on faradaic reactions can ultimately demonstrate improved electrochemical performance. In essence, the faradaic process takes place in accordance with Faraday's law, indicating that charge transfer occurs at the electrode-electrolyte interface. In contrast, the subsequent non-faradaic process does not adhere to Faraday's law; here, charge transfer is absent, as seen in phenomena like adsorption-desorption at the electrolyte-electrode interface and the reorientation of solvent dipoles. For instance, the charging and discharging cycles exhibit a high degree of reversibility due to their non-faradaic electrical mechanism (P. Sharma & Bhatti, 2010). This characteristic contributes to remarkable cycling stability, allowing for up to 106 cycles or more, alongside a

rapid charging and discharging rate, with minimal degradation. A main limitation of EDLCs is found in the restricted range of electrode materials available, as EDLC devices need to utilize electrodes with high conductivity. However, this limitation can be addressed through the recent advancements in ionic conductive electrolytes (Simon et al., 2013). Carbon-based materials commonly used for EDLC devices include carbon nanotubes, graphene, activated carbon, and reduced graphene oxide.

Graphene and Carbon Nanotubes (CNTs)

Graphene represents a unique form of graphite, characterized by a single layer of carbon atoms with atomic thickness. Its remarkable electrical and mechanical attributes contribute to its widespread use, produced through various fabrication methods (Davies & Yu, 2011). Additionally, its capacity to incorporate diverse functional groups into its framework enables it to exhibit a broad spectrum of electrical and mechanical characteristics. Graphene facilitates the creation of flexible structural forms across dimensions 0D, 1D, 2D, and 3D, allowing for precise tuning of surface area and enhancing the desired structural properties. This material stands out due to its exceptional electrical and thermal conductivity, impressive mechanical strength, and robust chemical stability. Integrating these properties into developed supercapacitors would enhance their performance, providing high power density, rapid charge/discharge rates, and extended life cycle efficiency (Niu et al., 2020).

Activated Carbon (AC)

In supercapacitors, activated carbon is used because it has a high surface area, good electrical conductivity, is available, and does not cost too much. It is a three-dimensional porous material with a high specific surface area and excellent electronic conductivity at low cost. Electric Double Layer Capacitor (EDLC) devices using activated carbon electrodes manifest excellent electrochemical performance not only because of the large surface area but also due to the oxidative nature of the material (Endo et al., 2001).

2.2.2 Pseudocapacitors

Pseudocapacitors store energy by fast and reversible charge transfer reactions at or near the electrode-electrolyte surface, leading to pseudocapacitance. Pseudocapactors use oxides and conductive polymers to store energy through fast, reversible redox electrochemical processes, resulting in higher specific capacitance per unit of electrode surface area or mass. The Faradaic mechanism, which involves the transfer of charge between the electrolyte and electrode, is like

oxidation-reduction reactions. The reduction and oxidation that occur on the electrode material, which includes the charge transfer across a double layer when a voltage is applied to the pseudocapacitor, result in the Faradic current passing through an SC cell (S.-M. Chen et al., 2014; Choi & Yoon, 2015). Pseudocapacitors can also achieve higher specific capacitance and energy densities than EDLCs because of the Faradic mechanism they use. These capacitors are classified as faradaic, as they engage in redox reactions, meaning that charge transfer takes place between the electrolyte and the electrode. The majority of electrode materials used in this type of capacitor consist of metal oxides, metal-doped carbon, and conductive polymers. Nevertheless, pseudocapacitors tend to have a shorter lifespan and lower power density. These outcomes are attributed to the redox reactions occurring within the capacitors (D. Wei Kumar et al., 2025).

Conducting Polymer Pseudocapacitors

Apart from carbon-based materials and metal oxides, conducting polymers (CPs) present numerous benefits as electrode materials for supercapacitors. These benefits encompass high electrical conductivity when doped, a broad operating potential range, and the ability to adjust redox activity through chemical alterations. Additionally, many CPs are economically viable and environmentally friendly. The mechanism for charge storage in conducting polymers primarily involves faradaic processes, characterized by reversible redox reactions that occur throughout the material's bulk rather than being restricted to the surface (Roohi et al., 2024). During the oxidation phase, ions from the electrolyte are integrated into the polymer backbone, while the reduction phase leads to the release of ions back into the electrolyte. This intrinsic redox activity enables CP-based electrodes to attain higher capacitance values than those based solely on electrostatic storage methods. As charging and discharging happen without substantial structural degradation, these processes exhibit a high level of reversibility, enhancing their rate capability. Depending on the nature of ion insertion, conducting polymers can become either positively or negatively charged. The electrical conductivity of CPs varies during redox transitions, with oxidation resulting in the formation of positively charged (p-type) polymers due to the generation of delocalized π-electrons along the polymer chain. In contrast, reduction produces negatively charged (n-type) polymers. Notable examples include polyaniline (PANI), polythiophene (PTh), and polypyrrole (PPy), along with their derivatives (Hong et al., 2020). In the context of supercapacitor applications, p-doped PANI and PPy are favored, as their n-doped forms typically demonstrate subpar stability in electrolyte solutions. In p-doped CPs, oxidation leads to doping via the incorporation of ions from the electrolyte into the polymer backbone, while reduction facilitates de-doping, allowing these ions to return to the solution. The enhanced stability of p-doped polymers in comparison to their n-doped counterparts is likely attributed to diminished electronic repulsion (Peringath et al., 2023).

Metal Oxide Pseudocapacitors

Transition metallic oxides (TMOs) have been extensively investigated as materials for pseudocapacitor applications due to their various oxidation states. Transitional metal oxide materials have been identified as promising candidates for use as electrodes in energy storage devices due to their abundant reserves, environmental friendliness, ease of access, and other intriguing properties, such as diverse constituents and morphologies, large surface area, and high theoretical specific capacitance (An et al., 2019). Metal oxides exhibit great specific capacitance because they present lower resistances in ion transport. Transition metal oxides, such as RuO_2 , MnO_2 (Lei & Chen, 2015), Mn_3O_4 (Zhu et al., 2020), NiO (Sun et al., 2019), Co_3O_4 , SnO_2 , ZnO, Fe_2O_3 (Gao et al., 2018; Obodo et al., 2025; Shah et al., 2025), TiO_2 (Lakra et al., 2023), V_2O_5 (D. Chen et al., 2019), CuO (Gholivand et al., 2015), and WO_3 (Shinde et al., 2019), have displayed tremendous performances for supercapacitor applications by redox reactions. Among the extensively studied metal oxides is RuO_2 , which is noted for its low equivalent series resistance (ESR) and remarkably high specific capacitance. Nevertheless, its high cost in comparison to other transition metal oxides has prompted researchers to explore alternative options. Despite this, metal oxides have yet to realize their full capacitance potential. It is asserted that metal oxides can deliver substantial capacitance coupled with high energy at reduced current densities (J. Zhang et al., 2019). However, these materials are reported to contribute to the cracking of electrodes, resulting in limited short-term stability, as their pore structures cannot be modified or engineered in any way. Typically, to mitigate these issues, metal oxides are blended with carbon to create composites. Additionally, carbon-based materials are predominantly utilized as electrode materials for the development of pseudocapacitor electrodes, and their integration with nanosized transition metal oxide materials has demonstrated the potential to attain ultra-high specific capacitance. Comparing transition metallic oxide (TMO)-based electrodes to their bulk counterparts, nanostructure engineering has been shown to be a useful strategy for improving electrochemical performance (including reversible capacity/capacitance, cycling stability, and rate performance). However, single component materials that are obtained by simply engineering the nanostructure (tuning the particle size, geometric shape, and porosity) are still insufficient for ultra-stable, high energy density, and high power density supercapacitors for TMO-based electrode materials. Composite materials have been studied in order to improve the electro-capacitive performance of SCs by mixing a TMO material with another material that has complementary properties or can have synergistic effects with the host (Liang et al., 2021).

2.2.3 Hybrid Supercapacitors

Hybrid supercapacitors are devices that combine asymmetric electrodes, one with electrostatic (double-layer) capacitance and the other with electrochemical (pseudo-capacitive) activity. These

capacitors incorporate performance attributes that were previously unavailable with either type of electrode separately. Hybrid supercapacitors combine the fundamental features of pseudo-capacitors and electric double layer capacitors (EDLCs), resulting in a balanced combination of high energy density, power density, and cycling stability (Jalal et al., 2021; Lokhande et al., 2020). This particular kind of supercapacitor utilizes a combination of polarizable electrodes, which are usually made from carbon-based materials, alongside non-polarizable electrodes, like metals or conducting polymers, to accumulate electrical charges. Its functionality merges both faradaic and non-faradaic mechanisms, effectively leveraging the benefits of battery-type electrodes (faradaic) for substantial energy storage and capacitor-type electrodes (non-faradaic) for swift charge and discharge capabilities. By fusing these complementary processes, the device attains enhanced energy and power density, better cycling stability, and potentially reduced manufacturing costs in comparison to traditional electric double-layer capacitors (EDLCs) (Oyedotun et al., 2023). Furthermore, this hybrid configuration provides increased adaptability in optimizing performance for particular applications within energy storage systems. Among various supercapacitors, this particular type stands out due to its two distinct electrodes. These electrodes are engineered to operate in unison to meet the requirements for both power and energy density, with one functioning as a capacitive electrode and the other as a faradaic electrode. Typically, materials derived from carbon are utilized for the negative electrode, while the anode is composed of a metal or metal oxide. Metal electrodes are recognized for their significant intrinsic volumetric capacity, which contributes to enhanced energy densities. These capacitors possess the capability to demonstrate greater energy density and cycling stability compared to symmetric supercapacitors.

2.3 Design Strategies and Fabrication of Efficient Electrode Materials

Activated carbon, graphene, carbon nanotubes, conducting polymers, and transition metal oxides are among the most commonly utilized electrode materials. The working electrode was created by combining the active material, acetylene black, with polyvinylidene difluoride (PVDF) in a variable ratio. PVDF serves as a binder material created by the polymerization of vinylidene difluoride (Oyedotun et al., 2023). The mixture was thoroughly ground using a mortar and pestle to achieve uniform dispersion. Subsequently, 3-4 drops of N-methyl-2-pyrrolidone (NMP) were gradually added to the blend while stirring continuously overnight to obtain homogeneous slurry. The resulting paste was then coated onto a nickel or stainless steel mesh current collector and dried in an oven at 80^{o}C for 12 hrs to remove any residual solvent and ensure proper adhesion (Iro et al., 2016; Meher & Rao, 2011). The overall performance of a supercapacitor is significantly influenced by the careful selection of its key components, namely, the electrode materials, electrolyte, separator, and current collector. Each element plays a crucial

role in determining the device's efficiency, energy storage capacity, and long-term stability.

2.3.1 Separator

The separator is a crucial component in supercapacitor architecture, serving to prevent direct contact and electron transfer between the two electrodes while allowing ionic movement (Kim et al., 2015). A high-quality separator must exhibit sufficient mechanical strength to ensure device reliability and to prevent the migration of active materials over time. Poor quality separators can introduce additional internal resistance, significantly lowering cell performance and, in severe cases, may cause short circuiting of the entire device. Therefore, selecting an appropriate separator is a vital step during cell assembly (Shulga et al., 2014). An ideal separator must meet the following criteria: (I) electronically non-conductive, (II) offer excellent chemical resistance to corrosion caused by electrolytes and electrode degradation byproducts, (III) possess high ionic conductivity while maintaining strong electronic insulation, (IV) is easily wetted by the electrolyte to ensure optimal ion transport. Materials such as glass fiber, cellulose based paper, and ceramics are traditionally employed as separators. However, polymer-based separators, including polypropylene (PP), polyethylene (PE), and polypropylene carbonate, have gained widespread use due to their low cost, porous structure, and mechanical flexibility. Among these, polypropylene is the most extensively utilized, primarily due to its good electrolyte wettability and balance of performance and processability (Cholewinski et al., 2021; Czagany et al., 2024).

2.3.2 Current Collector

The current collector possesses essential characteristics, including excellent electrical and thermal conductivity, minimal contact resistance, substantial chemical and electrochemical stability, low corrosion susceptibility, compatibility with electrode materials, and a light material. The current collector plays a vital role in the operation of a supercapacitor by facilitating the flow of electrical current between the external circuit and the electrode, delivering charge from the power source to the electrode, and carrying it from the electrode to the external load (Verma et al., 2020). Additionally, it serves a secondary function of dissipating heat generated during cell operation. To perform effectively, current collectors must exhibit excellent electrical conductivity and high chemical stability within the cell environment to resist degradation caused by electrolyte exposure. In many cases, the intrinsic conductivity of the electrode's active material is insufficient, leading to increased internal resistance. This can significantly compromise the overall electrochemical performance, even if the active material itself has superior capacitive properties (H.-C. Wu et al., 2009).

To ensure effective charge transport and reliable power delivery in supercapacitor systems, high-quality electrical contacts and suitable conductive additives are essential. Commonly used cur-

rent collector materials include aluminum, copper, iron, steel, and various metal alloys, chosen for their excellent electrical conductivity and mechanical robustness. Direct coating of active materials onto current collectors can significantly enhance performance by promoting strong molecular-level contact. This reduces interfacial resistance between the active material and the collector, thereby improving overall charge transfer efficiency. Therefore, selecting a suitable current collector is essential for maintaining low resistance and ensuring long-term device reliability (Trivedi et al., 2021).

2.3.3 Electrolytes

The electrolyte is an important component in supercapacitors, as it transfers and balances charges between the two electrodes. Electrolytes significantly affect the performance of the device and have a stronger influence on how well supercapacitors work (Pal et al., 2019). The electrolytes for electrochemical supercapacitors are divided into several types, as shown in Fig.2.3. The interaction of the electrolyte and electrodes in all electrochemical processes has a major impact on the electrode-electrolyte interface state and the internal structure of active materials. The secret to high-performing and safe supercapacitive devices is the electrolyte selection (Pal et al., 2019). There is currently no ideal electrolyte that satisfies every need for electrochemical devices. Aqueous electrolyte-based supercapacitive devices, for instance, have high capacitance and conductivity but low energy density, cycling stability, and leakage issues. Ionic liquids (ILs) and organic electrolytes can function at higher voltages, although their ionic conductivity is often significantly lower. Solid-state electrolytes have poor ionic conductivity but may not have the possible leakage issue of liquid electrolytes (T. Zhang et al., 2020). The conductivity of the electrolyte affects the supercapacitor device's performance; a higher conductivity makes it simpler to move ions toward the electrode surface. The quantity of charge carriers, ionic mobility, and ion valency all affect the electrolyte's ionic conductivity (Guan et al., 2025). The electrolyte with the highest conductivity is sulfuric acid (H_2SO_4), which is followed by potassium hydroxide (KOH) (Konikkara & Kennedy, 2017). Because aqueous electrolytes have a lower viscosity than non-aqueous electrolytes, their conductivity is superior. Electrolytes are arranged as follows in increasing order of conductivity: $KOH > KCl > H_2SO_4 > Na_2SO_4$. When mixed with a solvent, a good electrolyte should dissolve easily into free ions. The electrolytes concentration can have an impact on its specific conductance. Aqueous electrolytes, being liquid-based electrolytes with low viscosity and rapid ionic conduction, perform better in energy storage than solid or semi-solid/gel electrolytes.

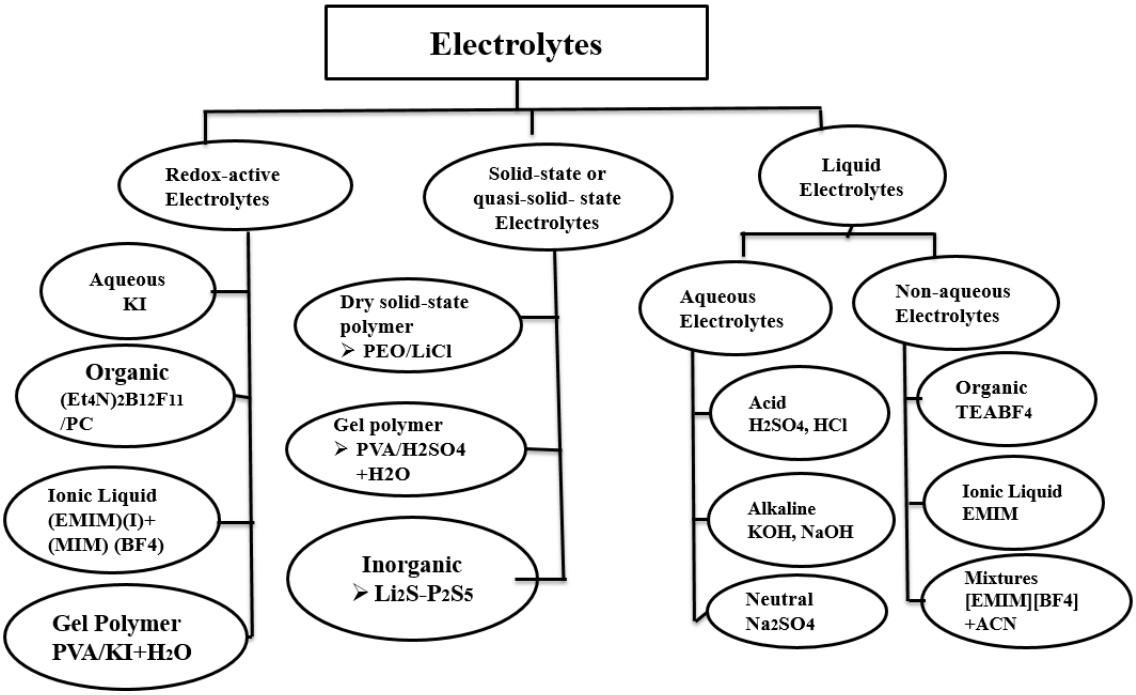

Figure 2.3: Schematic illustration of the types of electrolytes used in electrochemical supercapacitors.

2.3.4 Binder

In supercapacitors, a binder is utilized to connect active materials with conductive agents and adhere to electrode materials. The binder plays a crucial role in providing the necessary strength and appropriate pore size for the electrode material. Choosing a suitable binder is essential since it affects the electrochemical performance of supercapacitors by covering the active pores present on the electrode surfaces (Bresser et al., 2018). To achieve low contact resistance and enhanced performance, the active material is combined with conductive carbon and the binder in an optimal ratio. Below are discussions on some commonly employed binders:

Polytetrafluoroethylene (PTFE) offers excellent chemical stability attributed to its CF_2-CF_2 units. Additionally, it exhibits hydrophobic and insulating characteristics, which reduce the wettability of the electrode by electrolyte ions. As a result, the internal resistance of the device is elevated (Seman et al., 2022).

Polyvinylidene difluoride (PVDF) exhibits low hydrophilicity and possesses polarity attributed to its functional groups (CH_2-CF_2). It demonstrates remarkable chemical stability along with excellent resistance to both chemicals and corrosion. Additional examples of binders include carboxymethylcellulose (CMC), polyvinylidene chloride (PVDC), and graphene/PVDF composites, among others (Moniruzzaman et al., 2022).

2.4 SnO_2-Based Composite Materials for Supercapacitor Application

The SnO_2 nanoparticles are an important semiconductor having wide band gap energy around 3.6 eV. The SnO_2 is an n-type semiconductor in its purest ground state. The crystal structure of SnO_2 is tetragonal/rutile as presented in Fig. 2.4.

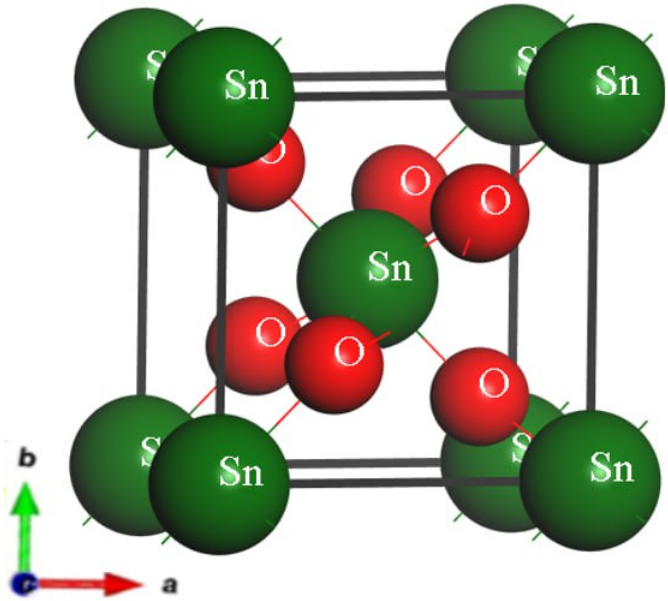

Figure 2.4: Crystal structure of SnO_2.

Tin dioxide has been widely studied due to its distinctive properties, such as excellent optical, electrical, thermal, and chemical properties. Numerous methods have been used to fabricate SnO_2 nanoparticles, e.g., spray pyrolysis (Atay & Akyuz, 2022), hydrothermal (Suthakaran et al., 2019), evaporation of tin grains in air (Le Minh, 2013), chemical vapor deposition (Y. Liu et al., 2005), thermal evaporation of SnO_2 powders (Binh et al., 2008), and the sol-gel method (Aziz et al., 2013).

SnO_2-based nanomaterials have attracted considerable attention as a promising electrode material for supercapacitors due to their low cost and high-power density. SnO_2-based supercapacitors have been paid significant attention due to their high electrochemical capacitor (EC) and chemical stability. There are different SnO_2-based composites for supercapacitor applications, like $ZnWO_4/SnO_2$ (Vinayaraj et al., 2020). SnO_2 holds potential uses in a range of applications, including sensors (B. Li et al., 2020) and solar cells (Dadkhah & Salavati-Niasari, 2014). SnO_2 is non-toxic, cost-effective, and straightforward to produce. Its outstanding physical and chemical characteristics are highly relevant for a range of applications, including gas sensors (Xi et al., 2008). photocatalysts (Ramanathan & Murali, 2022), lithium-ion batteries (Y. Wang & Lee, 2005), and supercapacitors (Lim et al., 2013). Rao et al. (2005) incorporated SnO_2 into a

supercapacitor, achieving a specific capacitance of merely 17.3 $F.g^{-1}$ when assessed at a current density of $0.1A.g^{-1}$. The SnO_2 nanoparticles were produced via a co-precipitation technique, and the supercapacitor's electrochemical performance was evaluated using CV and GCD testing. At a scan rate of 5 mVs^{-1}, the highest specific capacitance of 176 $F.g^{-1}$ was recorded (Manikandan et al., 2023). Supercapacitors based on SnO_2 have garnered considerable interest owing to their good electrochemical and chemical stability. This has led to the development of composites such as SnO_2/MnO_2 for use as electrodes in supercapacitors (H. Xiao et al., 2017).

Tin oxide/Graphene (SnO_2/G) nanocomposites were prepared by a simple wet chemical route. A maximum specific capacitance of 818.6 $F.g^{-1}$ was obtained for SnO_2/G-a composite at 1 mVs^{-1} scan rate, suggesting that the presence of graphene matrix in SnO_2 nanoparticles has enhanced the electrochemical behavior of SnO_2. The galvanostatic charge/discharge studies confirmed the good cyclic stability of the composite electrode (Velmurugan et al., 2016).

Joshi et al. (2022) reported the synthesis of SnO_2 nanoparticles using Camellia sinensis leaf extract. The biologically synthesized SnO_2 nanoparticles were subsequently combined with reduced graphene oxide (rGO) under ultrasonic conditions to form SnO_2/rGO composites. The freshly prepared SnO_2/rGO was employed as an electrode material for supercapacitors. The cost-effective SnO_2/rGO exhibited specific capacitances of 310.7 $F.g^{-1}$ at a scan rate of 10 mVs^{-1} and 267.8 $F.g^{-1}$ at a current density of 1 $A.g^{-1}$. Furthermore, the specific energy and specific power were determined to be 13.3 $Wh.kg^{-1}$ and 160.6 W kg^{-1} at 1 $A.g^{-1}$, and 4.6 $Wh.kg^{-1}$ and 1606.2 $W.kg^{-1}$ at 10 $A.g^{-1}$, respectively.

SnO_2/QDs/rGO composites were successfully constructed as electrode materials for supercapacitors. The results show that the prepared composite electrodes have a capacity of 253.3 $F.g^{-1}$ at a current density of $0.1A.g^{-1}$, and the capacity remains at 198.9 $F.g^{-1}$ even at 2 $A.g^{-1}$, indicating an excellent rate capability. Moreover, cyclic voltammetry results indicate that the composite electrodes present a specific capacitance retention of 95.9% after 6000 cycles, which supports potential application in supercapacitors (T.-T. Wei et al., 2021). G. Kumar et al. (2020) synthesized the ternary CeO_2/SnO_2/rGO nanocomposite, which delivered a specific capacitance of 156 $F.g^{-1}$ at $0.5A.g^{-1}$.

SnO_2, NiO, and SnO_2/NiO nanocomposites were synthesized at low temperature by a modified sol-gel method using ultrasonication. The analysis of the electrochemical performance of the material was done with the help of cyclic voltammetry and galvanostatic charge-discharge. The specific capacitance of the synthesized samples with different concentrations of SnO_2 and NiO was analyzed at different scan rates of 5 to 100 mVs^{-1}. Interestingly, a 7:1 mass ratio of NiO and SnO_2 nanocomposite exhibited a maximum specific capacitance of 464 $F.g^{-1}$ at a scan rate of 5 mVs^{-1} and good capacitance retention of 87.24% after 1000 cycles. These excellent

electrochemical properties suggest that the SnO_2/NiO nanocomposite can be used for a high energy density supercapacitor electrode material (Varshney et al., 2020).

Nano-scaled SnO_2/V_2O_5 mixed oxide is synthesized by a hydrothermal method in an autoclave. For comparative evaluation, V_2O_5 single oxide is prepared by a conventional process from ammonium vanadate. The capacitive behavior of the following electrodes is studied by cyclic voltammetry in 0.1 M KCl solutions: carbon nanotubes (CNT), V_2O_5, V_2O_3/CNT, and SnO_2/V_2O_5/CNT. At a scan rate of 100 mVs^{-1}, the SnO_2/V_2O_3/CNT electrode provides the best performance of 121.4 $F.g^{-1}$ (Jayalakshmi et al., 2007).

SnO_2 and various concentrations of g-C_3N_4 (25, 50, 75 and 100 mg) nanocomposite were investigated for electrochemical performance. At a current density of 1 $A.g^{-1}$, the green synthesized (SnO_2/g-C_3N_4 (50 mg)) SCN-50 nanocomposite displays a high specific capacitance of 302.7 $F.g^{-1}$, as well as the composite demonstrates excellent capacitance retention of 94 % after 10000 loops. Moreover, the asymmetric supercapacitor device of SnO_2/g-C_3N_4//Activated carbon performed good reversible and cyclic stability with high energy and power density (R. Kumar et al., 2024).

2.5 Bismuth-Based Composites for Supercapacitor Application

Bismuth compounds are attractive because of their low toxicity, low cost, and the ability to produce nanostructures with different shapes, morphologies, and sizes. These semiconductors, represented by $(Bi_2O_2)^2$ $(A_{n-1}B_nO_{3n+1})^{-2}$ $(A = Ba, Bi, Pb, etc.; B = Nb, W, Mo,$ etc.), possess unique layered structures in which perovskite slabs of $(A_{n-1}B_nO_{3n+1})^{-2}$ are sandwiched between $(Bi_2O_2)^2$ layers (H. Huang et al., 2019).

Bismuth-based materials have emerged as promising candidates for supercapacitor applications due to their unique electrochemical properties, high specific capacitance, and environmental benignity. These materials, particularly bismuth oxides like $BiMnO_3$ (Teli et al., 2022), and Bi_2S_3 (Danamah et al., 2023), BiOI (P. Wu et al., 2020), exhibit excellent redox activity and superior electrical conductivity, which enhance charge storage and energy density (Nie et al., 2015; T.-T. Wei et al., 2021). Their facile synthesis, stability in aqueous electrolytes, and potential for hybridization with carbon-based materials further contribute to their appeal in developing high-performance supercapacitors. The rGO/Bi_2O_3 composite demonstrated an enhanced specific capacitance of up to 94 $F.g^{-1}$ and exhibited good stability. This improvement is attributed to the pseudocapacitance of bismuth oxide, increased electrical conductivity, and the extensive charge separation area within the rGO matrix (Ciszewski et al., 2015). A better specific capacitance of 136.76 $F.g^{-1}$ has been observed in Bi_2O_3/graphene nanocomposite electrode material, compared to 81.03 $F.g^{-1}$ for pure Bi_2O_3-based electrode via a sol-gel synthesis method (Deepi et

al., 2018). The Bi_2O_3@MnO_2 composite electrode material outperforms both Bi_2O_3 and MnO_2 electrodes in a three-electrode system, exhibiting a specific capacitance as high as 350 $F.g^{-1}$ at 10 $A.g^{-1}$ (Shaikh et al., 2020).

Matinise et al. (2023) studied the bimetallic compound $BiFeO_3$ was successfully synthesized using a green method involving natural extract from *Moringa oleifera* and was evaluated as an electrode material for supercapacitors. The $BiFeO_3$ electrode achieved a specific capacitance of 105 $F.g^{-1}$ at a current density of 0.25 $A.g^{-1}$. The excellent specific capacitance value of 811 $F.g^{-1}$ at 50 mVs^{-1} with excellent charge discharge capacity is demonstrated by the perovskite bismuth ferrite embedded nitrogen-doped carbon ($BiFeO_3$-NC) nanocomposites, which are made using the polymeric precursor method and fired at 800^oC/6h for energy storage applications (Al-Maswari et al., 2021). Using the hydrothermal technique, pure MoS_2 and MoS_2/Bi_2S_3 nanocomposites with varying Bi concentrations were successfully produced. When compared to pure MoS_2, MoS_2/Bi_2S_3 nanocomposites had superior electrode/electrolyte interactions and outstanding electrochemical characteristics (K. B. M. Ismail et al., 2023).

Comparing the Bi_2MoO_6/PANI nanocomposite to pure Bi_2MoO_6, it offers several advantages for enhancing electrochemical performance, including a large reaction surface area, good structural stability, a high number of active sites, good strain accommodation, and quick electron and ion transportation. As a result, the Bi_2MoO_6/PANI electrode exhibits higher specific capacitance (826 $F.g^{-1}$ at 1 $A.g^{-1}$ current density) and capacitance retention (75.5% after 3000 cycles) at higher currents than pure Bi_2MoO_6 (90.0 $F.g^{-1}$) (F. Wu et al., 2017).

A novel composite consisting of polypyrrole (PPy) and bismuth oxide $\alpha - Bi_2O_3$ was examined for use as an electrode in supercapacitors. The $\alpha - Bi_2O_3$@PPy composite's specific capacitance was found to range from 634 to 301 $F.g^{-1}$, with respect to gravimetric currents of 3 and 10 $A.g^{-1}$ (Xavier et al., 2019). Moreover, bismuth-based polyaniline nanocomposites greatly improve the performance of supercapacitors by fusing the exceptional conductivity of polyaniline with the distinctive electrochemical characteristics of bismuth-based compounds. Nanomaterials like $BiVO_4$/PANI exhibit enhanced supercapacitance activity when a conducting polymer is added. The supercapacitor's efficiency is increased by this synergy, which also increases charge storage and rate capability. In addition to providing more stability and surface area, the nanocomposite structure also improves energy and power density (Srinivasan et al., 2020).

Flexible electrodes composed of a bismuth ferrite (BFO)/graphene nanocomposite were created using a straightforward drop-casting technique. The mechanical durability of the electrodes was evaluated by bending the supercapacitor. The BFO/graphene electrode provides enhanced accessibility to the electrolyte, while the graphene nanosheets serve as an efficient conductive route for charge transfer between the electrode material and the current collector. This electrode

demonstrated outstanding electrochemical performance in terms of specific capacitance and cycling stability. From a cyclic voltammetry test conducted at a scan rate of 10 mVs^{-1} within a potential range of 0-0.9 V, the electrode exhibited a specific capacitance of 9 $mF.cm^{-2}$. It is capable of delivering a specific power ranging from 0.5 to 3.5 $kW.kg^{-1}$ along with a reasonable energy density (Soam et al., 2020). As a result, bismuth-based materials hold significant potential for advancing energy storage technologies, offering a sustainable and efficient solution for modern energy demands (Y. Li et al., 2019).

The layered structure of $Bi_5Nb_3O_{15}$ (see Fig. 2.5) facilitates rapid ion diffusion and electron transport, enhancing its charge-discharge capabilities. Additionally, its ability to maintain performance over numerous cycles makes it a viable candidate for sustainable energy storage solutions. Research into $Bi_5Nb_3O_{15}$ continues to reveal its potential for integration into high-performance supercapacitors, promising advancements in energy storage technology (Y. Li et al., 2019).

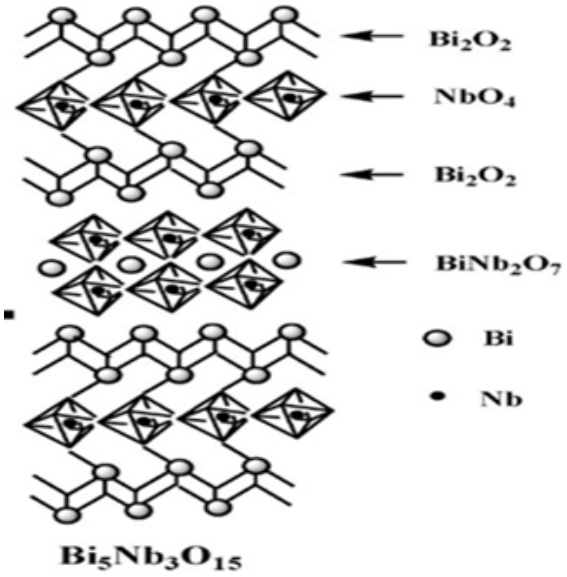

Figure 2.5: A mixed layered orthorhombic crystal structure of $Bi_5Nb_3O_{15}$ (Guo et al., 2011).

2.6 Electrode System

2.6.1 Three-Electrode Setup

The three-electrode arrangement is a commonly utilized configuration, as illustrated in Fig. 2.6. This setup consists of a working electrode (WE), a counter electrode (CE), and a reference electrode (RE). Current circulates between the working and counter electrodes, while the potential is recorded between the working and reference electrodes. There is no current flow between

the working and reference electrodes, leading to an insignificant potential drop. Consequently, any voltage drop caused by the solution is compensated. The role of the counter electrode is to balance the total current measured at the working electrode, and it experiences a significant potential (S. Sharma & Chand, 2023).

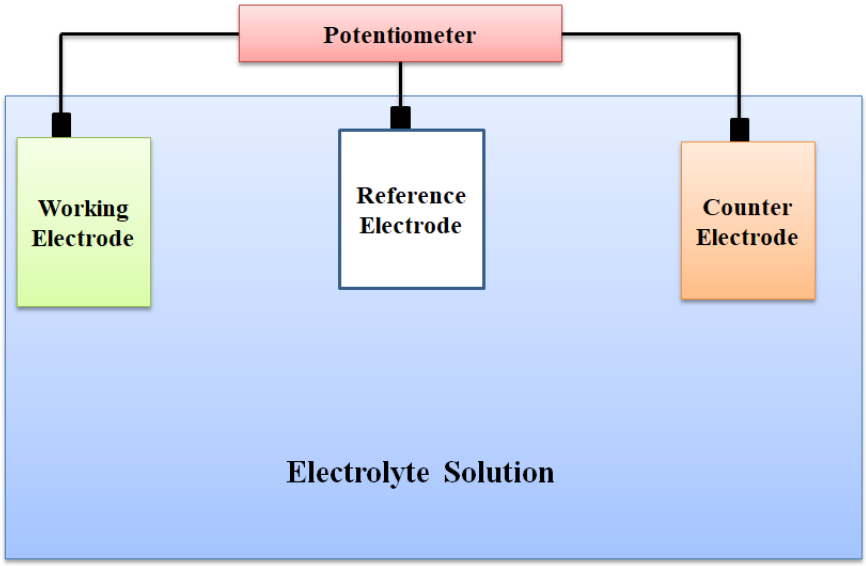

Figure 2.6: Illustration diagram for three electrodes set up (Meng et al., 2017).

2.6.2 Two-Electrode Setup

Supercapacitor electrodes can be evaluated for their electrochemical performance using either a three-electrode or a two-electrode (device) configuration. In most cases, the specific capacitance of an electrode material is first measured using a three-electrode system to identify its optimal working conditions. Once satisfactory results are achieved, the study proceeds to a two-electrode setup, which more accurately reflects real device performance (Nath et al., 2022). Unlike the three-electrode system that may overestimate the material's capacitance due to its high sensitivity, the two-electrode configuration provides a more practical assessment of the electrode's behavior. In this setup, the device can be symmetric (both electrodes made of the same material) or asymmetric (different materials for each electrode), with the two electrodes separated by an electrolyte-soaked separator. The assembly typically includes a metallic spacer and spring to ensure firm contact between components. Key parameters such as specific energy, power density, and cycle stability of the supercapacitor can be effectively evaluated using the two-electrode configuration (Ahmed et al., 2023).

In a setup utilizing a two-electrode cell (see Fig. 2.7) or as shown in Fig. 2.2 (a), the counter electrode (CE) and reference electrode (RE) are connected to one electrode, while the working electrode (WE) and the sensor (S) are linked to the opposing electrode (Imran et al., 2023).

The total potential across the entire cell is recorded, which encompasses contributions from the CE/electrolyte interface as well as the electrolyte itself. Consequently, this two-electrode arrangement can be employed when precise management of the interfacial potential at the WE-electrolyte interface is not essential, and the overall performance of the cell is being assessed (Dunn et al., 2011).

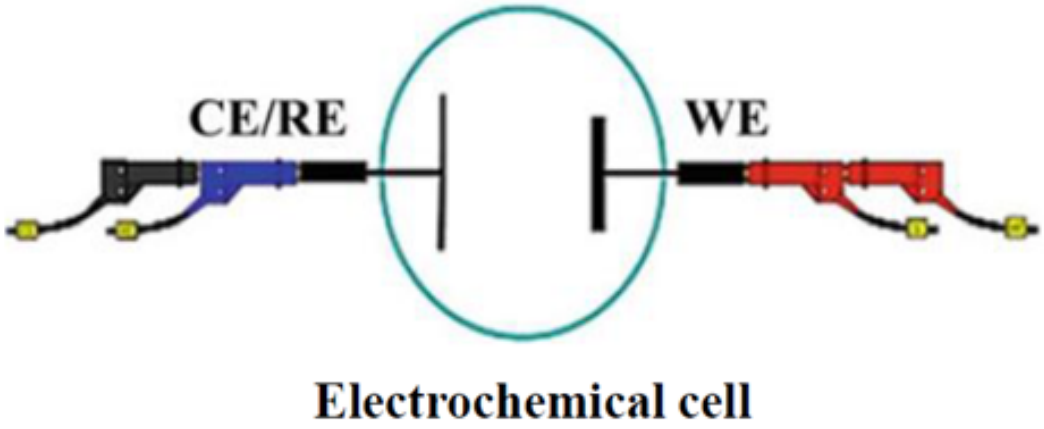

Figure 2.7: Schematic view of the two-electrode setup.

2.7 Fundamentals of Electrochemical Characterization

The performance of a supercapacitor is defined by several key parameters, including cell capacitance, operating voltage, equivalent series resistance (ESR), power density, energy density, and time constant. In most evaluations, three core parameters, cell (or total) capacitance, operating voltage, and ESR are primarily used to assess energy and power performance. These parameters are typically sufficient for commercial devices where materials, fabrication methods, and cell designs are standardized. However, in research focused on developing new materials, advanced manufacturing techniques, and innovative cell designs, additional performance metrics become essential (Mehra et al., 2024).

A comprehensive understanding of supercapacitor performance requires consideration of a wide range of factors and their complex interrelationships (Xing et al., 2022). Figure 2.8, provides an overview of key performance metrics, major influencing factors, and corresponding test methods for supercapacitor evaluation. The three core parameters are cell capacitance, operating voltage, and equivalent series resistance, are highlighted in yellow. Power and energy densities are represented in dark blue, while the time constant and cycling stability appear in light orange. Major affecting factors are shown in light purple, and test methods are indicated in white. Figure 2.8, illustrates the complex relationships between these elements, providing a comprehensive

framework for performance assessment of supercapacitors (Karthikeyan et al., 2021).

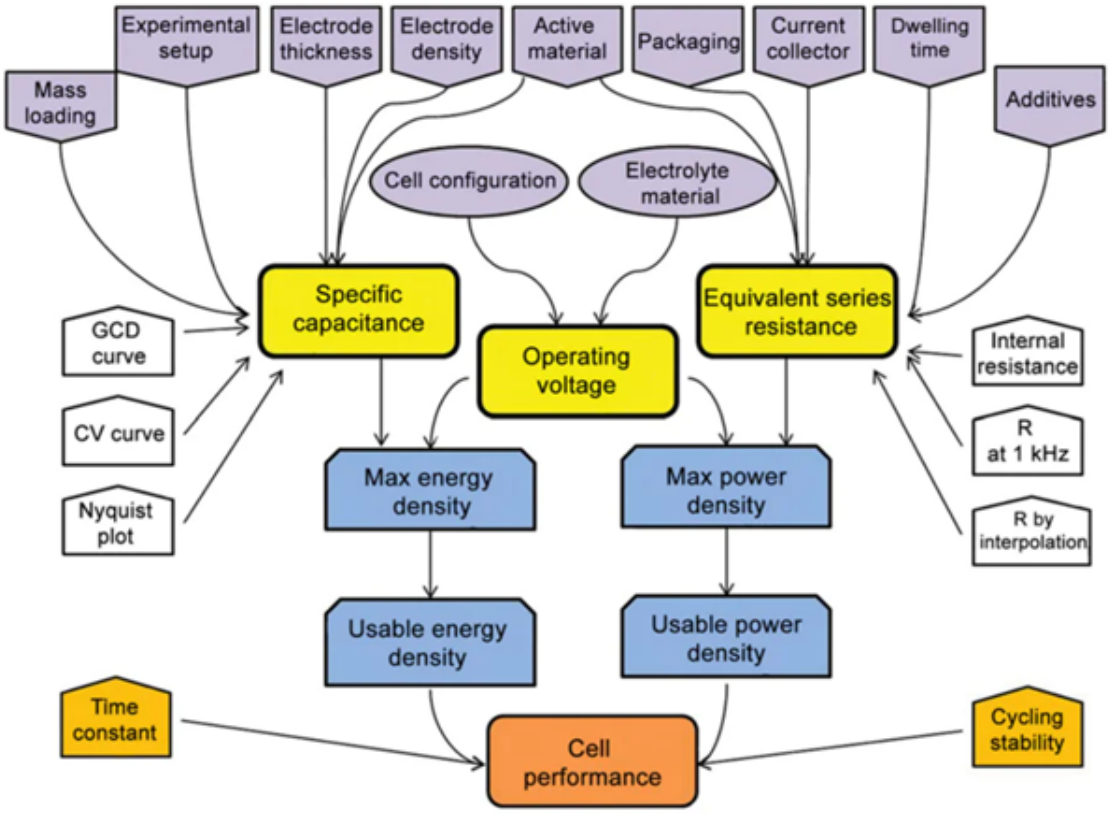

Figure 2.8: Schematic representation of performance parameters, critical influencing factors, and associated test methods for supercapacitors (Karthikeyan et al., 2021).

Generally, three techniques are used to evaluate the electrochemical performance of SCs including cyclic voltammetry (CV), galvanostatic charge/discharge (GCD), and electrochemical impedance spectroscopy (EIS) (ABID et al., 2020).

2.7.1 Cyclic Voltammetry (CV)

CV is an effective and widely used electrochemical method for evaluating a system's entire behavior, including its kinetic and thermodynamic aspects. It is a practical way to record the current versus potential and measure the current responsiveness of a redox-active solution (Palagonia et al., 2019). A linearly altered electric potential is applied during CV testing between the references and working electrodes in three-electrode designs or between the positive and negative electrodes in two-electrode systems. The sweep rate, also known as the scan rate, is the speed of the potential change in $mV.s^{-1}$, whereas the potential windows are the range of possible changes. The electrochemical reactions involved are characterized by recording the instantaneous current during the cathodic and anodic sweeps. The data are plotted as potential (V) against current (A)(Allagui et al., 2016; Tomboc & Kim, 2019). When EDLC and PC

types have different characteristics, CV testing using a three-electrode setup is thought to be the most appropriate method for examining the charge storage mechanisms of SC materials. The test results can first be interpreted using the shape of the CV curves. For EDLC and most PC materials, the resulting CV curves have an appealing rectangular shape, but for other PC materials, there may be noticeable redox peaks that occur in a very reversible way (Kuo et al., 2006). Therefore, using the shape of CV curves alone to distinguish between EDLC and PC materials is insufficient. Therefore, it is not sufficient to differentiate EDLC and PC materials solely by observing the shape of CV curves. The operating voltage or potential window for supercapacitor materials is determined by CV testing. In a three-electrode setup, the reversibility of the charge and discharge processes is investigated while the reversal potential is changed. It is also possible to assess total cell capacitance, specific capacitance, and energy performance (Elgrishi et al., 2018).

Specific capacitances (C_{SP}) of the materials were calculated by integrating the area under CV curves using Eq. (2.2) (Ismail et al., 2020):

$$C_{\mathrm{sp}} = \frac{1}{m\nu\Delta V}\int_{V_1}^{V_2} I(v)\,dV, \tag{2.2}$$

where ν is the scan rate (Vs^{-1}), m is the active mass of the material (g), and ΔV is the potential window. The term $\int_{V_1}^{V_2} I(v)\,dV$ represents the integral area under the CV curve.

The charge storage mechanism of the nanoparticles and nanocomposites was further evaluated through a detailed analysis of their CV curves. A power-law relationship between the peak current and the scan rate (ν) was employed to identify the dominant charge-storage process using Eqs. (2.3) and (2.4):

$$I = a\nu^{b}, \tag{2.3}$$

$$\log(I) = b\log(\nu) + \log(a), \tag{2.4}$$

where I represents the peak current, ν is the scan rate, and a and b are adjustable parameters.

The parameter b, which indicates the charge storage mechanism, can be obtained from the slope of the plot of log(peak current) versus log(scan rate). As the value of b approaches 1, the charge storage mechanism is considered a surface-controlled process involving physical adsorption and desorption. In contrast, when the b value approaches 0.5, the storage process is diffusion-limited. To determine the b value, the logarithm of the scan rate ($\log\nu$) was plotted against the logarithm of the current ($\log I$) at a fixed potential (Alshoaibi, 2025; Karadurmus et al., 2022; Qin et al.,

2022).

Dunn's method is used to distinguish surface-controlled (capacitive) and diffusion-controlled charge storage contributions from CV curves. It is based on the relationship between current (i) and scan rate (ν), expressed as

$$i(v) = K_1 \nu + K_2 \nu^{1/2}. \tag{2.5}$$

where $k_1\nu$ represents the capacitive contribution and $k_2\nu^{1/2}$ represents the diffusion-controlled contribution. By rearranging this expression,

$$\frac{i(V)}{\nu^{1/2}} = k_1 \nu^{1/2} + k_2, \tag{2.6}$$

where i, ν, K_1, and K_2 indicate the current, scan rate, and constants, respectively, and $K_1\nu$ and $K_2\nu^{1/2}$ represent the current contributions from the surface capacitive effects and the diffusion-controlled intercalation process, respectively.

2.7.2 Galvanostatic Charging-Discharging (GCD)

GCD testing is one of the most common and reliable procedures for measuring supercapacitors (SCs) under direct current circumstances. This technique involves repeatedly charging and discharging the device or its working electrode at a constant current level, with or without a dwelling period in which the peak voltage is held constant before discharge begins. The standard result is a plot of potential (v) vs time (s), which can be used to extract significant performance data (Abdel Maksoud et al., 2021). Choosing an adequate constant current level is crucial because it ensures the development of consistent, reliable, and comparable data across various tests and equipment. Cell capacitance (C_T), equivalent series resistance (ESR), and operating voltage (V_o) are the three primary performance metrics that may be determined using GCD testing, which is thought to be a very flexible and accurate method for assessing SC devices. Other important characteristics like the time constant, power density, energy density, and peak current can be obtained from these fundamental values. Additionally, examining the cycling stability of SCs over extensive charge/discharge cycles is especially suited for GCD testing. GCD testing also offers comprehensive details on the electrode materials' specific capacitance, charge/discharge reversibility, and potential window when carried out with a three-electrode setup (ABID et al., 2020). The specific capacitance (C_{SP}) has been evaluated from the charge-discharge curves, according to Eq. (2.7) (Reddy & Ramaprabhu, 2007).

$$C_{\text{sp}} = \frac{I\,\Delta t}{m\,\Delta V}, \tag{2.7}$$

where I is the applied current, m is the mass of each electrode, Δt is the discharging time, and ΔV is the potential window.

Coulombic Efficiency

Coulombic efficiency (η) represents the ratio of the discharge time to the charge time of a supercapacitor, reflecting the effectiveness of charge transfer during electrochemical reactions (Laheäär et al., 2015). It is calculated as:

$$\eta(\%) = \frac{t_D}{t_c} \times 100\%, \tag{2.8}$$

where t_D is the discharge time and t_c is the charging time during galvanostatic charging and discharging.

Capacitance Retention

Capacitance retention serves as a vital indicator for assessing the long-term stability and longevity of a supercapacitor (An et al., 2019). It is represented as the percentage of the original specific capacitance (C_o) that persists following a defined number of continuous charge-discharge cycles and is determined using the formula:

$$Retention(\%) = \frac{C_N}{C_o} \times 100. \tag{2.9}$$

In this formula, C_N denotes the specific capacitance after N cycles, while C_o represents the initial specific capacitance. Elevated retention percentages suggest that the electrode material sustains its electrochemical performance with minimal deterioration over prolonged cycling. This stability is influenced by various factors, including electrode composition, structural integrity, electrolyte compatibility, and the applied potential window. A retention profile nearing 100% after thousands of cycles indicates not only excellent reversibility of electrochemical processes but also robust mechanical stability of the electrode.

To ensure efficient charge transfer and maximize electrochemical performance in two electrode system, mass balance between the positive (WE) and negative electrodes was achieved using the mass-charge balance equation (Eq. 2.10) (G. Z. Chen, 2017; Koventhan & Lo, 2024),

$$\frac{M^+}{M^-} = \left(\frac{C^-_{\mathrm{sp}}}{C^+_{\mathrm{sp}}}\right)\left(\frac{\Delta V^-}{\Delta V^+}\right), \tag{2.10}$$

where M is the active mass of the electrode, C_{SP} is the specific capacitance obtained from the three-electrode system, and ΔV is the potential window.

In general, asymmetric supercapacitors involve two different capacitive electrodes. Typically, the negative electrode (or the first electrode) is based on carbon-based materials with a very large surface area, while the other electrode is the pseudocapacitive electrode, which is based on conducting polymers or metal oxides. The introduction of a pseudocapacitive electrode introduces Faradaic (redox) processes, adding pseudocapacitance to the overall performance. Complementary potential ranges for the two electrodes are combined in these designs in order to widen the cell voltage and hence improve energy density compared to symmetric configurations. Asymmetric supercapacitors consist of two capacitive electrodes. The pseudocapacitive electrode is made of conducting polymers or metal oxides, while the capacitive electrode typically uses carbon materials that have a large specific surface area. This design includes Faradaic capacitance because of the pseudocapacitive electrode. Asymmetric designs aim to improve energy density compared to symmetric ones by creating a wider cell voltage. This is achieved through the combination of complementary potential windows from the positive and negative electrodes. The specific capacitance (C_{SP}) was calculated from the discharge curves using the following Eq. 2.11 (Ndipingwi et al., 2018):

$$C_{\mathrm{sp}} = \frac{4I\Delta t}{m\Delta V}, \tag{2.11}$$

where I = the current (mA), m = the mass of both positive and negative electrodes (mg), Δt = discharge time (s), and ΔV = voltage window (V).

Specific energy and specific power are essential performance metrics that describe the energy-storage efficiency and power-delivery capability of supercapacitors. The specific energy (E_{sp}) indicates how much energy a device can store per unit mass and is calculated using

$$E_{\mathrm{sp}} = \frac{1}{2}C_{\mathrm{sp}}(\Delta V)^2, \tag{2.12}$$

where C_{sp} is the specific capacitance and ΔV is the operating potential window. In contrast, the specific power (P_{sp}) represents how quickly the stored energy can be delivered and is given by

$$P_{\mathrm{sp}} = \frac{E_{\mathrm{sp}}}{\Delta t}, \tag{2.13}$$

where Δt is the discharge time. Supercapacitors generally offer lower specific energy but exceptionally high specific power, making them ideal for applications requiring rapid energy delivery, such as regenerative braking, load leveling, and pulse-power systems.

2.7.3 Electrochemical Impedance Spectroscopy (EIS)

EIS testing, sometimes referred to as dielectric spectroscopic testing, applies a low amplitude alternating voltage (typically 5-10 mV) over top of a steady state potential to assess a power cell's impedance as a function of frequency (Karmakar, 2024). The resulting data are typically displayed graphically as a Nyquist plot, which shows the imaginary and real components of the cell impedances on a complex plane, and a Bode plot, which shows the cell response between the phase angle and frequency (Sunil et al., 2021). EIS has been used to estimate the capacitance, energy, and power attributes, as well as to characterize the charge transfer, mass transport, and charge storage mechanisms, in addition to the frequency response and impedance. The impedance of an electrochemical system can be determined by applying a low-amplitude alternating voltage ΔV superimposed on a steady-state potential (V_s) as expressed in Eq. Eq. 2.14:

$$\Delta V(\omega) = \Delta V_{\max} e^{j\omega t}. \tag{2.14}$$

Here, $\Delta V_{\max}$ represents the signal amplitude, and ω is the angular frequency. The applied voltage gives rise to alternating output current ΔI, described by Eq. 2.15:

$$\Delta I(\omega) = \Delta I_{\max} e^{j(\omega t+\phi)}. \tag{2.15}$$

In this expression, ϕ is the phase angle of the current relative to the voltage and ΔI is the current amplitude.

The electrochemical impedance, $Z(\omega)$ is then defined as:

$$Z(\omega) = \frac{\Delta V(\omega)}{\Delta I(\omega)} = |Z(\omega)|e^{-i\phi} = Z' + Z'', \tag{2.16}$$

where $Z^{'}$ and $Z^{''}$ are the real and imaginary components of the impedance, respectively. The magnitude of the impedance is given by:

$$|Z(\omega)|^2 = Z'^2 + Z''^2, \tag{2.17}$$

The Nyquist plot, which represents $Z^{'}$ versus $Z^{''}$ on a complex plane, it is commonly used to evaluate impedance data. Electrochemical impedance spectroscopy (EIS) provides valuable information on parameters such as impedance magnitude, specific capacitance, charge transfer resistance, mass transport behavior, and charge storage mechanisms. The impedance, specific

capacitance, charge transfer, mass transport, and charge storage mechanisms involved in SC materials can be investigated using EIS testing by performing a comparable analysis in a three-electrode system (Magar et al., 2021). Electrochemical impedance spectroscopy (EIS) is a powerful test that provides information regarding series resistance Rs, charge transfer resistance Rct, double layer capacitance Cdl, and Warburg impedance Zw created by diffusion (Sakita et al., 2021).

2.8 Characterization Techniques

Characterization techniques are essential for understanding the structural, chemical, and electrochemical properties of electrode materials used in supercapacitors. X-ray diffraction (XRD) is employed to determine the crystalline structure, phase purity, and average crystallite size of synthesized materials, confirming the successful formation of composite structures such as metal oxides, polymers, or carbon-based hybrids (Z. Wang et al., 2020). The crystallite sizes were calculated using the Debye-Scherrer equation (Fatimah et al., 2022), with the equation represented in Eq. 2.18.

$$D = \frac{K\lambda}{\beta \cos\theta}. \tag{2.18}$$

In this equation, D represents the crystallite size in nm, k is a shape factor of the crystallite (usually taken as 0.9), λ stands for the incident wavelength of X-rays (0.154 nm), β denotes the full width at half maximum (FWHM) of the selected peak in radians, and θ signifies the diffraction angle (Bragg's angle) at which the peak arises, also measured in radian. Bragg's law states that waves are constructively added in certain directions, and expressed using Eq. 2.19: (Jacob et al., 2015)

$$2d_{hkl} \sin\theta = n\lambda, \tag{2.19}$$

where d_{hkl} is the interplanar spacing between diffracting angles, θ is the diffraction beam angle, n is the order of diffraction, and λ is the wavelength of the beam.

From the tetragonal structure of nanoparticles ($a = b \neq c$; $\alpha = \beta = \gamma = 90^\circ$), the lattice constants can be calculated by Eq. 2.20:

$$\frac{1}{d_{hkl}^2} = \frac{h^2 + k^2}{a^2} + \frac{l^2}{c^2}, \tag{2.20}$$

where, d_{hkl} is the interplanar spacing, h, k, and l are integers, (hkl) is the lattice plan index, and a and c are lattice constants.

From the orthorhombic crystal structure ($a \neq b \neq c; \alpha = \beta = \gamma = 90^{\circ}$) the lattice parameters can be calculated by Eq. 2.21:

$$\frac{1}{d_{hkl}^2} = \frac{h^2}{a^2} + \frac{k^2}{b^2} + \frac{l^2}{c^2}, \tag{2.21}$$

where d_{hkl} is the interplanar spacing, (h, k, l) are the Miller indices and (a, b, c) are the lattice constants.

Fourier Transform Infrared Spectroscopy (FTIR) provides information on the functional groups and chemical bonding within the material. By identifying characteristic vibrational peaks, FTIR confirms the interaction or successful incorporation of components in composite materials (Mohamed et al., 2017).

UV-vis spectroscopy is a valuable technique for the study of the absorption properties of nanomaterials. UV-vis radiations, which are a component of the electromagnetic spectrum, can be used in spectroscopy to get valuable insights into the properties of materials. This includes understanding their absorption, transmission, and reflectivity characteristics. The performance of a material in multiple technological uses, such as conductivity, transparency, and light absorption efficiency, can be estimated by precisely calculating the optical band gap using Eq. 2.22 (Picollo et al., 2019).

$$(\alpha h\nu) = A(h\nu - E_g)^n, \tag{2.22}$$

where n is the nature of electrons transition, n = ½ and 2 are direct and indirect transition band gaps, respectively, α is the absorption coefficient, hν is the photon energy, A = 1 is a constant that depends on the material and the measurement conditions, and E_g is the optical bandgap energy of the material.

The energy band gap (E_g) of a nanomaterials can be determine by plotting $(\alpha h\nu)^{1/n}$ versus $h\nu$ and extrapolating the linear portion of the plot to $(\alpha h\nu)^{1/n} = 0$, where n is the nature of electrons transition, n = ½ and 2 are direct and indirect transition band gaps, respectively (Sangiorgi et al., 2017).

The Scanning Electron Microscope (SEM) provides detailed images of the surface morphology, allowing observation of particle size, shape, and porosity, which are crucial factors influencing ion diffusion and charge storage capacity. Energy-Dispersive X-ray Spectroscopy (EDX) coupled with SEM offers elemental analysis, confirming the presence and uniform distribution of constituent elements in the composite (Jacob et al., 2015). Meanwhile, the Transmission Electron Microscope (TEM) provides high-resolution insights into the internal structure, lattice fringes, and interfacial bonding of nanomaterials, enabling a better understanding of their nanoscale architecture (Mohammed & Abdullah, 2018).

CHAPTER 3

MATERIALS AND METHODS

3.1 Materials

Analytical grade chemicals and reagents were used without further purification: tin(II) chloride dihydrate ($SnCl_2 \cdot 2H_2O$, 99%, Sigma-Aldrich), bismuth nitrate pentahydrate ($Bi(NO_3)_3 \cdot 5H_2O$), niobium chloride ($NbCl_5$), aniline ($C_6H_5NH_2$, $\geq$ 99.5%, Sigma-Aldrich), ammonium persulfate ($(NH_4)_2S_2O_8$, 98%, Sigma-Aldrich, APS), hydrochloric acid (HCl, $\geq$ 37%, Sigma-Aldrich), sulfuric acid (H_2SO_4, $\geq$ 98%, Sigma-Aldrich), polyvinylidene difluoride (PVDF), N-methyl-2-pyrrolidone (NMP), carbon black, activated carbon, absolute ethanol (C_2H_5OH, $\geq$ 99.8%), and deionized water. The chemical reagents were selected based on their suitability for the synthesis of metal oxide nanoparticles, conducting polymer formation, and electrode fabrication for electrochemical energy storage applications. $SnCl_2 \cdot 2H_2O$ and $Bi(NO_3)_3 \cdot 5H_2O$ were chosen as precursor sources for SnO_2 and $Bi_5Nb_3O_{15}$ due to their high purity, good solubility, and thermal stability, which facilitate controlled nanoparticle formation. $NbCl_5$ was used as the Nb source to form the $Bi_5Nb_3O_{15}$ phase. Aniline was selected as the monomer for polyaniline (PANI) synthesis because of its well-established polymerization behavior and excellent electrical conductivity in acidic media. $(NH_4)_2S_2O_8$ served as an oxidizing agent to initiate and control the polymerization of aniline. HCl and H_2SO_4 were employed to maintain an acidic environment favorable for PANI formation and electrochemical measurements. PVDF and N-methyl-2-pyrrolidone were used as binder and solvent, respectively, to prepare stable electrode coatings, while carbon black and activated carbon were incorporated to enhance electrical conductivity and surface area. Absolute ethanol and deionized water were used as solvents to ensure purity and prevent contamination during synthesis and processing.

3.2 Methods

3.2.1 Preparation of Plant Extract

Leaves of *vernonia amygdalina* (grawa) plant extract were carefully harvested from the University of Nigeria, Nsukka, Nigeria. After collecting the leaves, they were initially washed with water and then rinsed with distilled water to eliminate any dust particles. Subsequently, the leaves were air-dried at room temperature for a few weeks. Finally, the dried *vernonia amygdalina* leaves were chopped into pieces and preserved in sealed plastic bags for future use. 10 g

of dried *vernonia amygdalina* leaves were heated with 100 mL of distilled water at 60^{o}C for 30 minutes. Afterward, the extract was allowed to cool at room temperature, filtered with Whatman filter paper No. 1, and stored at 4^{o}C for subsequent experiments.

3.2.2 Synthesis of SnO_2 Nanoparticles Using *Vernonia Amygdalina* Plant Leaf Extract

The synthesis of SnO_2 nanoparticles was carried out using *vernonia amygdalina* leaf extract via a green synthesis approach. A 100 mL solution of 0.2 M $SnCl_2{\cdot}2H_2O$ was prepared in distilled water and heated at 60 °C for 15 minutes before incorporating the plant extract. In a standard procedure, 20 mL of *vernonia amygdalina* extract was slowly added to the 100 mL precursor solution while stirring continuously. After stirring for 30 minutes, the solution transitioned from white to an orangish color, signaling the development of SnO_2 nanoparticles. The mixture was subsequently heated to 60^{o}C for 2 hrs while being stirred using a magnetic stirrer, then cooled to room temperature and kept for further stabilization for 12 hrs. The resulting precipitate was centrifuged and thoroughly washed several times with distilled water, followed by three washes with ethanol. The paste was then dried in an oven at 70°C for 12 hrs. Ultimately, the dried powder was placed in a crucible and annealed at 600^{o}C for 4 hrs to produce SnO_2 nanoparticles (see Fig. 3.1).

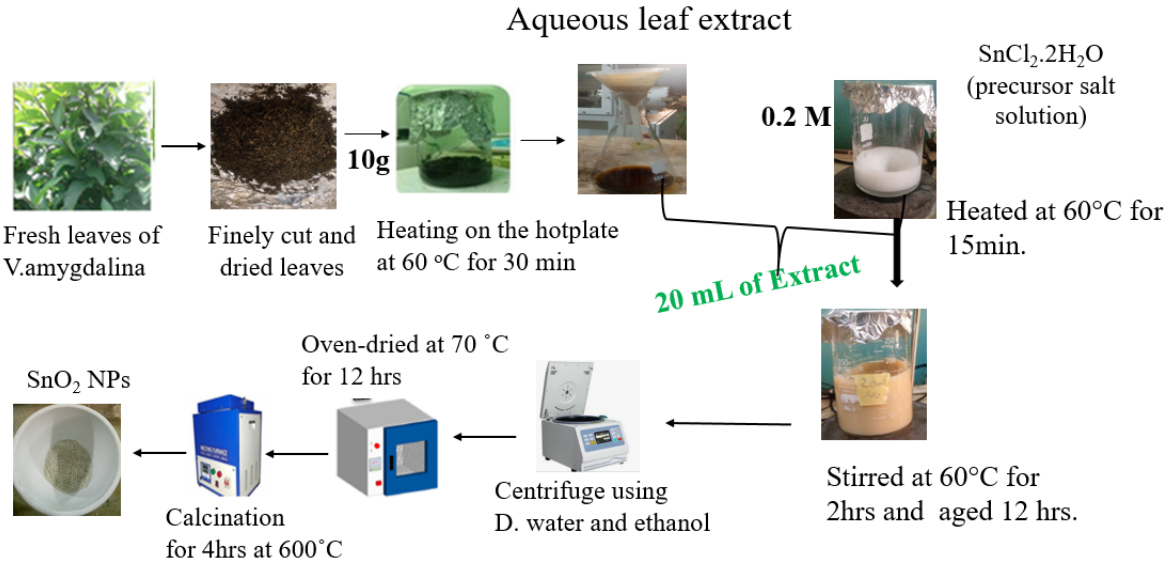

Figure 3.1: Preparation of SnO_2 nanoparticles using *Vernonia amygdalina* plant leaf extract.

The overall reaction mechanism of the synthesis of SnO_2 nanoparticles using *vernonia amygdalina* leaf extract are as shown in Eq. 3.1, and R represents a hydrocarbon group (alkyl or aryl group) attached to a hydroxyl group (-OH) from the phytochemicals present in plant extract.

$$SnCl_2 \cdot 2H_2O + R\text{–}OH + O_2 \xrightarrow{\text{heat}} SnO_2 + 2HCl + H_2O + \text{Oxidized Phytochemicals} \quad (3.1)$$

3.2.3 Synthesis of $Bi_5Nb_3O_{15}$ Nanoparticles Using *Vernonia amygdalina* Plant Leaf Extract

The $Bi_5Nb_3O_{15}$ nanoparticle was synthesized using *vernonia amygdalina* leaf extract through a green synthesis method. First, 8 mmol of $Bi(NO_3)_3.5H_2O$ was dissolved in 100 mL of distilled water, and separately, 4.8 mmol of $NbCl_5$ was dissolved in 100 mL of distilled water. Subsequently, the $NbCl_5$ solution was added slowly to the $Bi(NO_3)_3$ solutions. Then, 20 mL of V. amygdalina leaf extract was introduced during mixing, and the solution was stirred magnetically for 1hr at room temperature, and then placed in an oven at 80 ^oC for 1 hr and then followed by three washings with distilled water and ethanol, after centrifugation, and it was oven-dried at 70 ^oC for 12 hrs. Ultimately, the dried powder was annealed for 3hrs at 500 ^oC (Fig. 3.2) (Guo et al., 2011; Lee et al., 2013).

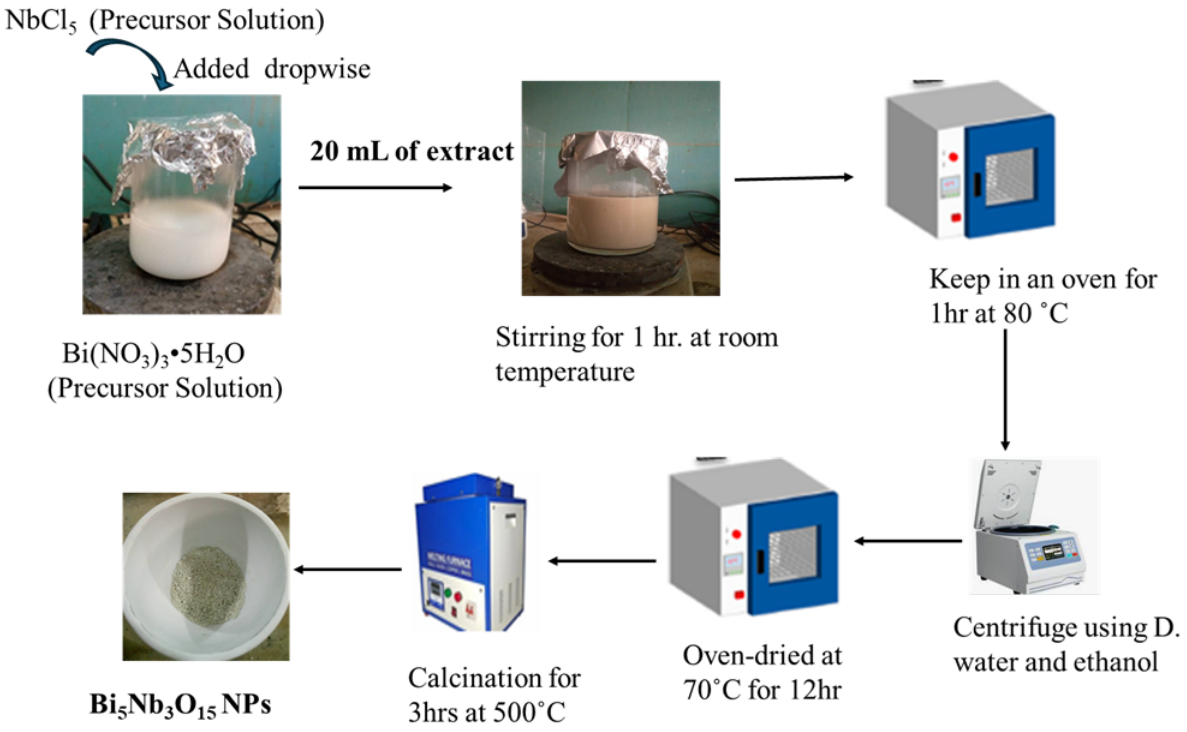

Figure 3.2: Preparation of $Bi_5Nb_3O_{15}$ nanoparticles using *Vernonia amygdalina* plant leaf extract.

$Bi_5Nb_3O_{15}$ nanoparticles were synthesized via a green approach using $Bi(NO_3)_3 \cdot 5H_2O$ and $NbCl_5$ as precursors, where phytochemicals (R–OH) from *V. amygdalina* leaf extract acted as reducing and stabilizing agents, and atmospheric oxygen facilitated the oxidation of Bi^{3+} and Nb^{5+} during heating, as shown in Eq. 3.2.

$$Bi(NO_3)_3 \cdot 5H_2O + NbCl_5 + R\text{–}OH + O_2 \xrightarrow{heat} Bi_5Nb_3O_{15} + NO_x + HCl + H_2O + R{=}O \quad (3.2)$$

3.2.4 Synthesis of Polyaniline (PANI) Polymer

Polyaniline was produced using a chemical polymerization technique. The method involved dissolving 4 mmol of aniline and 4 mmol of $(NH_4)_2S_2O_8$ (APS) separately in 50 mL of 1 M HCl, and also both solutions were stirred for 1 hr. To initiate the polymerization reaction, the APS solution (see Fig. 3.3(B) was added dropwise to the aniline solution (see Fig. 3.3(A) and stirred for about 3 hrs at 0-5^{o}C. Subsequently, the obtained precipitates were washed multiple times double-distilled water until the washings became clear. The precipitates were further washed with acetone and dried at 60^{o}C 12hrs (Abdolahi et al., 2012). This process is illustrated in Fig. 3.3.

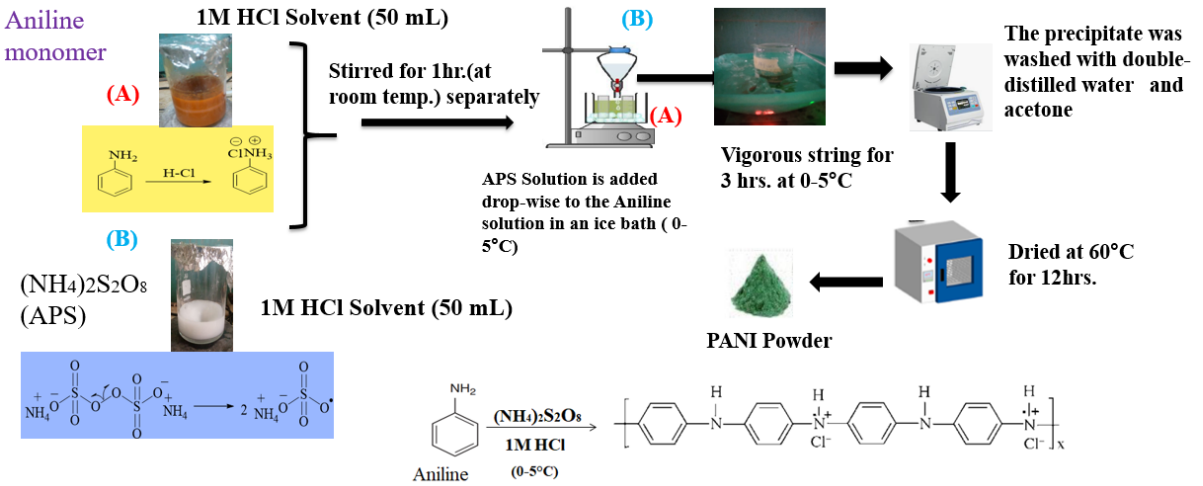

Figure 3.3: Synthesis process of polyaniline (PANI) polymer.

3.2.5 Synthesis of $SnO_2/Bi_5Nb_3O_{15}$ Nanocomposites

An ultrasonication assisted method is employed to synthesize the $SnO_2/Bi_5Nb_3O_{15}$ nanocomposite. Initially, 0.5 g of SnO_2 is dispersed in 50 mL of distilled water and stirred for 10 minutes to achieve uniform dispersion. Subsequently, 0.5 g of $Bi_5Nb_3O_{15}$ is added to the mixture, followed by ultrasonic treatment for 2 hrs to enhance mixing and interaction between the components. The resulting colloidal suspension is then filtered and repeatedly washed by distilled water and followed by ethanol to eliminate impurities. Finally, the suspension is dried in an oven at 80^{o}C for 12 hrs to obtain the nanocomposite.

3.2.6 Synthesis of SnO_2/PANI Nanocomposites

The SnO_2/PANI composites were synthesized using an ultrasonication-assisted method. Various amounts of SnO_2 (0.45g, 0.40g, 0.35g) and PANI (0.05g, 0.1g, 0.15g) were used in the composite formation. Initially, 0.45g of SnO_2 and 0.05g of PANI were taken from the synthesized

sample. Each component was separately dispersed in 50 mL of deionized water and processed through sonication for 1hr to achieve complete dispersion. Afterward, the mixtures of SnO_2 and PANI were combined under stirring and continuously heated to promote solvent evaporation. Once the solvent had fully evaporated, the composite was dried for 12 hrs in an oven at 70^oC. The dried samples were then ground using an agate mortar, resulting in the SnO_2/PANI sample, which was labeled SnO_2/PANI-10%. The other SnO_2/PANI nanocomposites were synthesized as the same procedure with SnO_2/PANI-10%. The samples mixed with varying mass ratios of PANI were designated as SnO_2/PANI-X, where X representing the proportion of PANI in the sample SnO_2/PANI-10, SnO_2/PANI-20 and SnO_2/PANI-30. The PANI content in SnO_2/PANI-10, SnO_2/PANI-20, and SnO_2/PANI-30 were calculated to be 10wt%, 20wt%, and 30wt%, respectively.

3.2.7 Synthesis of $Bi_5Nb_3O_{15}$/ PANI (BNO/PANI) Nanocomposites

The BNO/PANI composites were prepared via an ultrasonication process as illustrated in Fig. 3.4. The BNO/PANI nanocomposites were constituted using varying BNO-to-PANI mass ratios of 9:1, 8:2, and 7:3, corresponding to total masses of 0.5 g for each combination.

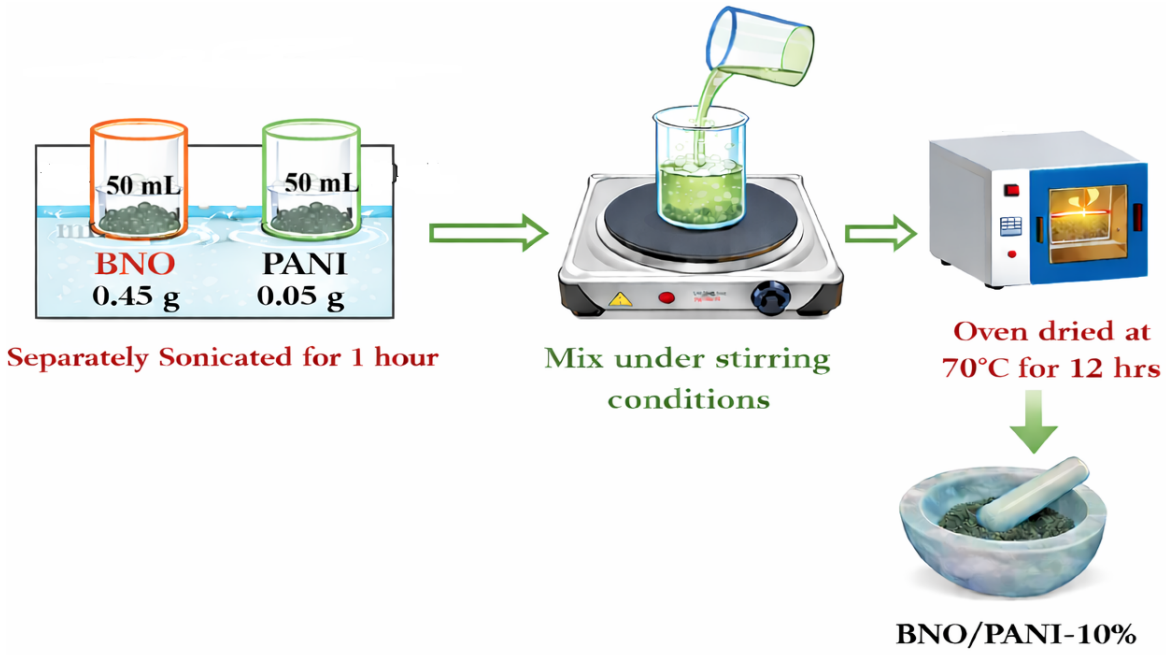

Figure 3.4: Schematic illustrations of steps for preparation of BNO/PANI-10% nanocomposites.

Initially, 0.45 g of BNO and 0.05 g of PANI were utilized from the synthesized sample. They were individually dispersed in 50 mL of deionized water and subjected to sonication for 1 hour to ensure complete dispersion. Subsequently, the suspensions containing BNO and PANI were

mixed under stirring and heated continuously to facilitate solvent evaporation. Once the solvent had completely evaporated, the composite was dried overnight in an oven at 70^oC. The dried samples were then ground in an agate mortar, and the resulting BNO/PANI sample was designated as BNO/PANI-10%. The same procedure was used for the synthesis of both 20% and 30% addition of PANI in the BNO nanoparticle. Then, the samples prepared with different mass ratios of PANI were labelled as BNO/PANI-10, BNO/PANI-20, and BNO/PANI-30. The content of PANI in BNO/PANI-10, BNO/PANI-20, and BNO/PANI-30 was calculated as 10wt%, 20wt%, and 30wt%, respectively.

3.2.8 Synthesis of SnO_2/BNO/PANI Nanocomposites

The SnO_2/BNO/PANI composites were synthesized using ultra-sonication assisted technique. First, 0.5 g of SnO_2, 0.4 g of BNO, and 0.1 g of PANI were separately dispersed in 50 mL of deionized water and sonicated for 1 hr to accelerate full dispersion. SnO_2, BNO, and PANI suspensions were combined while being stirred, and the mixture was heated constantly to accelerate the evaporation of the solvent. After the solvent had evaporated completely, the composite was placed in an oven to dry. An agate mortar was used to grind the dried samples into a uniform SnO_2/BNO/PANI nanocomposite.

3.2.9 Preparation of Electrode Materials

The formulation and mixing processes were critical for achieving optimal performance while producing working electrodes for supercapacitor applications. The working electrodes were created using a precisely tuned composition that included 80% active material, 10% polyvinylidene fluoride (PVDF) binder, and 10% carbon black. N-methyl-2-pyrrolidone (NMP) was utilized as the solvent to generate homogenous slurry, which was subsequently coated onto a piece of stainless steel using the doctor blade technique and dried in an oven at 80^oC overnight (see Fig. 3.5) (Srivastava et al., 2025). In the three-electrode configuration, the working electrode was prepared with an effective active mass for all electrodes was approximately 3 mg.

The asymmetric supercapacitor (ASC) devices were assembled in a Swagelok cell configuration as a two-electrode system, using the working electrodes as the positive electrode and activated carbon (AC) as the negative electrode, with 1 M H_2SO_4 used as the electrolyte, as shown in Fig. 3.6.

3.3 Characterizations

The structural and physicochemical properties of the synthesized nanoparticles were comprehensively investigated using a various characterization techniques, including XRD, SEM, EDX,

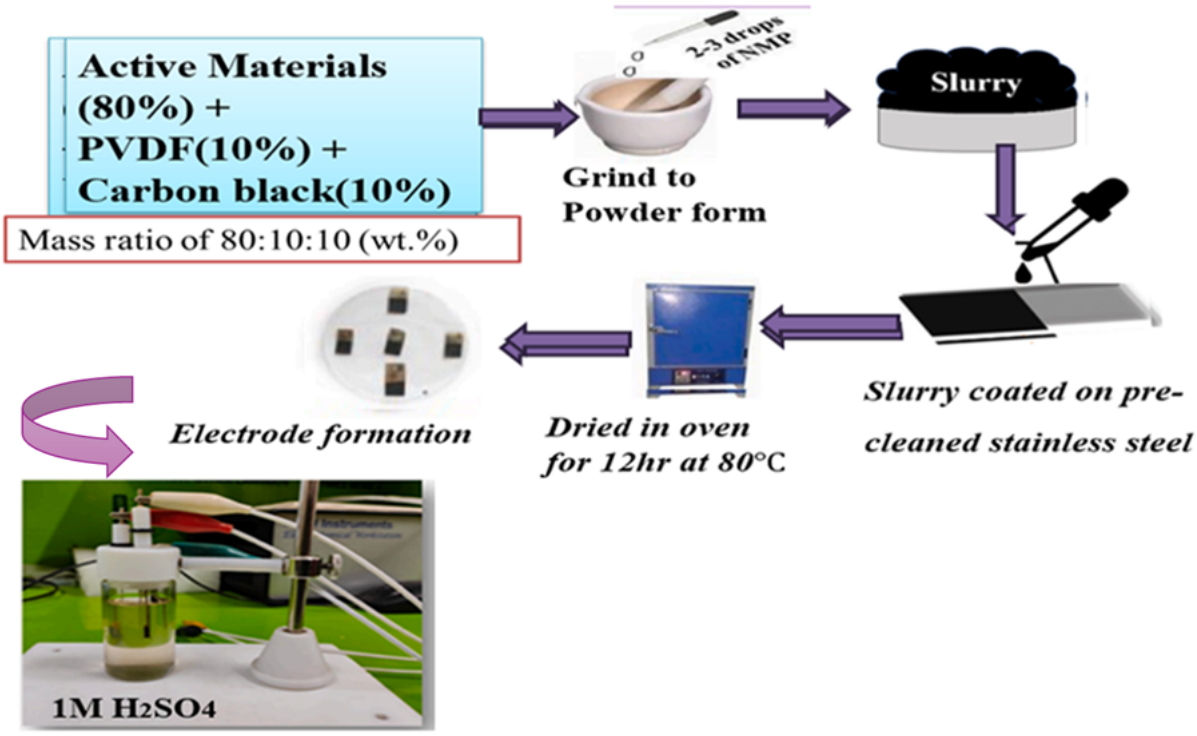

Figure 3.5: Schematic illustrations of steps for electrode materials preparation and three electrode setups.

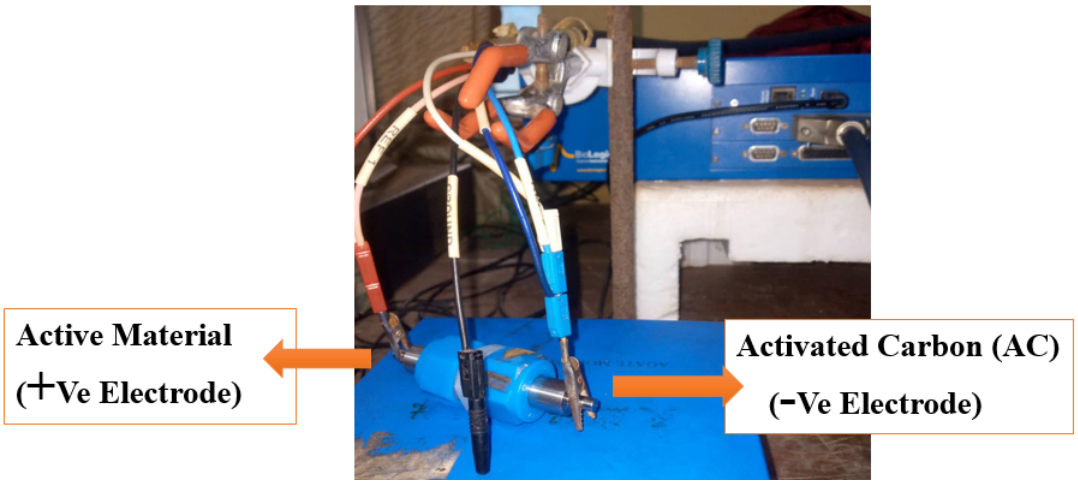

Figure 3.6: Two-electrode setup using a swagelok cell configuration.

TEM, and FTIR. Structural analysis and crystallite size determination were carried out using a DW-XRD-2700A diffractometer (Drawell, China), operated at 40 kV and 30 mA, with Cu-Kα radiation (λ = 0.154 nm) as the X-ray source. The chemical bonding and functional groups present in the samples were analysed by employing a 4600 type-A Fourier transform (FTIR)

instrument (Perkin Elmer,USA), FTIR spectroscopy is a versitle non-destructive technique used to identify functional groups present in the synthesized nanomaterials in the spectra range of 4000-400 cm^{-1}. Scanning electron microscope-Energy dispersive X-ray spectroscopy (JEOL, Japan) was used for morphology and elemental composition analysis. A scanning electron microscop (SEM) was used for high-resolution imaging of surfaces to determine the morphology of samples. A single-beam UV-visible spectrophotometer (UV-vis, V-770, Chana) was used to determine the optical properties of the samples.

The electrochemical performance was evaluated using a Biologic VSP 300 Potentiostat (Bio-Logic Science Instruments, France). The electrochemical performance of the synthesized materials was initially evaluated using a standard three-electrode setup. In this configuration, an Ag/AgCl electrode was used as the reference electrode, while a Pt wire functioned as the counter electrode. The working electrodes were fabricated by coating the synthesized materials onto stainless steel substrates using a doctor blade technique to ensure good electrical contact and mechanical stability. A 1 M H_2SO_4 aqueous solution was employed as the electrolyte due to its high ionic conductivity and compatibility with acidic systems. cyclic voltammetry (CV) and galvanostatic charge–discharge (GCD) techniques were used to assess charge storage capacity, efficiency, redox behavior, and electrochemical kinetics.The electrochemical measurements were conducted within a suitable potential window of 0 to 0.9 V versus Ag/AgCl, selected to prevent electrolyte decomposition and ensure stable redox behavior of the electrode materials. Electrochemical impedance spectroscopy (EIS) was also conducted to evaluate the resistance and capacitive behavior, offering a comprehensive understanding of the material's electrochemical properties.

CHAPTER 4

RESULTS AND DISCUSSION

4.1 X-ray Diffraction (XRD) Result Analysis

X-ray diffraction (XRD) analysis was conducted to determine the phase structure, crystallinity, and average crystallite size of the synthesized nanomaterials, including pure SnO_2, BNO, PANI, as well as their binary and ternary nanocomposites. The XRD pattern of SnO_2 exhibited prominent diffraction peaks at 2θ values of 26.6°, 34.2°, 37.9°, 51.8°, 54.8°, 62°, and 66.2°, corresponding to specific Miller indices of (110), (101), (200), (211), (220), (310), and (301), respectively, as shown in Fig. 4.1 (a). These reflections confirm the tetragonal rutile structure of SnO_2, matching the standard card (JCPDS# 01-077-0447), with lattice constants a = b = 4.736 Å and c = 3.185 Å in the $P4_2/mnm$ space group. The crystallite sizes were determined using Eq.2.18. The relatively broad diffraction peaks confirm the nanocrystalline nature of the material, and the average crystallite size of SnO_2 was calculated to be 11.10 nm, as summarized in Table 4.1. The lattice parameters calculated using Eq. 2.20, were a = b = 4.679 Å, and c = 3.145Å, which are in good agreement with the standard JCPDS values.

The XRD pattern of pure PANI exhibited a broad, low-intensity peak centered on 2θ = 23-25.5°, confirming its amorphous nature as shown in Fig. 4.1(b) below. This observation is in agreement with previously reported results in the literature (Vadiraj & Belagali, 2015). The absence of sharp diffraction features indicates that PANI does not form well-ordered crystalline domains.

Table 4.1: The crystallite size and d-spacing of SnO_2 nanoparticles were calculated from the XRD data.

Sample	2θ (°)	hkl	FWHM (rad)	K	λ (Å)	d-spacing (JCPDS card) (Å)	$d = \lambda/2\sin\theta$ (Å)	D (nm)	Average D (nm)
	26.6	110	0.017485	0.9	1.54	3.34872	3.282	8.15	
	34.2	101	0.015425	0.9	1.54	2.64295	2.610	9.40	
SnO_2	37.9	200	0.019558	0.9	1.54	2.3679	2.336	7.50	11.10
	51.8	211	0.007992	0.9	1.54	1.76361	1.747	19.32	
	54.8	220	0.01591	0.9	1.54	1.67436	1.662	9.83	
	62.0	310	0.013064	0.9	1.54	1.49759	1.487	12.40	

The binary nanocomposites, SnO_2/PANI with varying PANI weight percentages (10%, 20%, and 30%), displayed noticeable changes in their diffraction patterns as shown in Fig. 4.1(c-e).

While the primary peaks of SnO_2 were still visible, their intensity decreased, and the peaks became broader as the PANI content increased. No new diffraction peaks associated with PANI appeared, reaffirming its amorphous character within the composite. This suppression of peak intensity and broadening is attributed to the PANI coating on SnO_2 nanoparticles, which limits crystal growth. The calculated crystallite sizes for SnO_2/PANI nanocomposites were 7.55 nm for 10% PANI, 6.3 nm for 20% PANI, and 4.9 nm for 30% PANI, suggesting that the incorporation of PANI inhibits the crystallization of SnO_2 and promotes better nanoscale dispersion.

The XRD pattern of BNO showed sharp and intense peaks at the 2θ values of 12.6°, 25.87°, 29.36°, 32.52°, 33.48°, 36.5°, 41.03°, 46.9°, 49.74°, 54.16°, 55.16°, 58.68°, and 68.21° correspond to the (300), (111), (411), (020), (002), (800) (502), (022), (802), (431), (413), (822), and (004) crystallographic planes, respectively, and agree to the orthorhombic phase of BNO as shown in Fig. 4.1(f). These results are consistent with the standard card of (JCPDS No.98-011-3875), with lattice $a = 21.011$ Å, $b = 5.4630$ Å, and $c = 5.4730$ Å in the pnc2/30 space group, demonstrating the high crystallinity of the sample. The average crystallite size of pristine BNO was found to be 25.85 nm as shown in Table 4.2. By using Eq. 2.21, the orthorhombic crystal structure of BNO lattice parameters are calculated, and its values are a = 21.10 Å, b = 5.50 Å, and c = 5.34 Å, which well matches with JCPDS file.

The binary composites (BNO/PANI) with PANI content of 10%, 20%, and 30%, the XRD patterns showed that the overall crystalline structure of BNO was maintained, as shown Fig. 4.1(g-i). However, with increasing PANI content, the diffraction peaks became slightly broader, reduced in intensity, and shifted slightly to lower angles. These changes indicate that PANI is well integrated into the BNO matrix without altering its fundamental structure. The calculated crystallite sizes for the BNO/PANI composites were 26.43 nm, 23.17 nm, and 19.07 nm for 10%, 20%, and 30% PANI loadings, respectively. This trend suggests that the incorporation of PANI exerts a two-stage influence on the crystallinity of BNO. At a low PANI content (10%), the slight increase in crystallite size may be attributed to a surface stabilizing effect, where in PANI helps regulate crystal growth by suppressing unwanted nucleation events. However, as the PANI concentration increases to 20% and 30%, its amorphous and polymeric nature appears to hinder further crystallite growth. The expanded polymer matrix likely interferes with the crystallization process through spatial confinement, leading to a progressive reduction in particle size.

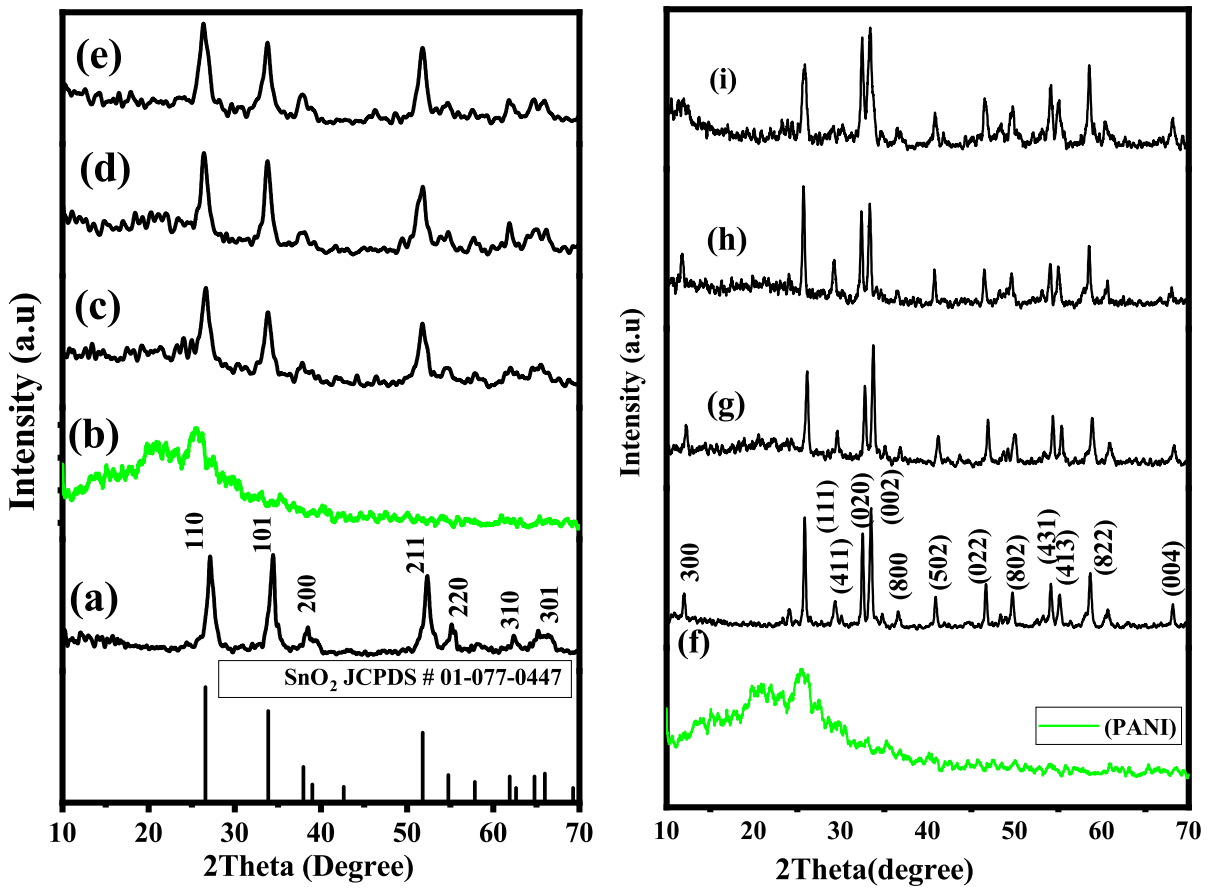

Figure 4.1: XRD patterns of (a) SnO_2, (b) PANI, (c) SnO_2/PANI-10%, (d) SnO_2/PANI-20%, (e) SnO_2/PANI-30%, and (f) BNO, (g) BNO/PANI-10%, (h) BNO/PANI-20%, and (i) BNO/PANI-30%.

Table 4.2: The average crystallite size and d-spacing of BNO nanoparticles were calculated from the XRD data

Sample	2θ (°)	hkl	K	λ (Å)	FWHM (rad)	D (nm) = 0.9λ/(β cos θ)	d-spacing (JCPDS card)(Å)	d (Å) = λ/2 sin θ	Average D (nm)
BNO	29.36	411	0.9	1.54	0.007824	18.31	3.11	3.04	25.85
	32.52	020	0.9	1.54	0.004827	29.90	2.736	2.75	
	33.48	002	0.9	1.54	0.005978	24.21	2.732	2.67	
	41.03	502	0.9	1.54	0.005045	29.32	2.29	2.20	
	46.90	022	0.9	1.54	0.004818	31.33	1.93	1.94	
	49.74	802	0.9	1.54	0.006177	24.72	1.89	1.83	
	54.16	431	0.9	1.54	0.006041	25.76	1.464	1.69	
	55.16	413	0.9	1.54	0.00673	23.23	1.441	1.66	
	58.68	822	0.9	1.54	0.00595	26.72	1.556	1.57	

The XRD pattern of the binary SnO_2/BNO composite exhibited distinct diffraction peaks cor-

responding to both SnO_2 and BNO phases, confirming the successful formation of a composite material, as shown in Fig. 4.2(d). All the characteristic peaks of pure SnO_2 and BNO were present in the SnO_2/BNO pattern, indicating that the structural integrity of each component was retained after composite formation. This also suggests a good combination between SnO_2 and BNO without the formation of any new impurity phases.

The ternary SnO_2/BNO/PANI composite showed a diffraction pattern containing features from both SnO_2 and BNO, while the broad amorphous peak associated with PANI remained centered on $2\theta \approx 23 - 25.5^{\circ}$. In this sample, the characteristic peaks of SnO_2 and BNO were still present but significantly reduced in intensity and slightly broadened, indicating strong interfacial interactions between the three components as shown in Fig. 4.2(e).

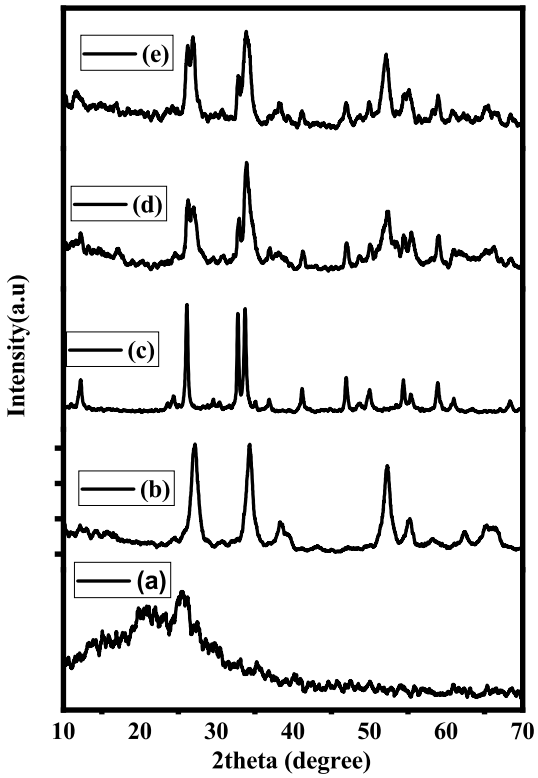

Figure 4.2: XRD of (a) PANI, (b) SnO_2, (c) BNO, (d) SnO_2/BNO, and (e) SnO_2/BNO/PANI Nanoparticles

The absence of new peaks and the shift in existing ones suggest a well-integrated composite structure without the formation of new crystalline phases. The average crystallite sizes for SnO_2/BNO and SnO_2/BNO/PANI composites were calculated to be 20.38 nm and 14.32 nm, respectively. The ternary composite exhibited an intermediate crystallite size compared to its individual and binary counterparts, reflecting a balance between crystallinity and structural integration. This suggests a synergistic effect in which PANI serves as a flexible, amorphous matrix

that stabilizes metal oxide nanoparticles, optimizing both surface area and particle dispersion.

4.2 FT-IR Spectra Analysis

Fourier-transform infrared (FT-IR) spectroscopy was employed to examine the functional groups that are present in pristine SnO_2, BNO, PANI, as well as their binary and ternary nanocomposites. The spectra confirmed the successful synthesis of each component and the integration of individual phases in the composite systems, as presented in Fig. 4.3 and 4.4. The FT-IR spectrum of SnO_2 displayed two prominent absorption bands, and a strong peak at approximately 628 cm^{-1}, corresponding to Sn-O-Sn stretching vibrations, and a broad peak around 3500 cm^{-1}, attributed to the O-H stretching and bending vibration which is due to the re-adsorption of water from the ambient atmosphere, as shown in Fig. 4.3(a). These features are consistent with typical metal oxygen bonding patterns in SnO_2 nanoparticles (Chetri & Choudhury, 2013).

The FT-IR spectrum of pure PANI confirmed the successful polymerization of aniline into its emeraldine salt form through the presence of several characteristic absorption bands. Prominent peaks were observed at 1638 cm $^{-1}$ and 1538 cm^{-1}, corresponding to C=C stretching vibrations of quinoid and benzenoid rings, respectively as shown in Fig. 4.3(a,b). These peaks are indicative of the polymer's redox activity and structural regularity. An additional absorption peak appeared at 1290 cm^{-1} and 1125 cm^{-1}, which are attributed to the C-N stretching amine group and C-H bending of quinoid and benzenoid rings respectively (Gospodinova & Terlemezyan, 1998; Sanches et al., 2015). O-H stretching at 3500 cm^{-1}, C-H stretching at 2350 cm $^{-1}$, and $C \equiv N$ stretching at 2109 cm^{-1} were among the additional notable peaks in the spectra that were indicative of PANI. The N=Q=N stretching vibration detected at 1117 cm^{-1} is particularly significant since it indicates that PANI is in its emeraldine oxidation state, which is the most conductive form of the polymer (Laska et al., 2002; Roy et al., 2020).

In the FTIR spectra of SnO_2/PANI-X nanocomposites, all the major characteristic vibrational bands of PANI were still clearly visible, indicating that the introduction of SnO_2 did not affect the basic functional groups of the polymer, as shown in Fig. 4.3(a). This retention of bands confirms that the composite formation was successful without affecting the typical functional groups in PANI.

The FT-IR analysis of BNO, synthesized using *V. Amygdalina* plant extract, shown distinct spectral features. The presence of metal–oxygen bonding was confirmed by a peak at 635 cm^{-1}, corresponding to Bi–O and Nb–O stretching vibrations, indicating the metal-oxide network characteristic of the BNO structure. Additionally, peaks observed at 2350 cm^{-1} and 2096 cm^{-1} are attributed to C–H and C≡N stretching vibrations, respectively, as shown in Fig. 4.3(b), which was also appear in SnO_2 nanoparticle. These features are likely due to the incorporation of

organic residues from the plant extract, suggesting that some phytochemical components were retained during the synthesis process.

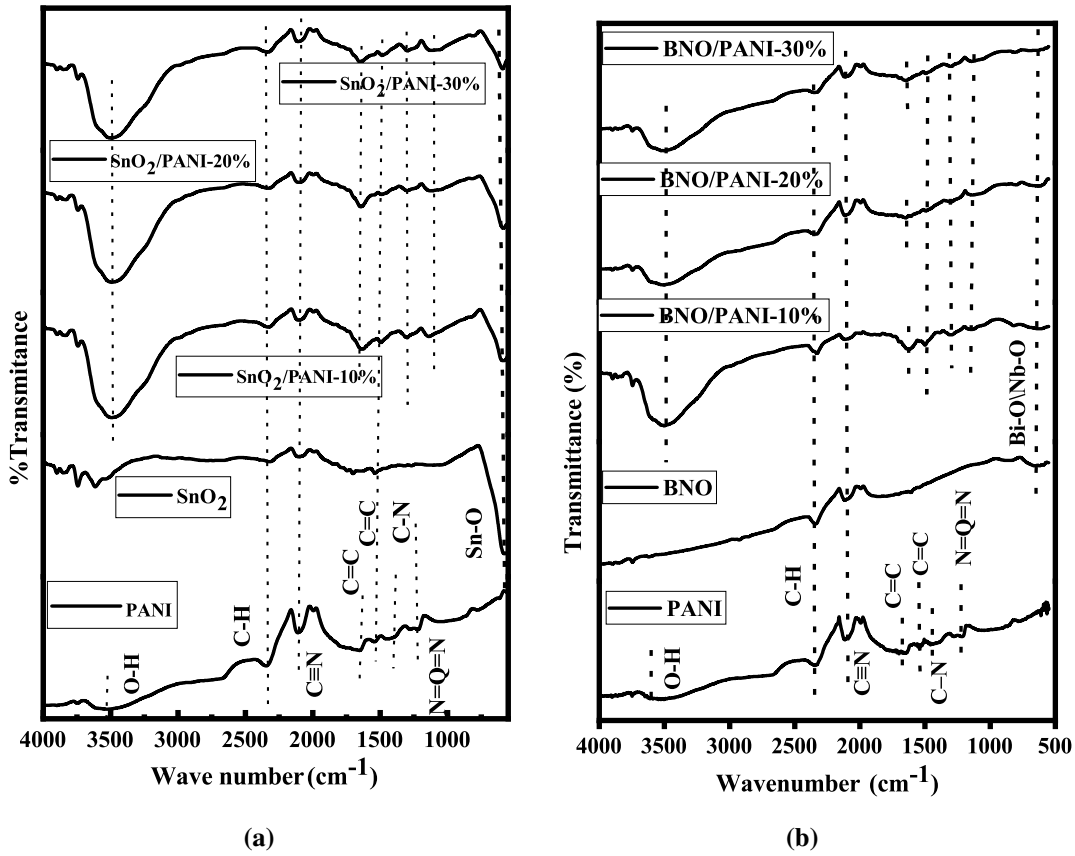

Figure 4.3: FT-IR of (a) PANI, SnO_2, and SnO_2/PANI-X, and (b) PANI, BNO, and BNO/PANI-X Nanoparticles

In the BNO/PANI binary nanocomposites, the FT-IR spectra confirmed the coexistence of characteristic features from both BNO and PANI, indicating successful integration of the two materials, as shown in Fig. 4.3(b). The presence of absorption bands corresponding to O-H stretching, C-H stretching, C $\equiv$ N stretching, quinoid and benzenoid C=C vibrations, and N=Q=N stretching collectively confirms the incorporation of PANI within the composite.

In the SnO_2/BNO, the FT-IR spectra shows the presences of characteristic peaks from both SnO_2 and BNO, as shown in Fig. 4.4, indicating the successful integration of both materials.

The ternary SnO_2/BNO/PANI nanocomposite spectrum displayed all the characteristic peaks associated with each component, confirming their successful integration into a single material as shown in Fig. 4.4. However, peak broadening were observed in comparison to the pristine components, which suggest strong interfacial interactions and effective blending at the molecu-

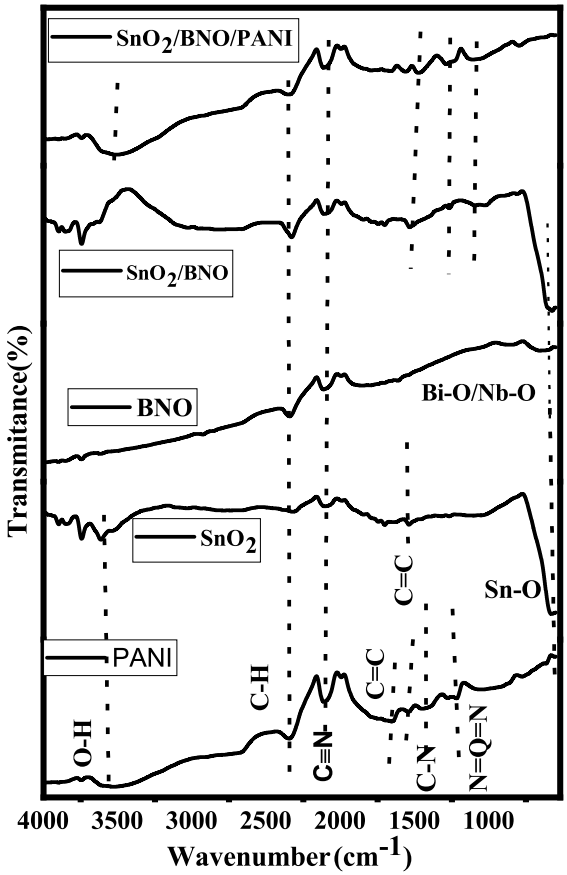

Figure 4.4: FT-IR of PANI, SnO_2, BNO, SnO_2/BNO, and SnO_2/BNO/PANI Nanoparticles

lar level. Therefore, the successful syntheses of both binary and ternary nanocomposites, as well as the formation of strong intermolecular interactions, were confirmed by the FT-IR analysis.

4.3 Scanning Electron Microscopy (SEM) Analysis

4.3.1 SEM Analysis SnO_2, PANI, Binary Composites (SnO_2/PANI-X)

The morphology of the synthesized samples was analyzed using SEM in the range of micrometric sizes. Figure 4.5 (a-e) displays SEM images of the pristine PANI, SnO_2, and SnO_2/PANI-X (X = 10 wt.%, 20 wt.%, and 30 wt. %) composite materials. The SEM image of pristine PANI, shown in Fig. 4.5 (a), illustrates a cauliflower-like granular morphology, which is the characteristic form of PANI synthesized in acidic aqueous media (Jia & Zhang, 2016). The pristine SnO_2 demonstrates a clustered nanorod-like morphplogy as shown in Fig. 4.5 (b), and upon incorporating PANI into the SnO_2 nanoparticle, a mixture of both granular and nanorod morphologies can be seen in the composite, as illustrated in Fig. 4.5 (c-e).

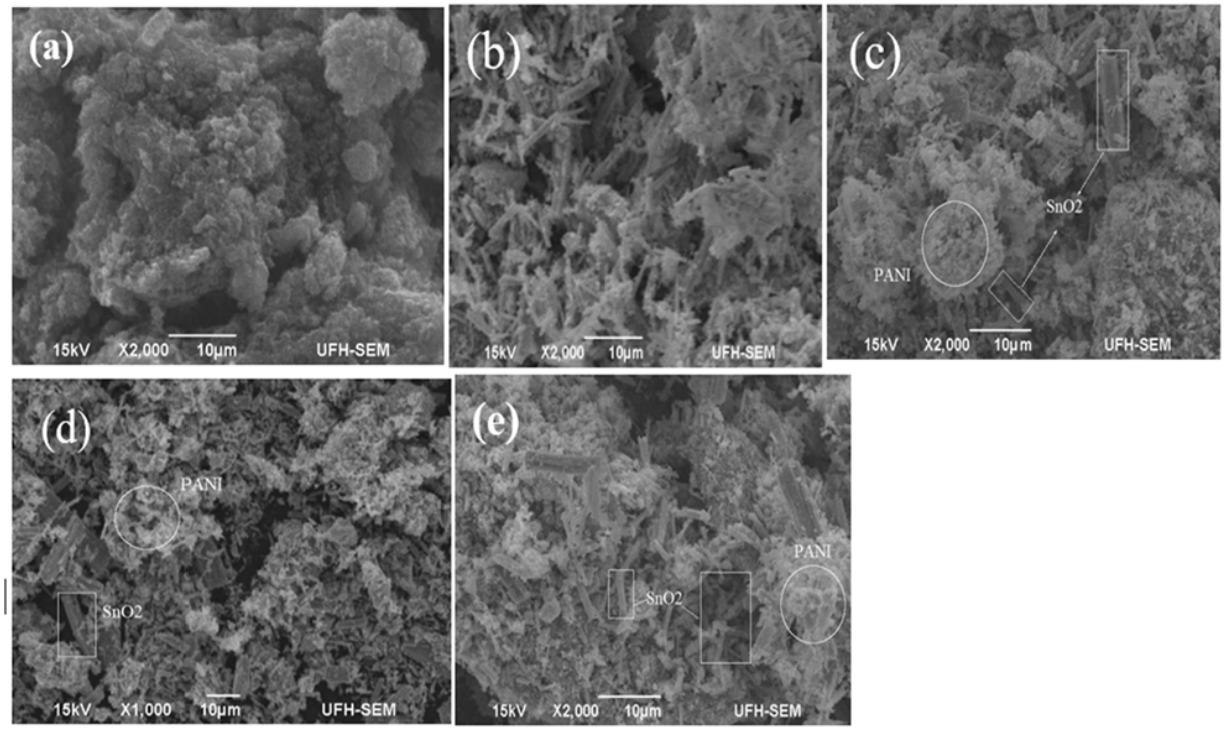

Figure 4.5: SEM image of (a) PANI, (b) SnO_2, (c) SnO_2/PANI-10%, (d) SnO_2/PANI-20%, (e) SnO_2/PANI-30%.

4.3.2 SEM Analysis of BNO and BNO/PANI-X Nanocomposites

SEM images of pristine BNO and BNO/PANI-X composite materials are shown in Fig. 4.6 (a-d). The pristine BNO exhibits agglomerated nanorod-like morphology (Fig. 4.6 (a)), and with the introduction of PANI into the BNO matrix, a combination of both granular and nanorod structures is observed in the composite, as depicted in Fig. 4.6 (b-d). As the PANI content increases from 10 wt% to 30 wt%, the composite displays a more pronounced granular morphology, indicating the well-distribution of PANI within the composite, as shown in Fig. 4.6 (b-d).

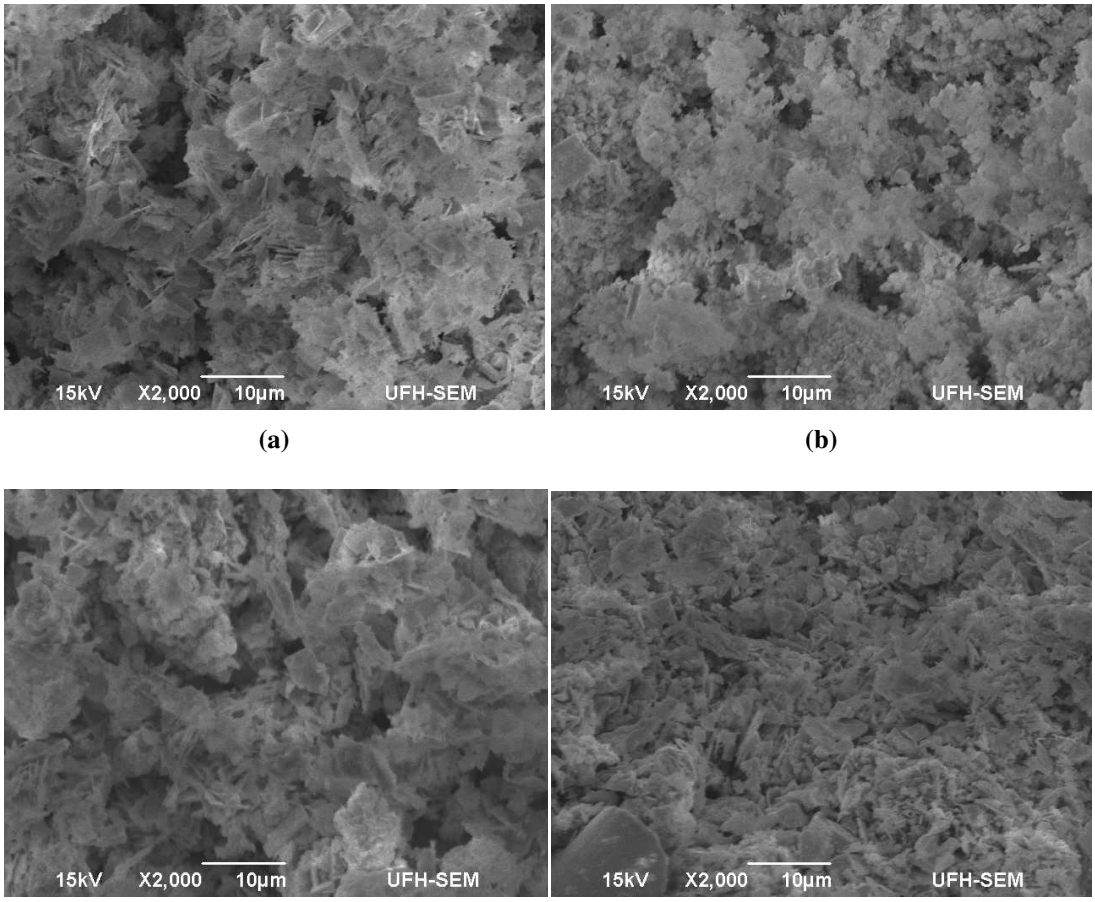

(a) **(b)**

(c) **(d)**

Figure 4.6: SEM image of (a) BNO, (b) BNO/PANI-10%, (c) BNO/PANI-20%, (d) BNO/PANI-30%.

4.3.3 SEM Analysis of Binary (SnO_2/BNO), and Ternary (SnO_2/BNO/PANI) Nanocomposites

The binary SnO_2/BNO nanocomposite exhibits a well-integrated structure, as illustrated in Fig. 4.7 (a). In this image, nanorod-shaped SnO_2 particles are visible alongside agglomerated nanorod bundles of BNO, indicating successful combination and uniform dispersion of both components within the composite matrix.

The ternary SnO_2/BNO/PANI nanocomposite (Fig. 4.7(b)) demonstrates a well-integrated structure, where the granular PANI, SnO_2 nanorods, and BNO nanorods are uniformly distributed. This homogeneous dispersion indicates effective synthesis, suggesting strong interfacial interactions among the components. The preserved morphologies of the individual materials within the composite highlight its structural integrity, which is crucial for potential applications requiring synergistic properties.

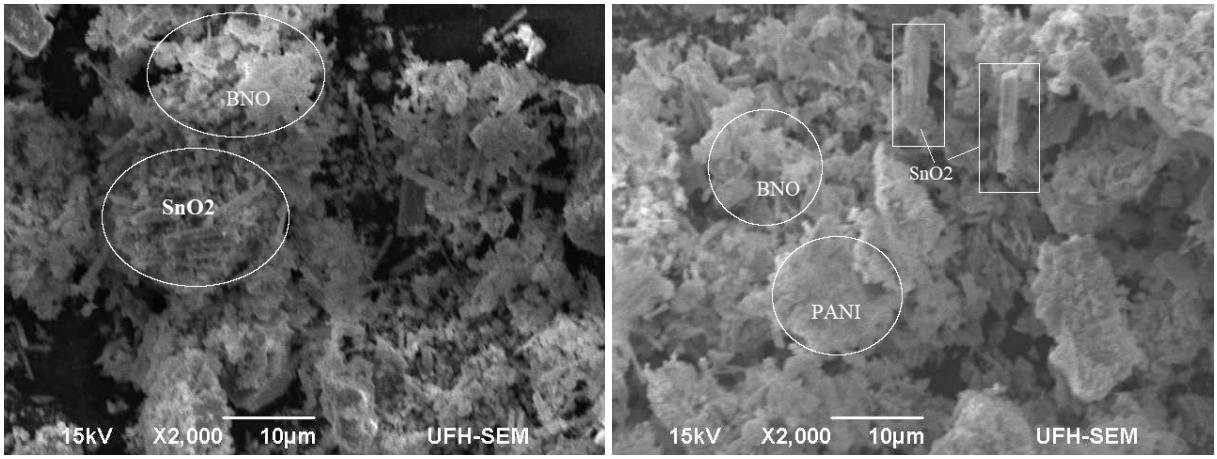

(a) **(b)**

Figure 4.7: SEM image of (a) SnO_2/BNO, (b) SnO_2/BNO/PANI of nanocomposites

4.4 Energy Dispersive X-ray (EDX) Analysis

4.4.1 EDX Analysis of PANI, SnO_2, and SnO_2/PANI-X Nanoparticles

The elemental composition and distribution of elements in the samples were analyzed using energy-dispersive X-ray (EDX) analysis. In Fig. 4.8 (a), the EDX spectrum on the PANI sample is shown, with carbon as the dominant element (55.14,wt%, 71.54 At%), confirming the carbon rich aromatic backbone of the polymer. A substantial nitrogen content (14.41wt%, 16.88At%) verifies the presence of imine (=N–) and amine (–NH–) groups integral to the PANI chain. Oxygen (8.00wt%, 7.18At%) is consistent with partial oxidation or adsorbed moisture, suggesting the polymer exists predominantly in the conductive emeraldine state. The pronounced chlorine signal (16.37wt%, 3.03At%) indicates incorporation of chloride counter ions introduced by hydrochloric acid during oxidative polymerization, while the sulfur detected (6.08wt%, 1.36At%) is attributed to residual sulfate species originating from APS, the common oxidant employed in PANI synthesis. Collectively, these elemental compositions confirm successful fabrication of partially oxidized PANI in its emeraldine salt form, well suited for electrochemical applications.

Tin (Sn) was the most prevalent element, contributing 88.79Wt% and 51.26At% of the SnO_2 nanoparticles synthesized from Vernonia amygdalina leaf extract, according to EDX spectra as shown in Fig. 4.8 (b). The high tin content demonstrates the formation of Sn-based oxide structures. Findings of oxygen at 10.02Wt% and 42.92At% provide confidence in the idea that SnO_2 is nearly stoichiometric. The oxide has successfully formed since the atomic ratio of tin to oxygen is extremely close to the optimal 1:2 ratio. However, surface effects or partial reduction may cause slight variations. Additionally, a trace amount of nitrogen (1.19Wt%, 5.82At%) was

appeared, most likely from phytochemicals in the plant extract that contained it.

The EDX results for the SnO_2/PANI-X composites, illustrated in Fig. 4.8(c-e), confirm that all elements from both PANI and SnO_2 are uniformly distributed across the surface of the nanocomposite, indicating successful integration of PANI into the composite. The analysis of the SnO_2/PANI-10% nanocomposite using EDX showed that Sn was the most common element, making up 89.22wt% and 52.45At%, which confirms that SnO_2 is still the main phase in the composite, as shown in Fig. 4.8 (c). There were 10.35wt% and 45.14At% O, which helps the SnO_2 develop. There were also small amounts of C (0.32wt%, 1.86At%) and N (0.11wt%, 0.55At%) that were likely observed. This shows that 10% PANI was successfully added to the SnO_2 matrix.

The SnO_2/PANI-20% nanocomposite's EDX showed a significant rise in the signals for C and N, indicating that a higher PANI content had been successfully incorporated into the composite matrix, as illustrated in Fig. 4.8 (d). In particular, N and C were found at 3.07 wt% (10.82 At %) and 4.07 wt% (16.70 At%), respectively, to be significantly higher than in the 10% PANI-loaded sample, suggesting a higher level of the organic polymer. At 79.57 wt% (33.09 At%), Sn was still the most abundant element, indicating that SnO_2 is still the main structural and functional phase in the nanocomposite. In agreement with the formation of the SnO_2 oxide lattice, oxygen was also present at 12.78 wt% (39.39 At%). The progressive surface coverage and integration of PANI as its loading increases is reflected in the decrease in Sn and the corresponding increase in C and N.

The EDX analysis of the SnO_2/PANI-30% nanocomposite showed that the amount of C and N increased significantly (Fig. 4.8(e)). Carbon (C) was found at 15.43 wt% (45.16 At%) and N at 5.43 wt% (13.62 At %). These numbers show that more PANI was successfully added to the composite structure, making the organic part more important on the surface. The amount of Sn decreased to 59.11 wt% (17.49 At%) compared to lower PANI loadings, which is because the polymer matrix was covering more SnO_2 particles. Oxygen (O) was found at 13.97 wt% (15.33 At%), which is consistent with the oxide framework of SnO_2, but its atomic proportion is lower because more C and N atoms from PANI are present. Furthermore, the presence of chemical groups related to the synthesis process, possibly originating from APS and HCl, which are frequently used as oxidizing agents during PANI polymerization.

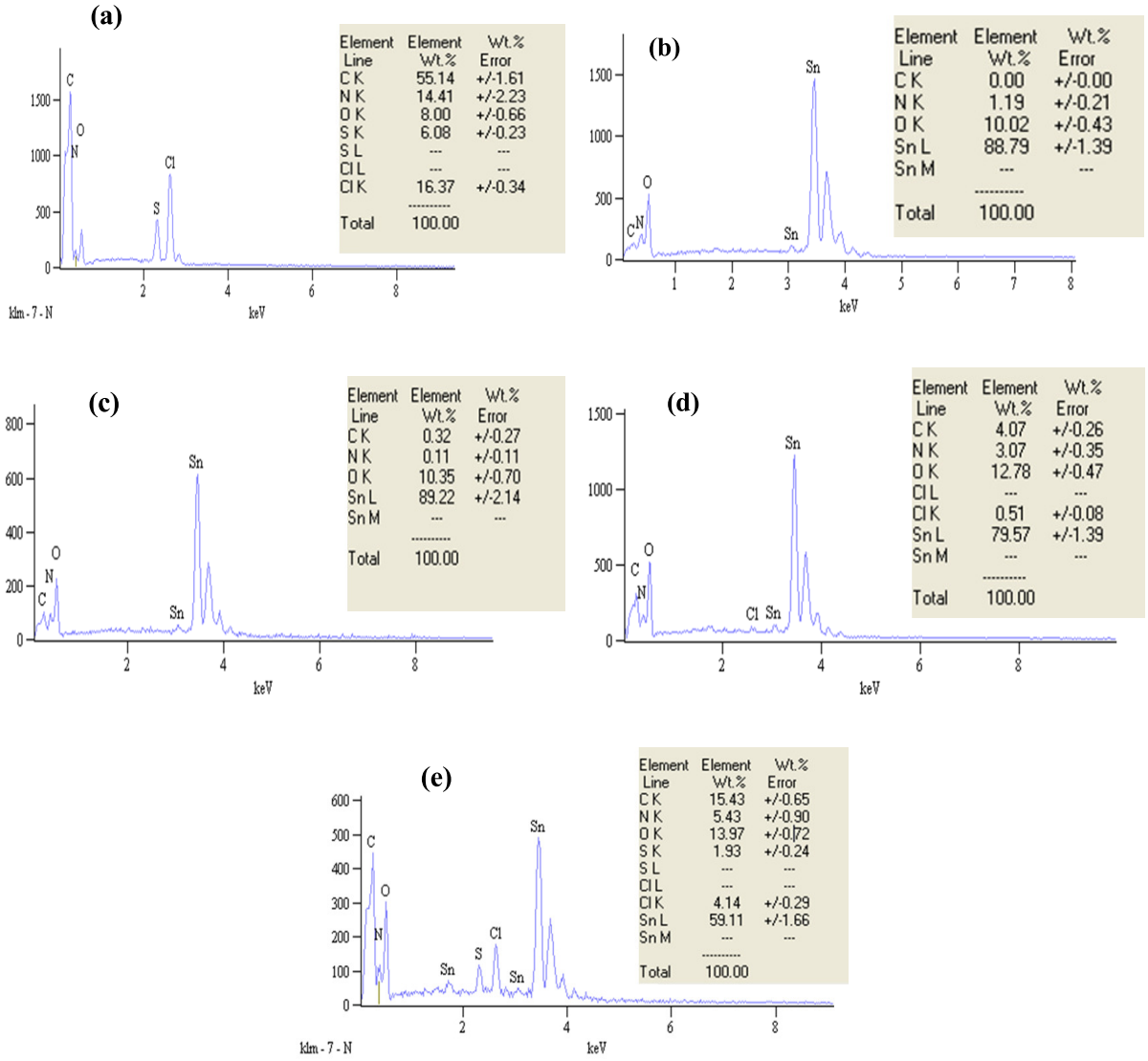

Figure 4.8: EDX pattern of a) PANI, b) SnO_2, c) SnO_2/PANI-10%, d) SnO_2/PANI-20%, and e) SnO_2/PANI-30% Nanoparticles .

4.4.2 EDX Analysis of BNO, BNO/PANI-X Nanoparticles

The elemental composition and spatial distribution of elements within the samples were examined using EDX analysis. In Fig. 4.9 (a), the elemental composition of BNO shows the presence of all expected elements with no detectable impurities. The EDX results for the BNO/PANI-X composites, illustrated in Fig. 4.9 (b-d), confirm that all elements from both PANI and BNO are uniformly distributed across the surface of the nanocomposite, indicating successful integration of PANI into the composite.

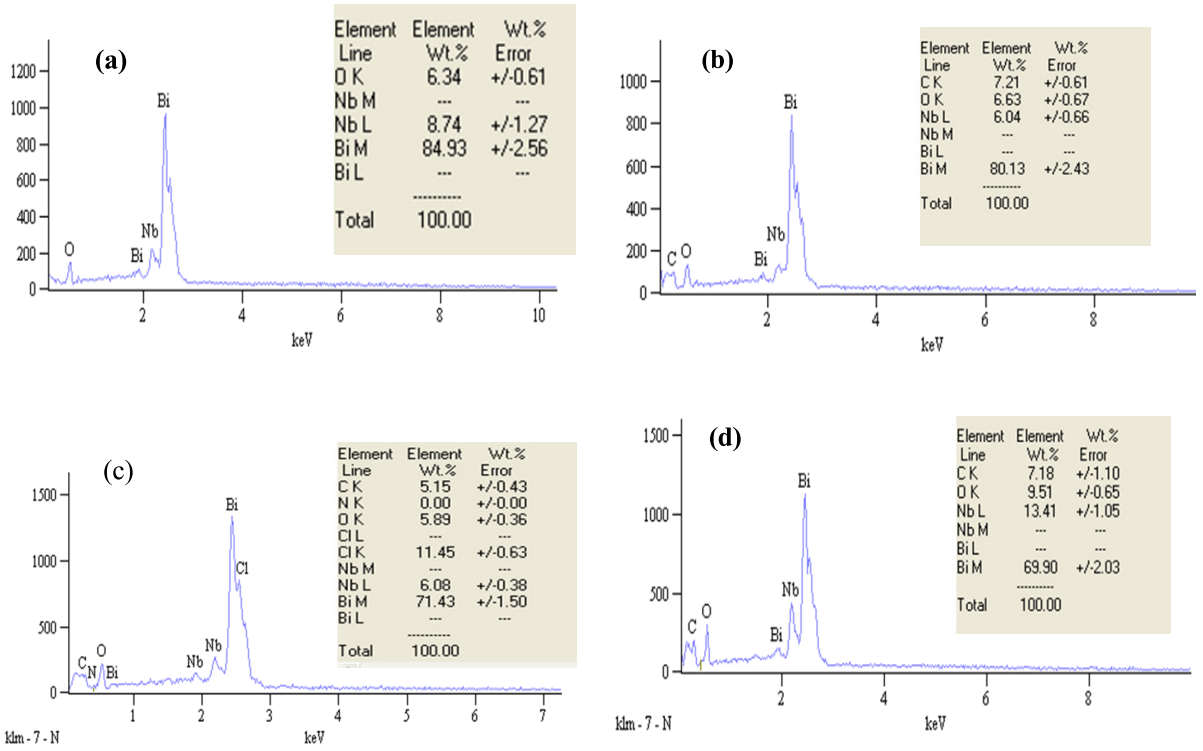

Figure 4.9: a) EDX pattern of a) BNO, b) BNO/PANI-10%, c) BNO/PANI-20%, and d) BNO/PANI-30%.

4.4.3 EDX Analysis of SnO_2/BNO and SnO_2/BNO/PANI Nanocomposites

The existence of all constituent elements is confirmed by the EDX analysis of the SnO_2/BNO nanocomposite, which shows distinct peaks for O (12.28 wt%), Nb (7.11wt%), Sn (52.80wt%), and Bi (27.81wt%) as shown in Fig. 4.10. While the total Bi and Nb levels match the anticipated Bi:Nb ratio for the $Bi_5Nb_3O_{15}$ (BNO) phase, suggesting that its layered perovskite framework is retained in the composite, the prominent Sn signal represents the significant contribution of SnO_2. Complete oxidation of the metallic species is further supported by the measured oxygen content, which comes from both oxides. Importantly, as shown in Fig. 4.10 (a), the spectrum shows no extra peaks, indicating that the synthesis technique created a chemically pure nanocomposite free from observable impurities.

The presence of C (12.17wt%), N (2.73wt%), O (12.07wt%), Nb (9.72wt%), Sn (41.73wt%), and Bi (21.58wt%) was confirmed by EDX analysis of the SnO_2/BNO/PANI ternary nanocomposite, as shown in Fig. 4.10 (b). While the presence of Nb and Bi validates the inclusion of the BNO phase, the detection of C and N shows that the PANI polymer was successfully incorporated. The substantial amount of SnO_2 in the composite is reflected in Sn, which is the dominating element. The oxygen (O) content is in line with each component's oxide nature. No

additional impurity elements were observed, confirming the purity and successful synthesis of the targeted ternary nanocomposite as illustrated in Fig. 4.10 (b).

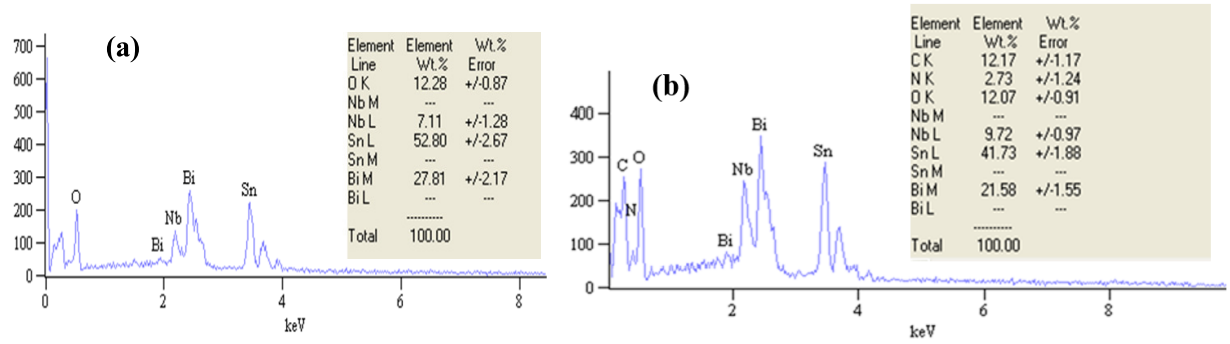

Figure 4.10: EDX pattern of a) SnO_2/BNO, and b) SnO_2/BNO/PANI nanocoposite.

4.5 Transmission Electron Microscopy (TEM) Analysis

Additional analyses were carried out using Transmission Electron Microscopy (TEM) and High-Resolution Transmission Electron Microscopy (HR-TEM) to obtain a better understanding of the internal structure and morphology. Using these methods, the individual SnO_2, BNO, and PANI nanoparticles, as well as their binary (SnO_2/BNO, SnO_2/PANI, BNO/PANI) and ternary (SnO_2/BNO/PANI) nanocomposites, were examined for their specific microstructural characteristics, crystallinity, lattice fringes, atomic-scale orientations, and particle sizes. Critical information about the creation of the composite and material synergy at the nanoscale was obtained by using high-resolution imaging to identify particle size distributions and structural integration between the constituents.

4.5.1 TEM Analysis of PANI, SnO_2, and SnO_2/PANI-X Nanoparticles

Figure 4.11 (a, b) illustrates the distinct morphologies of the individual components, with (a) showing the network-like structure of PANI and (b) displaying the spherical-like morphology of SnO_2 nanoparticles. In Figures 4.11 (d) and 4.12 (a3), 4.13 (b3), and 4.14 (c3), the selected area electron diffraction (SAED) patterns exhibit well-defined diffraction rings with bright spots for SnO_2, SnO_2/PANI-10%, SnO_2/PANI-20%, and SnO_2/PANI-30%, respectively. These concentric rings are characteristic of a polycrystalline structure, confirming the high crystallinity of both the pristine SnO_2 nanoparticles and the SnO_2/PANI nanocomposites with 10%, 20%, and 30% PANI content. These observations are in strong agreement with the XRD analysis results. Specifically, the SAED pattern of pure SnO_2 shows five prominent diffraction rings corresponding to interplanar spacings (d-values) of 0.330, 0.256, 0.221, 0.170, and 0.142 nm. These match

the (110), (101), (200), (211), and (310) crystal planes of SnO_2, respectively, as indicated in Fig. 4.11 (d).

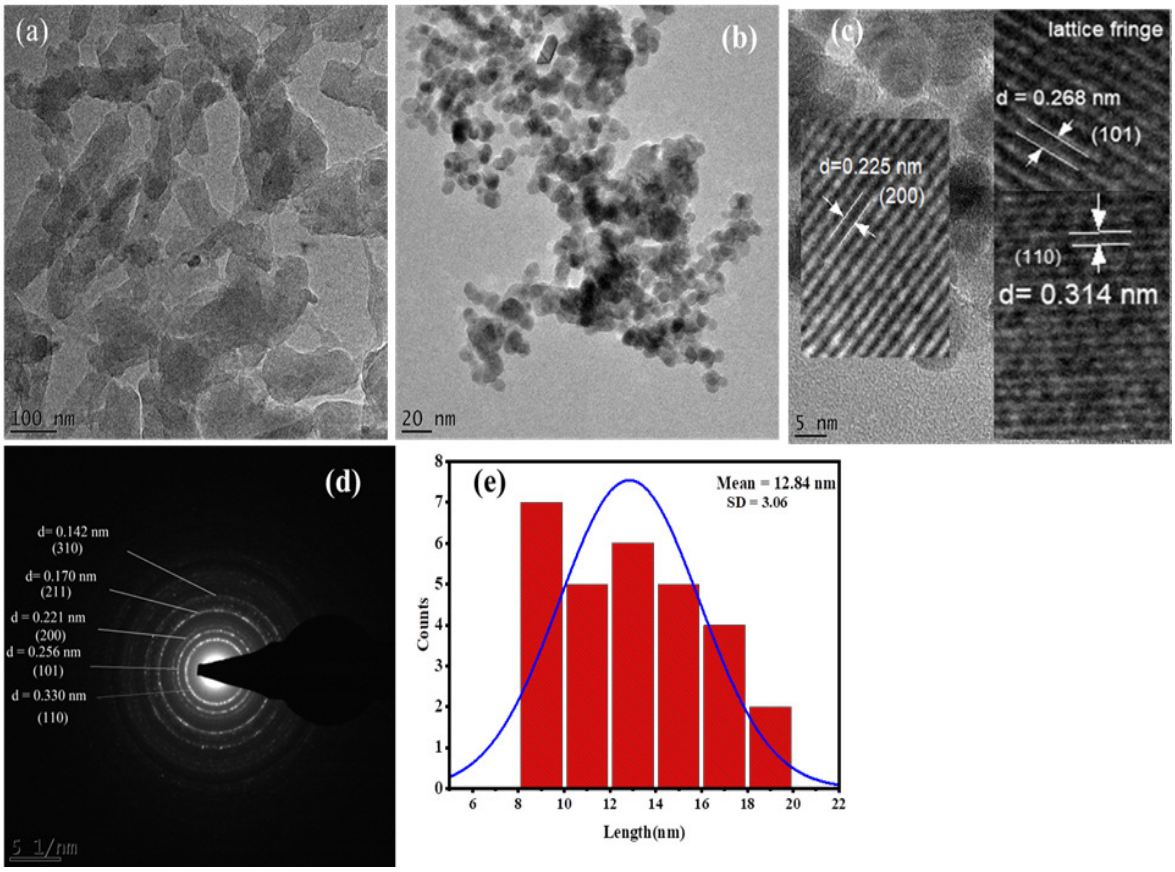

Figure 4.11: TEM image of (a) PANI, (b) SnO_2, (c) HR-TEM image of SnO_2, (d) SAED image of SnO_2, and (e) Average particle size distribution of SnO_2.

The interplanar d-spacing values of the continuous lattice fringes were measured to be approximately 0.314, 0.268, and 0.225 nm, which correspond to the (110), (101), and (200) atomic planes in the SnO_2 nanoparticle, as shown in Fig. 4.11 (c).

Furthermore, in the SnO_2/PANI-10% nanocomposite, five distinct bright rings were observed, corresponding to interplanar spacing (d) values of 0.303, 0.262, 0.232, 0.173, and 0.143 nm, representing the (110), (101), (200), (211), and (310) planes of SnO_2 as shown in Fig. 4.12 (a3). This indicates that the nanocomposite maintains the crystalline structure of SnO_2 after the addition of PANI.

The interplanar d-spacing values determined from the continuous lattice fringes are shown in Fig. 4.12 (a2), 4.13 (b2), and 4.14 (c2) to be approximately 0.344, 0.338 and 0.338 nm for the (110) planes, and 0.258, 0.278, and 0.263 nm for the (101) planes in the SnO_2/PANI-10%,

SnO_2/PANI-20%, and SnO_2/PANI-30% nanocomposites, respectively. The slight differences in d-spacing among these composites, although originating from the same atomic plane, are attributed to the varying amounts of PANI.

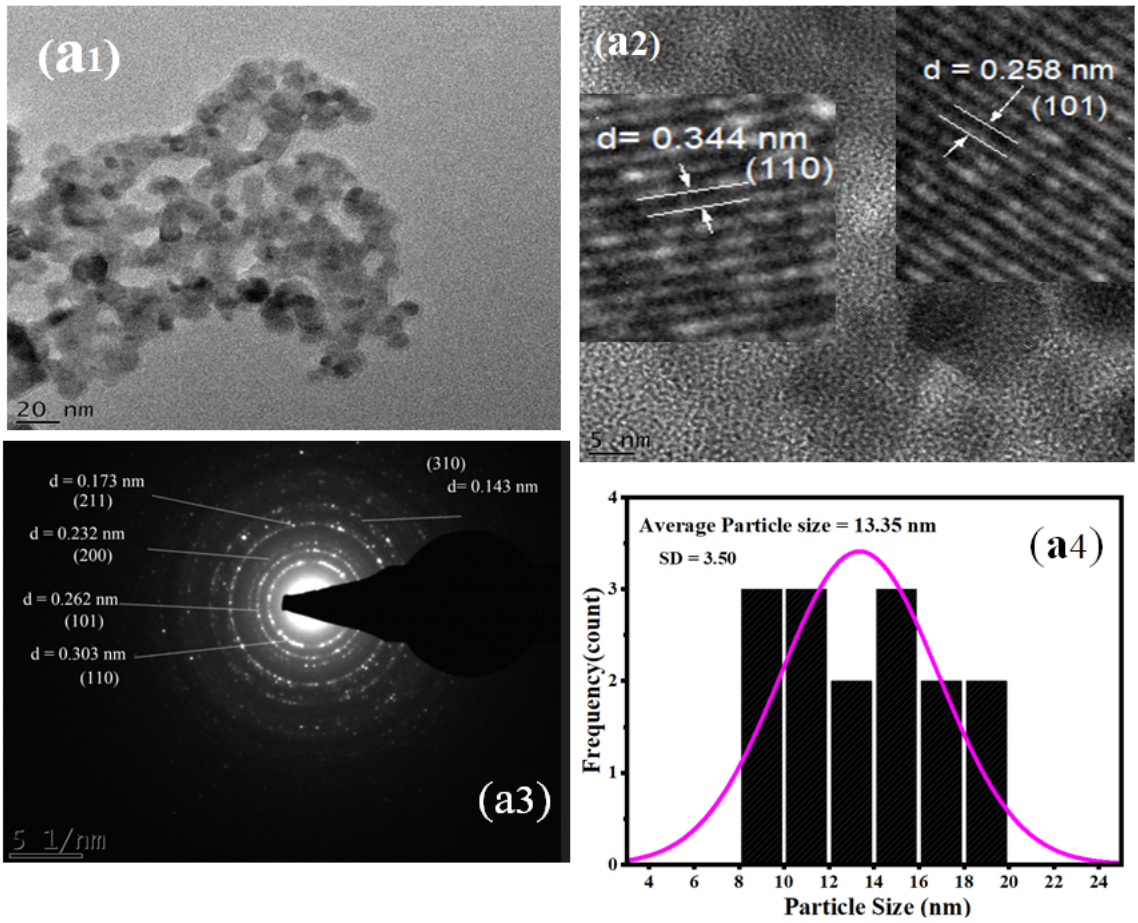

Figure 4.12: TEM image of (a1) SnO_2/PANI-10% at high resolution, (a2) TEM image with inset of HR-TEM; (a3) SEAD image, and (a4) particle size distribution of SnO_2/PANI-10% nanocomposite.

Furthermore, the SAED pattern of the SnO_2/PANI-20% nanocomposite shows four distinct bright diffraction rings with interplanar spacing (d) values of 0.332, 0.259, 0.172, and 0.143 nm, which can be indexed to the (110), (101), (211), and (310) crystallographic planes of SnO_2, respectively (Fig. 4.13 (b3)). This confirms that the crystalline structure of SnO_2 remains well-preserved after the incorporation of PANI. Similarly, the SnO_2/PANI-30% nanocomposite shows four clear diffraction rings with d-spacing values of 0.318, 0.259, 0.175, and 0.145 nm, corresponding to the same (110), (101), (211), and (310) planes, as shown in Fig. 4.14(c3).

Figure 4.11 (e) and Fig. 4.12 (a4), 4.13 (b4), and 4.14 (c4) illustrate the particle size distribution curves of SnO_2 NPs, SnO_2/PANI-10%, SnO_2/PANI-20%, and SnO_2/PANI-30% nanocompos-

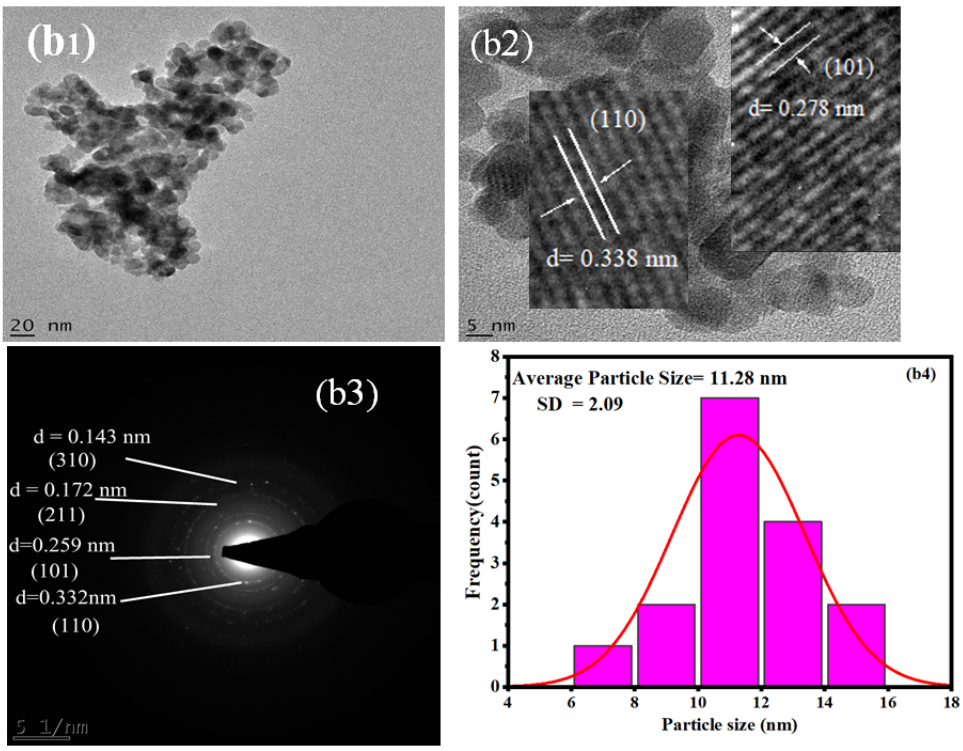

Figure 4.13: TEM image of (b1) SnO_2/PANI-20% at high resolution, (b2) TEM image with inset of HR-TEM; (b3) SEAD image, and (b4) particle size distribution of SnO_2/PANI-20% nanocomposite.

ites respectively. These curves indicate that the majority of nanoparticles fall within the size range of 12-14 nm for SnO_2, SnO_2/PANI-10%, and also 10-12 nm for both SnO_2/PANI-20% and SnO_2/PANI-30% nanocomposites. The particle sizes of SnO_2, SnO_2/PANI-X nanocomposites are 12.84, 13.35, 11.28, and 10.96 nm for SnO_2, SnO_2/PANI-10%, SnO_2/PANI-20%, and SnO_2PANI-30%, respectively, with standard deviations ranging from 2.09 to 3.50 nm. The SnO_2/PANI-10% composite has the largest particle size, possibly due to increased aggregation, while SnO_2/PANI-30% shows the smallest particle size, indicating better dispersion. The relatively low standard deviations suggest uniform particle distributions, with slight variations due to differing PANI contents.

4.5.2 TEM Analysis of BNO and BNO/PANI-X Nanoparticles

Further analysis using TEM and HR-TEM was carried out to examine the intricate microstructure, crystalline characteristics, and atom orientation of BNO and BNO/PANI-X nanocomposites. The TEM image of the layered nanorod crystalline structure of BNO is shown in Fig. 4.15(a). The HR-TEM image as shown in Fig. 4.15 (a), 4.16 (a1, a2), 4.17 (b1, b2), and 4.18 (c1, c2) clearly shows that the nanocomposites are mixed layered aurivillius-phase perovskite struc-

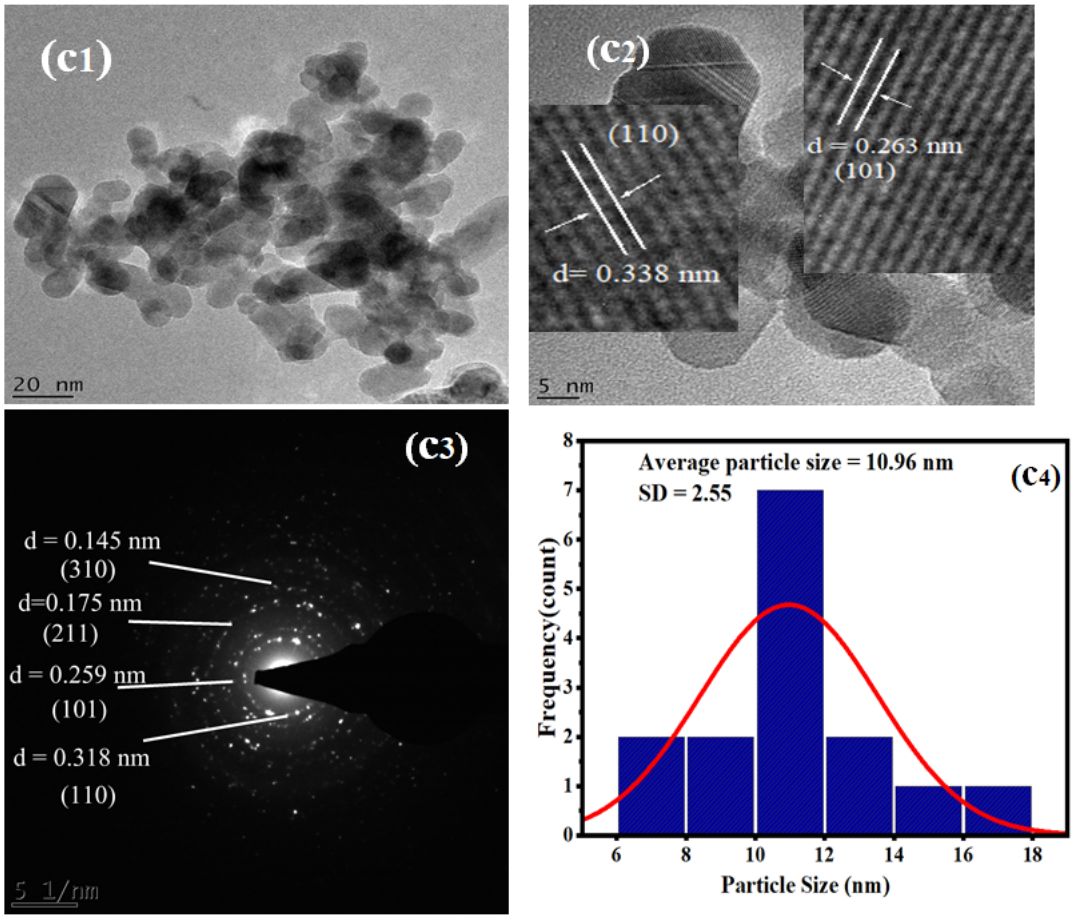

Figure 4.14: TEM image of (c1) SnO_2/PANI-30% at high resolution, (c2) TEM image with inset of HR-TEM; (c3) SEAD image, and (c4) particle size distribution of SnO_2/PANI-30% nanocomposite.

ture, with a significant predominance of BNO, which can be represented by $[Bi_2O_2]$ + $[NbO_4]$ + $[Bi_2O_2]$ + $[BiNb_2O_7]$ (Guo et al., 2011), of BNO, BNO/PANI-10%, BNO/PANI-20%, and BNO/PANI-30%, respectively.

In Fig. 4.15 (c) and Fig. 4.16 (a4), 4.17 (b4), and 4.18(c4), the SAED patterns show clear electron diffraction rings with bright spots, indicating that the BNO, BNO/PANI-10%, BNO/PANI-20%, and BNO/PANI-30% nanocomposites have a high level of crystallinity (polycrystalline), which is consistent with the results of the XRD analysis. The continuous lattice fringes were measured to have interplanar d-spacing values as shown in Fig. 4.15 (b) of approximately 0.355, 0.309, and 0.722 nm, corresponding to the (111), (411), and (300) atomic planes in the BNO nanoparticle, respectively. Specifically, in the BNO nanoparticle, six distinct bright rings corresponding to interplanar spacing (d) values of 3.52, 2.94, 2.68, 2.59, 1.87, and 1.65 Å, representing the (111), (411), (002), (800), (022), and (413) planes, respectively are observed, as shown in

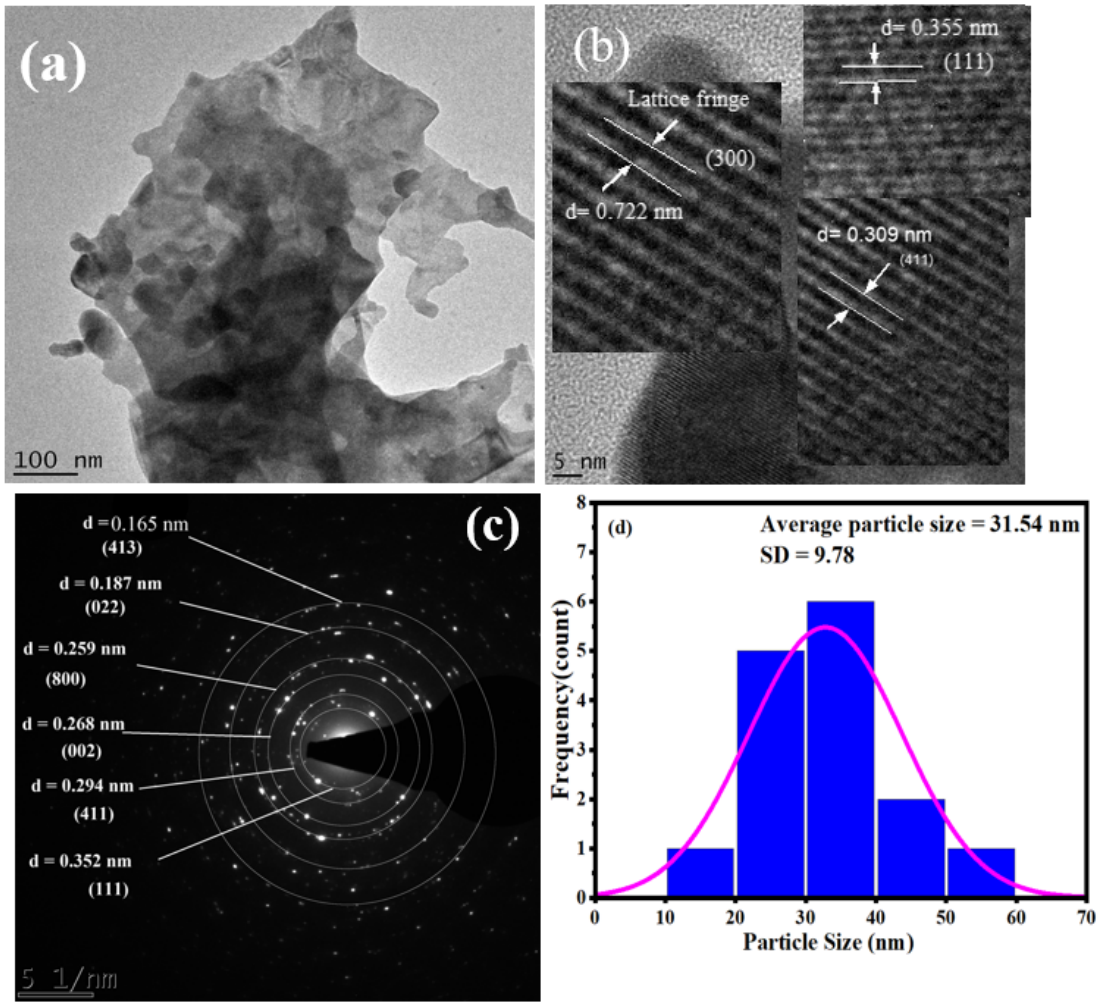

Figure 4.15: TEM image of (a) BNO, (b) HR-TEM image of BNO, (c) SAED image of BNO, and (d) Average particle size distribution of BNO.

Fig. 4.15(c). Additionally, in the BNO/PANI-10% sample, six distinct bright rings corresponding to interplanar spacing (d) values of 3.50, 2.70, 2.25, 1.95, 1.67, and 1.55 Å, representing the (111), (002), (502), (022), (413), and (822) planes of BNO, respectively are obvious, as shown in Fig. 4.16(a4). This suggests that the nanocomposite retains the crystalline structure of BNO even after the incorporation of PANI.

The continuous lattice fringes were measured to have interplanar d-spacing values as shown in Fig. 4.16(a3), 4.17(b3), 4.18(c3) of approximately 0.345, 0.351, and 0.340 nm, corresponding to the (111) atomic plane in the BNO/PANI-10%, BNO/PANI-20%, and BNO/PANI-30% samples, respectively. The variation in d-spacing across these composites, despite being from the same atomic plane, is attributed to the differing percentage of PANI.

The particle size distribution curves as shown in Fig. 4.15 (d) and Fig.4.16 (a5), 4.17 (b5), and

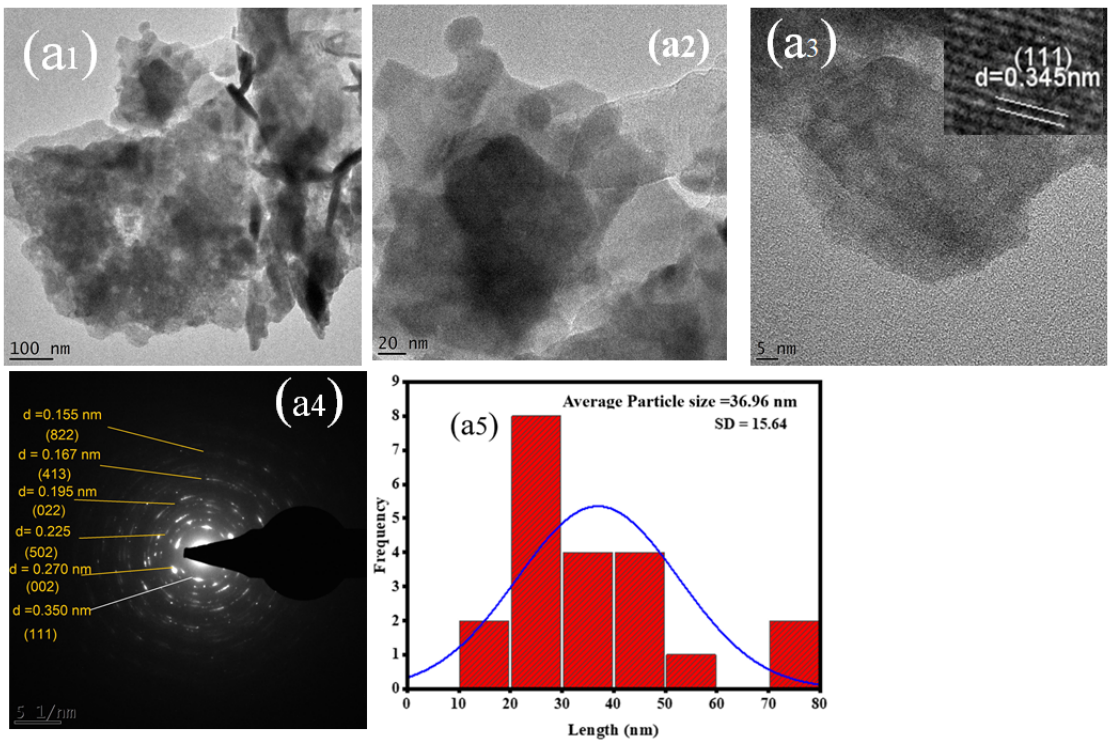

Figure 4.16: (a1, a2) TEM images, (a3,) HR-TEM image, (a4) SAED image, (a5) Particle size distribution of BNO/PANI-10% nanocomposite.

4.18 (c5), generated using Image J software, reveal that the majority of nanoparticles fall within the size ranges of 30-40 nm for BNO, 20-30 nm for BNO/PANI-10%, 40-60 nm for BNO/PANI-20%, and 30-40 nm for BNO/PANI-30% nanocomposites. The normal distribution fit to these curves yielded average particle sizes of 31.54, 36.96, 59.69, and 35.73 nm, with corresponding standard deviations of 9.78, 15.64, 24.83, and 12.92, respectively. These variations in particle size indicate that the incorporation of PANI influences the growth and aggregation of the particles within the composites. Specifically, the larger particle size observed in the BNO/PANI-20% sample suggests more significant aggregation or coalescence, while the relatively smaller sizes in BNO/PANI-10% and BNO/PANI-30% imply more controlled particle growth, likely due to different interactions between BNO and different amounts of PANI.

4.5.3 TEM Analysis of SnO_2/BNO Nanocomposite

In the SnO_2/BNO nanocomposite, the continuous lattice fringes were measured to have interplanar d-spacing values at 3.40, 2.73, and 2.64 Å, corresponding to the (110), (101), and (002) planes, respectively, as shown in Fig. 4.19(b). Additionally, SAED patterns shown four distinct bright rings were observed, corresponding to interplanar spacing (d) values of 0.322, 0.262, 0.217, and 0.168 nm, which are indexed to the (110), (101), (002), and (413) planes, respec-

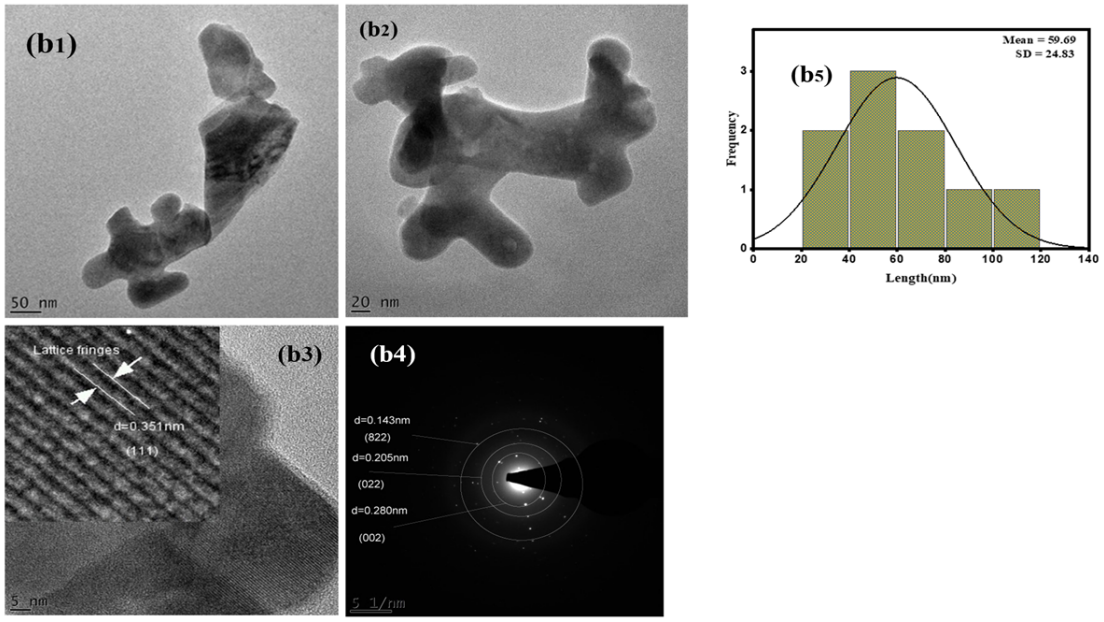

Figure 4.17: (b1, b2) TEM images, (b3) HR-TEM images, (b4) SAED images, and (b5) Particle size distribution of BNO/PANI-20% nanocomposite.

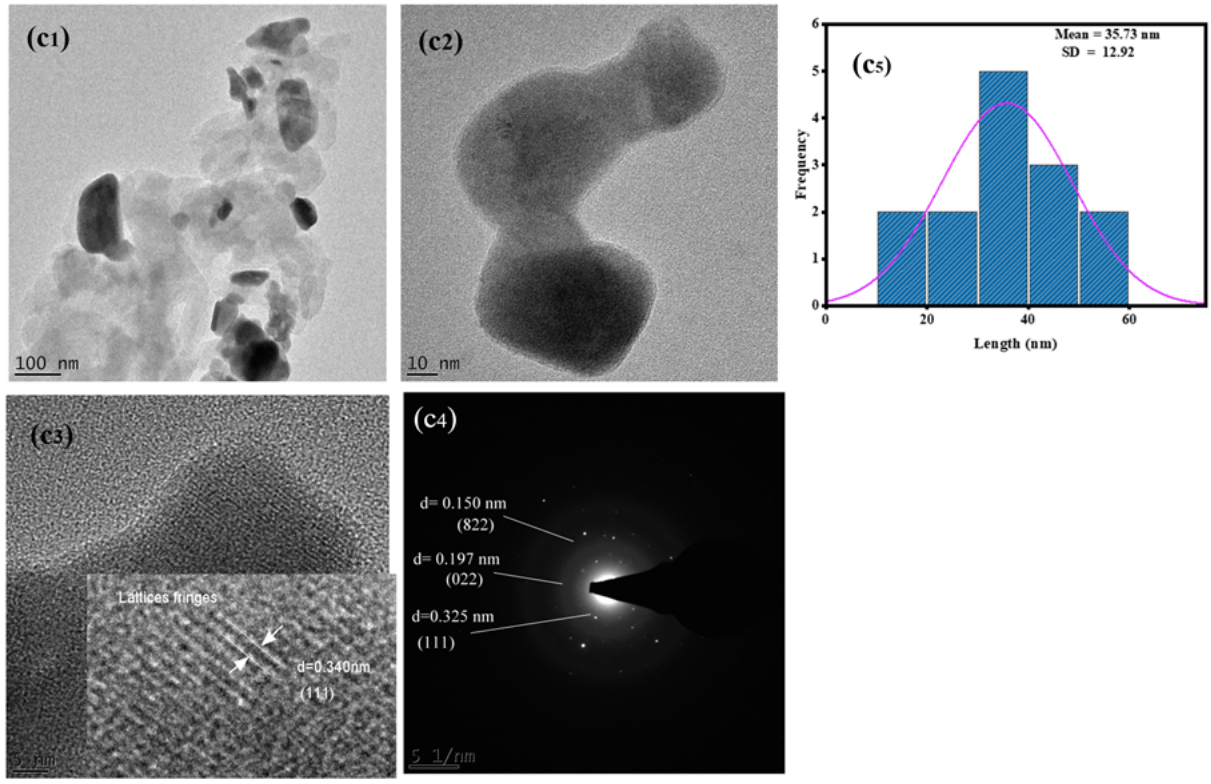

Figure 4.18: (c1, c2) TEM images, (c3) HR-TEM images, (c4) SAED images, and (c5) Particle size distribution of BNO/PANI-30% nanocomposite.

tively, as shown in Fig. 4.19 (c). These features confirm the coexistence of both SnO_2 and BNO phases within the nanocomposite. The slight shifts in the observed d-spacing values in the composite, relative to those of the pure SnO_2 and BNO, suggest possible interfacial interactions between the two components without significant distortion of their crystal structures. Furthermore, particle size distribution analysis, as shown in Fig. 4.19 (d), indicates that the SnO_2/BNO nanocomposite particles predominantly fall within the range of 14-16 nm. A normal distribution fit yielded a mean particle size of 16.23 nm with a standard deviation of 4.59.

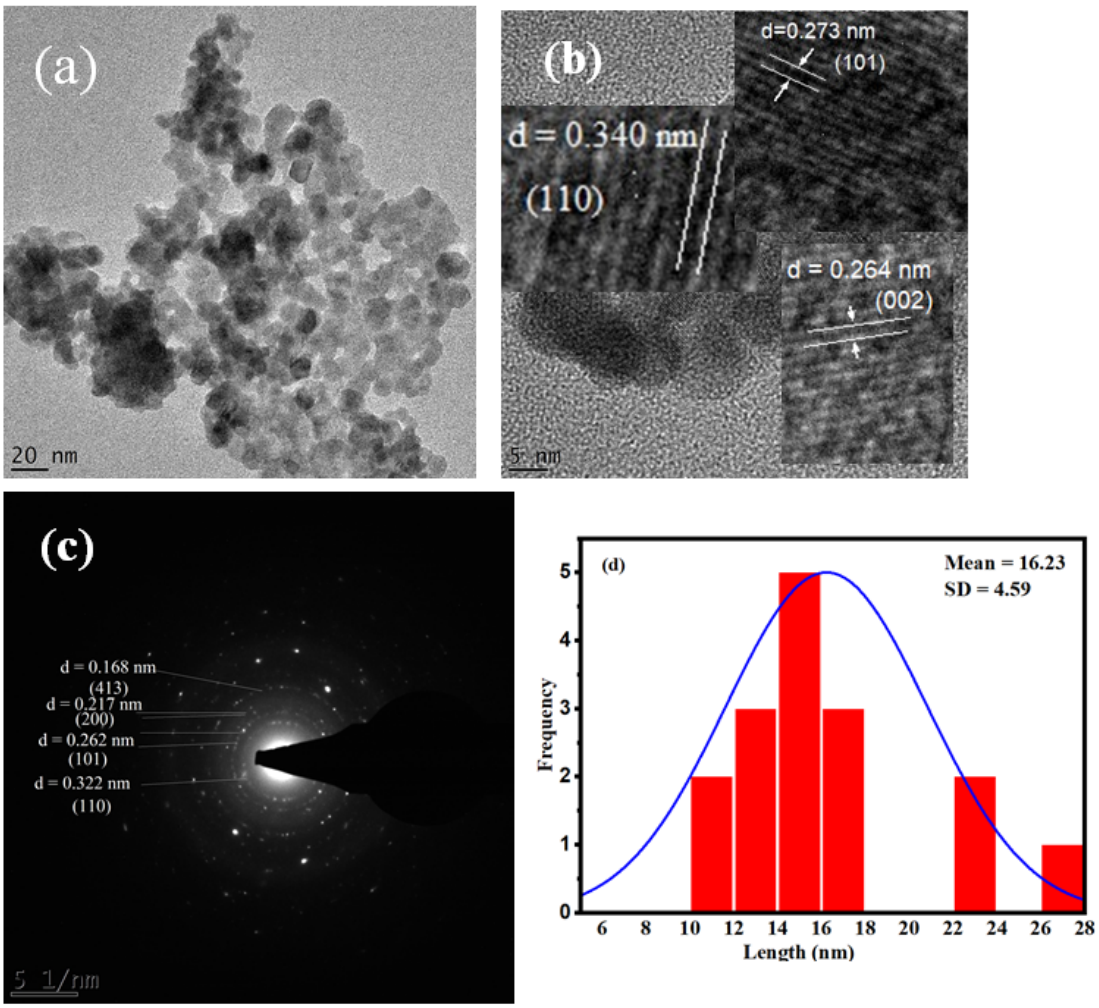

Figure 4.19: TEM image of (a) SnO_2/BNO, (b) HRTEM image of SnO_2/BNO, (c) SAED image of SnO_2/BNO, and (d) Average particle size distribution of SnO_2/BNO of the nanocomposite

4.5.4 TEM Analysis of SnO_2/BNO/PANI Ternary Nanocomposite

As observed in Fig. 4.20(a-d), the SnO_2/BNO/PANI ternary nanocomposite was characterized using TEM and HR-TEM to examine its microstructure, crystalline nature, and atomic orientation. As shown in Fig. 4.20(a), the ternary nanocomposite retains the morphology of each of the

individual pristine components, indicating successful integration. The (002) and (110) planes of BNO and SnO_2 were recognized as separate lattice fringes with d-spacings of 0.269 and 0.343 nm in the HR-TEM image of the ternary composite, respectively, as shown in Fig. 4.20 (b). Lattice strain brought on by the addition of BNO and PANI is probably the cause of the minor differences in these values when compared to those of pure SnO_2. However, the retention of primary SnO_2 planes suggests that the SnO_2 crystalline structure is still mostly present in the composite. Five different diffraction rings are also seen in the selected area electron diffraction (SAED) pattern (Fig. 4.20(c)), which correspond to interplanar spacings of 0.355, 0.274, 0.229, 0.176, and 0.144 nm. The (111), (002), (502), (211), and (310) atomic planes can all be associated with these rings, respectively. The coexistence of both phases is confirmed by the presence of the BNO of (111), (002), and (502) planes as well as the SnO_2 (211) and (310) planes. This image illustrates the development of a ternary nanocomposite that is structurally coherent and well-integrated.

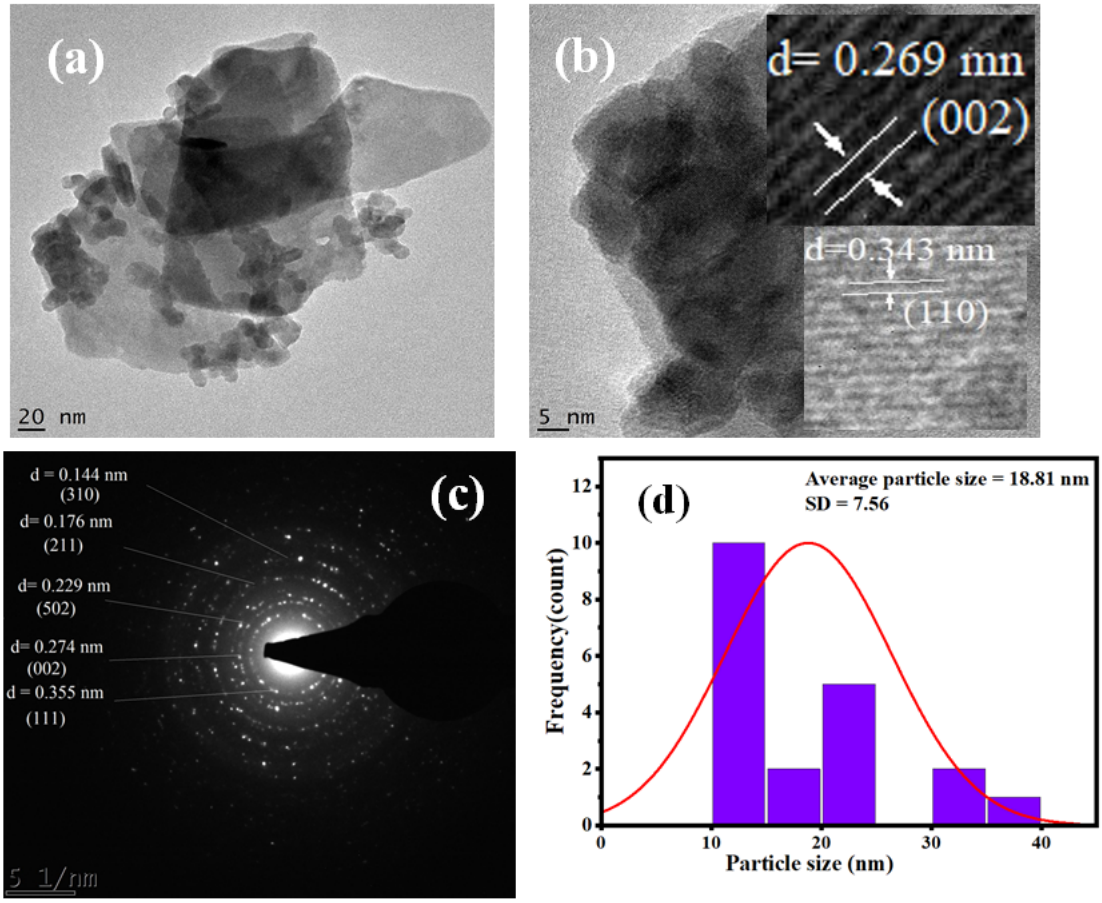

Figure 4.20: TEM image of (a) SnO_2/BNO/PANI, (b) HR-TEM image of SnO_2/BNO/PANI, (c) SAED image of SnO_2/BNO/PANI, and (d) Average particle size distribution of SnO_2/BNO/PANI of the nanocomposite

According to TEM investigation, the average particle size of the SnO_2/BNO/PANI ternary nanocomposite is 18.81 nm (see Fig. 4.20 (d). This value falls between the SnO_2 and BNO particle sizes of the constituent parts. The ternary composite's intermediate size indicates that the various phases were successfully integrated throughout its synthesis, without particle expansion or agglomeration. The PANI matrix may have stabilized the particle growth throughout synthesis, as evidenced by the decrease in particle size when compared to BNO and the minor rise when compared to SnO_2. Because it provides a balance between surface area and structural integrity, this moderate particle size is beneficial for different applications.

4.6 Optical Properties

4.6.1 Optical Properties of SnO_2, and SnO_2/PANI-X Nanocomposites

The UV–Vis absorbance spectra of pure SnO_2 and SnO_2/PANI nanocomposites with varying PANI contents (10%, 20%, and 30%) reveal a strong absorption in the UV region below 350 nm, which gradually decreases toward the visible range (400–800 nm), as shown in Fig. 4.21(a). This characteristic UV absorption corresponds to intrinsic electronic transitions from the valence to the conduction band in SnO_2, indicating its wide band gap semiconducting nature. Upon incorporating PANI, the overall absorbance intensity notably increases, particularly in the visible region, with the SnO_2/PANI–30% composite exhibiting the highest absorbance.

The Eg can be determined by extending the linear section of the curves to the point of zero absorption ($\alpha = 0$) using Eq. 2.22, as shown in Fig. 4.21(b) (Sangiorgi et al., 2017). The band gap measurements for SnO_2 and its composites with PANI at different weight percentages (10%, 20%, and 30%) were calculated using Tauc's Eq. (2.22) for indirect allowed transitions. The SnO_2 nanoparticles demonstrated an indirect band gap of 3.91eV, confirming their nature as wide band gap semiconductors, which is in close agreement with the previously reported band gap energy of 3.7 eV (Uddin et al., 2021). The indirect band gap fitting is more suitable because the absorption spectrum of SnO_2 shows characteristics typical of an indirect semiconductor, such as a gradual increase near the band edge. This fitting provides a more accurate and smoother curve, better matching the known electronic structure of SnO_2 and offering a more precise representation of its optical properties. However, when the conducting polymer (PANI) was added to the SnO_2 nanoparticles, there was a notable reduction in the band gap values, as shown in Fig. 4.21 (b). The enhanced absorbance with increasing PANI concentration can be attributed to π–π^* transitions in the PANI backbone and to strong interfacial interactions between the SnO_2 nanoparticles and the polymer matrix. This interaction facilitates better charge transfer and light harvesting, resulting in a slight red shift and reduced band gap energy.

The SnO_2/PANI-10% composite shows a band gap (E_g) of 3.8 eV, whereas the SnO_2/PANI-20% and SnO_2/PANI-30% composites exhibited even lower band gaps of 3.62 eV and 3.23 eV, respectively. The gradual decrease in the band gap energy of a semiconductor nanocomposite indicates enhanced electrical conductivity, beneficial for energy storage applications like supercapacitors.

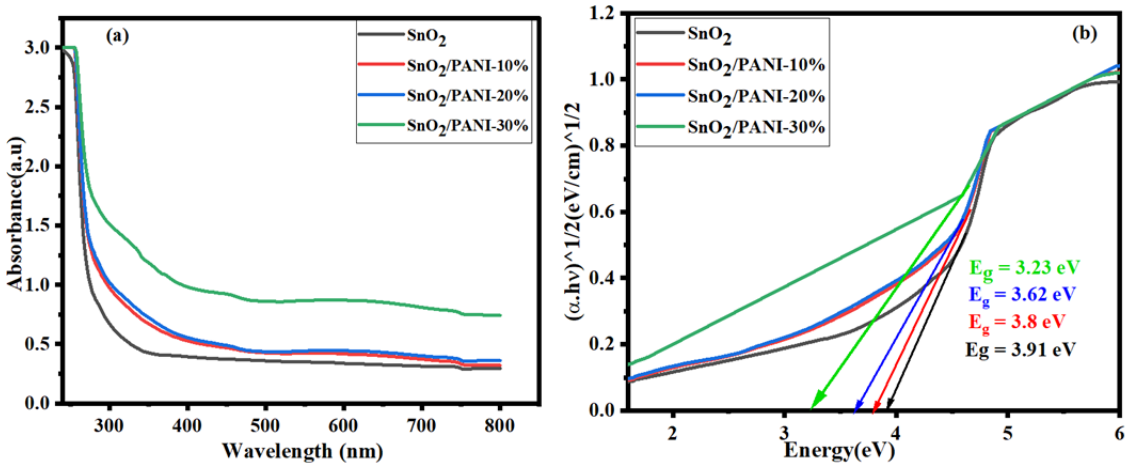

Figure 4.21: (a) absorbance spectra of SnO_2, and SnO_2/PANI-X, and (b)Tauc's plot for determining the optical band gap (Eg) for SnO_2, SnO_2/PANI-X with indirect transition.

4.6.2 Optical Properties of BNO/PANI Nanocomposites

The UV–Vis spectra of pure $Bi_5Nb_3O_{15}$ (BNO) and BNO/PANI nanocomposites with different PANI loadings (10%, 20%, and 30%) show a strong absorption edge around 300 nm, which corresponds to the intrinsic band-to-band transition of BNO.

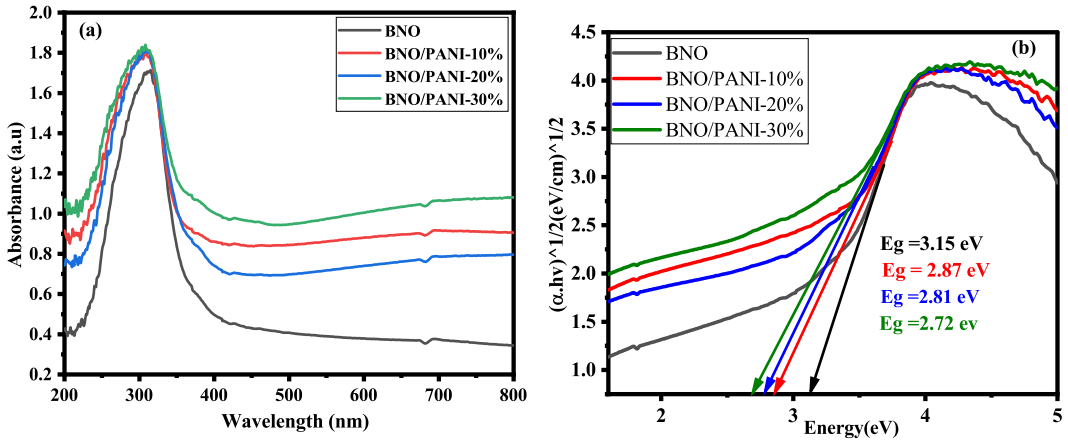

Figure 4.22: (a) absorbance spectra of BNO , and BNO/PANI-X nanocomposites, (b) Tauc plot for determining the optical band gap (E_g) for BNO, BNO/PANI-X with indirect transition.

The pure BNO sample exhibits strong absorption in the UV region, confirming its wide band gap semiconducting nature. Upon the incorporation of PANI, the overall absorbance increases markedly, particularly in the visible region (400–800 nm), with the BNO/PANI–30% composite displaying the highest absorption intensity, as shown in Fig. 4.22(a). This enhancement can be attributed to the π–π^* transitions within the conjugated structure of PANI and to the strong interfacial interaction between the BNO nanoparticles and the PANI matrix.

The band gap values for BNO and its composites with PANI at varying weight percentages (10%, 20%, and 30%) were determined using Tauc's Eq. 2.22 for indirect allowed transition. The synthesized BNO nanoparticle displayed a band gap of 3.15 eV, confirming its intrinsic nature as a wide band gap semiconductor, and this is a close agreement with earlier reported band gap energy value of 3.25 eV (Gurunathan & Maruthamuthu, 1998), However, upon incorporating conducting polymer (PANI) into the BNO matrix, the band gap values decreased significantly as illustrated in Fig. 4.22(b). The BNO/PANI-10% composite showed a band gap (Eg) of 2.87 eV, while the BNO/PANI-20% and BNO/PANI-30% composites exhibited even lower band gaps of 2.81 eV and 2.72 eV, respectively. This progressive reduction in the band gap with increasing PANI content suggests a strong interaction between BNO and PANI, enhancing the material's light absorption capabilities. Additionally, the reduction in band gap of a semiconductor nanocomposite implies improved electrical conductivity, which is advantageous for energy storage applications such as supercapacitors. The storage principle is based on charge separation. So the composite that has a low or medium energy band with a gap shows a good supercapacitance performance (Momma et al., 1996; Obodo et al., 2020).

4.6.3 Optical Properties of SnO_2/BNO and SnO_2 /BNO/PANI Nanocomposites

The UV-Vis spectra show that the SnO_2/BNO and SnO_2/BNO/PANI nanocomposites have significant absorption peaks at about 315 and 300 nm, respectively, as shown in Fig. 4.23 (a). This means that they absorb ultraviolet light. These absorption peaks are caused by electronic transitions from the valence band to the conduction band, which are typical of semiconductor materials, and are represented by these absorption peaks. The optical band gaps of SnO_2/BNO and SnO_2/BNO/PANI nanocomposites were studied using UV-Vis spectroscopy, as shown in Fig. 4.23 (b). The optical band gaps (E_g) were then determined using Tauc's approach (Eq.(2.22)), which consists of plotting the converted absorbance data against photon energy and extrapolating the linear component of the plot. The band gap values for synthesized nanocomposites were 3.2 eV for SnO_2/BNO and 2.65 eV for SnO_2/BNO/PANI, as shown in the Fig. 4.23 (b). In comparison, the band gap of pristine SnO_2 was found to be 3.91 eV, whereas that of BNO was 3.15 eV. SnO_2/BNO has an intermediate band gap, indicating the production of a nanocomposite that improves charge transport between the two.

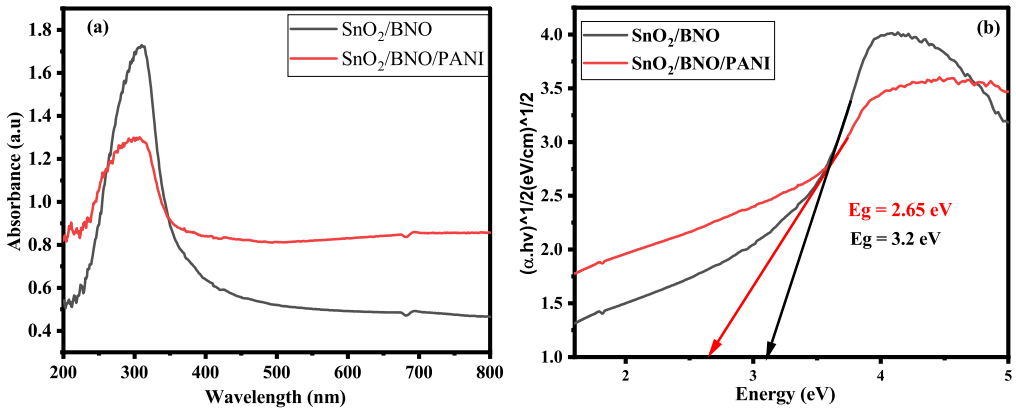

Figure 4.23: (a) Absorption and (b) Tauc's plot for determining the optical band gap (E_g) for SnO_2/BNO, and SnO_2/BNO/PANI nanocomposites .

The ternary SnO_2/BNO/PANI nanocomposite has a reduced band gap, indicating improved electrical interaction with the conductive polymer PANI. When compared to the pristine SnO_2, and BNO nanoparticles, as well as, the binary SnO_2/BNO, SnO_2/PANI-X, and BNO/PANI-X nanocomposites , the absorption peak of the ternary nanocomposite shows a red shift, which indicates that the addition of PANI has improved charge delocalization and increased electronic interaction. This change decrease band gap energy as compared to the pristine and binary nanoparticles, suggests that PANI expands the absorption towards the visible region, improving light-harvesting capabilities in addition to altering the optical absorption edge.

4.7 Electrochemical Ananlysis

4.7.1 Cyclic voltammetry (CV) Studies of SnO_2, SnO_2/PANI-X Nanocomposites

Cyclic voltammetry (CV) is regarded as an excellent method for evaluating the capacitive characteristics of any material. Figures 4.24 (a-d) display the CV curves for pristine SnO_2 and SnO_2/PANI-X composites at scan rates of 5, 10, 20, 50, and 100 mVs^{-1}. The CV testing was performed across a potential range of 0 to 0.9 V in a 1 M H_2SO_4 aqueous electrolyte solution. The CV curves exhibit a quasi-rectangular shape within the specified potential range, as illustrated in Fig. 4.24. Thus, the quasi-rectangular CV curve suggests that the electrode material has desirable properties for capacitive applications, such as efficient charge storage, stability, and reversibility within the tested voltage range. In acidic electrolytes (1M H_2SO_4), SnO_2 exhibits pseudocapacitive behavior mainly through a reversible redox process involving proton insertion. During the electrochemical cycling, protons from the electrolyte interact with the surface or near-surface region of SnO_2, accompanied by electron transfer from the external circuit, as shown in Eq. 4.1. This process leads to the formation of a hydrogenated oxide phase without

significant structural change, as represented by the following redox reaction:

$$SnO_2 + nH^+ + ne^- \rightleftharpoons SnOOH, \tag{4.1}$$

Here, n denotes the number of protons and electrons involved in the reversible process, indicating the degree of proton intercalation.

SnO_2/PANI-X nanocomposites show a larger integral area of the CV curve when compared with SnO_2, indicating the increased specific capacitance, as shown in Table 4.3. As the weight percentage of PANI on the SnO_2 surface rises, the integral area of the CV curve also increases, along with a higher background current. Therefore, it is reasonable to conclude that the capacitive contribution of SnO_2/PANI is enhanced due to the substantial accessible active area of PANI supported on SnO_2.

The cyclic voltammetry (CV) analysis of SnO_2/PAN nanocomposites with varying PANI content (10%, 20%, and 30% by weight) reveals a clear trend of enhanced the specific capacitance with increasing PANI concentration at the first two lower scan rates, as shown in Table 4.3. The specific capacitance (C_{SP}) of the electrode material were obtained by using Eq. (2.2).

As the percentage of PANI in the SnO_2 nanoparticles increases, the CV area under the curves becomes significantly larger, indicating a substantial improvement in the charge storage capability of the composites. This is corroborated by the observed increase in specific capacitance values, demonstrating that higher PANI content enhances the electrochemical activity of the nanocomposites, as shown in Table 4.3. As shown in Fig. 4.24 (e, f), there is minimal difference in the performance between the 20% and 30% addition of PANI. Therefore, increasing the PANI content beyond 30% may not have resulted in higher specific capacitance. As a result, additional amounts exceeding 30% PANI on SnO_2 were not explored. The incorporation of PANI, a conductive polymer with excellent redox properties, synergistically increases the pseudocapacitive behavior of SnO_2, resulting in improved overall capacitance.

Table 4.3: Specific capacitance of the synthesized SnO_2, SnO_2/PANI-10%, SnO_2/PANI-20%, and SnO_2/PANI-30% nanocomposite electrodes measured at scan rates of 5–100 mV/s in the potential range of 0–0.9 V.

Scan rate (mV/s)	Specific capacitance (F/g) of the electrode materials			
	SnO_2	SnO_2/PANI-10%	SnO_2/PANI-20%	SnO_2/PANI-30%
5	11.8	118	222	242
10	9.5	70.6	147	144
20	8.3	47.0	93.9	87.8
50	7.1	28.1	49.2	45.0
100	6.1	18.4	28.5	26.8

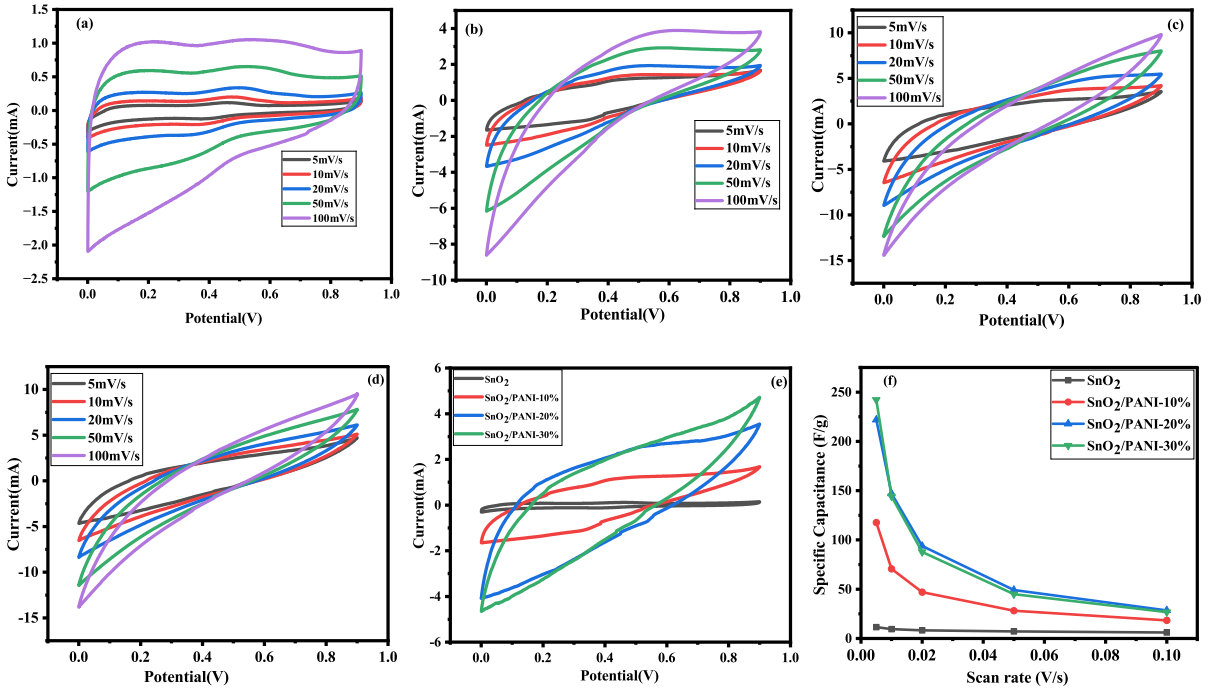

Figure 4.24: A CV cures of a) SnO_2, b) SnO_2/PANI-10%, c) SnO_2/PANI-20%, d) SnO_2/PANI-30%, e) SnO_2, SnO_2/PANI-X at 5 mVs^{-1} scan rate f) Specific capacitance for scanning rates of SnO_2, SnO_2/PANI-X in 1M H_2SO_4 aqueous electrolyte.

4.7.2 Cyclic Voltammetry (CV) Studies of BNO, and BNO/PANI-X Nanocomposites

The capacitance behavior of BNO and BNO/PANI-X nanocomposites as electrode materials was studied using 1 M H_2SO_4 aqueous electrolyte solution within a potential range of 0 to 0.9 V. The CV curves of the pristine BNO and BNO/PANI-X are performed at scan rates of 5, 10, 20, 50, and 100 mVs^{-1} in the indicated voltage range, as shown in Fig. 4.25 (a-d). The CV curves of BNO are quasi-rectangular shape within the measured potential range. Oxidation and

reduction peaks are observed at 0.49 V and 0.4 V, respectively, in the CV of BNO nanoparticles at a scan rate of 5 mVs^{-1}. The oxidation and reduction peaks of BNO are shifted to the positive and negative potential, respectively, as the scanning rate increases, as illustrated in Fig. 4.25 (a). The shape of the CV and existence of oxidation and reduction peaks in BNO indicated the occurrence of a faradaic reaction, and it shows surface pseudocapacitive behavior, while that of the composites shows more of intercalation pseudocapacitance (Chodankar et al., 2020). The charge storage mechanism in H_2SO_4 electrolyte is the adsorption of H^+ ions on the composite's surface and the charge/discharge possibly achieved through intercalation/ de-intercalation of H^+ as shown in Eq. 4.2 (Gu et al., 2017; Rafique et al., 2020).

$$Bi_5Nb_3O_{15} + nH^+ + ne^- \leftrightarrow H_nBi_5Nb_3O_{15} \tag{4.2}$$

The intercalation pseudocapacitance involves the reversible insertion of protons (H^+) into the BNO structure, combined with the redox activity of PANI. From Fig. 4.25 (b-e), it can be noted that the current response of the BNO/PANI-X is significantly larger than BNO, which indicates that BNO/PANI-X has better electrochemical kinetics. The calculated specific capacitances for BNO, BNO/PANI-10%, BNO/PANI-20%, and BNO/PANI-30% are 10.4, 129, 157, and 216 Fg^{-1}, respectively, at a scan rate of 5 mVs^{-1} as shown in Table 4.4. Among all the samples of BNO/PANI-X, BNO/PANI-30% showed the highest specific capacitance at a scan rate of 5 mVs^{-1}. As the particle size decreases, the specific surface area increases, resulting in improved charge transport at the interface between the electrode and the electrolyte (Isacfranklin et al., 2020). The cyclic voltammogram (CV) of BNO/PANI-10% and BNO/PANI-30% nanocomposites show distinct reduction and oxidation peaks compared to BNO and BNO/PANI-20%. This indicates an optimal synergy between BNO and PANI at the 10%, 30% PANI loading, enhancing the visibility of redox peaks as shown in Fig. 4.25 (e). However, the capacitance value of BNO/PANI-10% is less than that of BNO/PANI-20%, although it is greater than that of pristine BNO. This suggests that while the 10% PANI composition improves the electrochemical activity and redox reactions, and higher PANI loadings (20% and 30%) further enhance the overall capacitance due to increased electronic conductivity and more active sites provided by PANI (M. S. Kumar et al., 2020). Even if the redox peaks decrease, the increased surface area can contribute significantly to the overall capacitance.

The CV results indicate that the specific capacitance of the BNO/PANI-X nanocomposites improved compared to the pristine BNO, with the specific capacitance increasing as the weight percentage of PANI increases. However, at higher scan rates, like 50 and 100 mVs^{-1}, the specific capacitance of the BNO/PANI-30% composite is below BNO/PANI-20% as shown in Fig. 4.25 (f). In the BNO/PANI-30% composite, the increased PANI content created a more complex

structure, making ion diffusion more challenging at higher scan rates and reducing the specific capacitance value as compared to BNO/PANI-20%. Higher scan rates can lead to diffusion limitations where ions cannot penetrate the electrode material effectively.

Table 4.4: Specific capacitance of the synthesized BNO, BNO/PANI-10%, BNO/PANI-20%, and BNO/PANI-30% nanocomposite electrodes measured at scan rates of 5–100 mV/s in the potential range of 0–0.9 V.

Scan rate (mV/s)	Specific capacitance ($F \cdot g^{-1}$) of the electrode materials			
	BNO	BNO/PANI-10%	BNO/PANI-20%	BNO/PANI-30%
5	10.4	129	157	216
10	7.34	98.6	124	154
20	5.48	74.4	99.4	109
50	3.90	48.0	73.3	65.2
100	3.15	31.9	56.5	41.7

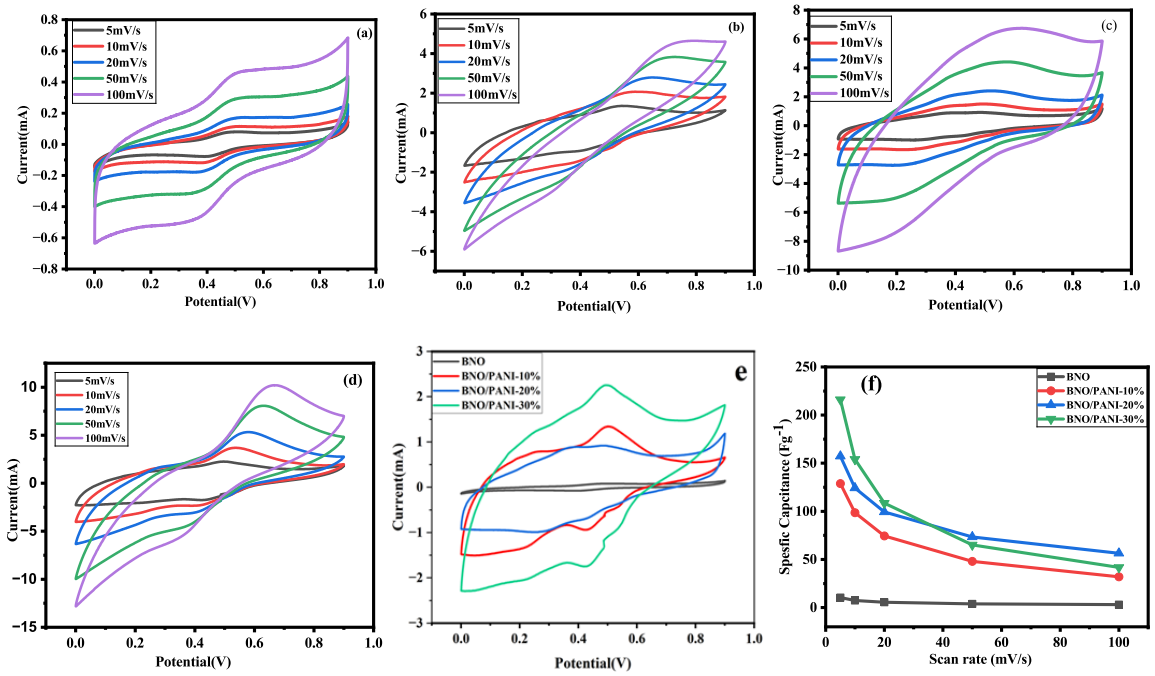

Figure 4.25: Cyclic voltammetry curves of a) BNO, b) BNO/PANI-10%, c) BNO/PANI-20%, d) BNO/PANI-30%, and e) BNO, BNO/PANI-X at 5 mV/s scan rate, and f) specific capacitances of BNO and BNO/PANI-X nanocomposites at various scan rates by cyclic voltammetry analysis.

At a high scan rate, the CV curve area is larger compared to that at a low scan rate, but this does not enhance the electrode material's charge storage capacity. At a low scan rate, the active materials have sufficient time to engage in redox reactions with the electrolyte, promoting charge

storage. Concurrently, a higher scan rate increases the current of the electrode material, causing the oxidation peak to shift towards the positive potential and the reduction peak towards the negative potential (Fig. 4.25 (b-d)). This result is due to the polarization reaction (Elmanfaloty et al., 2024).

4.7.3 Cyclic Voltammetry (CV) Analysis of SnO_2/BNO, and SnO_2/BNO/PANI Nanocomposites

Figure 4.26 (a,b) shows the CV curves for SnO_2/BNO and SnO_2/BNO/PANI composites at scan rates of 5, 10, 20, 50, and 100 mVs^{-1}. The CV test was carried out in a 1 M H_2SO_4 aqueous electrolyte solution at potentials ranging from 0 to 0.9 V. The CV curves have a quasi-rectangular shape within the prescribed potential range, as shown in Fig. 4.26. Thus, the quasi-rectangular CV curve indicates that the electrode material possesses desirable qualities for capacitive applications, such as effective charge storage, stability, and reversibility within the voltage range examined. The specific capacitance (C_{SP}) values were calculated from the area enclosed by the CV curves using Eq. 2.2. The SnO_2/BNO nanocomposite delivers specific capacitances of 15.7, 11.5, 9.04, 6.95, and 5.82 F g^{-1} at scan rates of 5, 10, 20, 50, and 100 mV s^{-1}, respectively. Notably, the ternary SnO_2/BNO/PANI nanocomposite exhibits significantly higher specific capacitances of 424, 327, 241, 146, and 92.7 F g^{-1} at the corresponding scan rates.

The CV curves of SnO_2/BNO and SnO_2/BNO/PANI nanocomposites exhibit significantly larger integral areas compared to pristine SnO_2 and BNO, indicating enhanced specific capacitance as shown in Fig. 4.26 (a,b). This increase in the CV area suggests improved charge storage capability resulting from the synergistic effects between the composite components. Notably, the SnO_2/PANI and BNO/PANI composites demonstrate a greater integral area and higher background current than SnO_2/BNO, implying superior capacitive performance. This can be attributed to the conductive nature of PANI, which provides a larger electrochemically active surface area when supported on SnO_2, facilitating more efficient charge transfer and storage. Furthermore, the ternary SnO_2/BNO/PANI composite exhibits an even higher background current than the binary SnO_2/BNO, BNO/PANI, and SnO_2/PANI composites, suggesting further enhancement in capacitive behavior due to the combined contributions of BNO and PANI on SnO_2 nanoparticles.

As shown in Fig. 4.26 (c), the CV results confirm that the specific capacitance of the ternary nanocomposite is significantly enhanced compared to pristine SnO_2, BNO, and the binary composites. The calculated specific capacitances confirm this trend, with values of 15.7 and 424 F.g^{-1} for SnO_2/BNO and SnO_2/BNO/PANI, respectively, at 5 mVs^{-1}. The substantial increase in capacitance for the PANI-containing composites underscores the critical role of conductive

polymer integration in improving electrochemical performance.

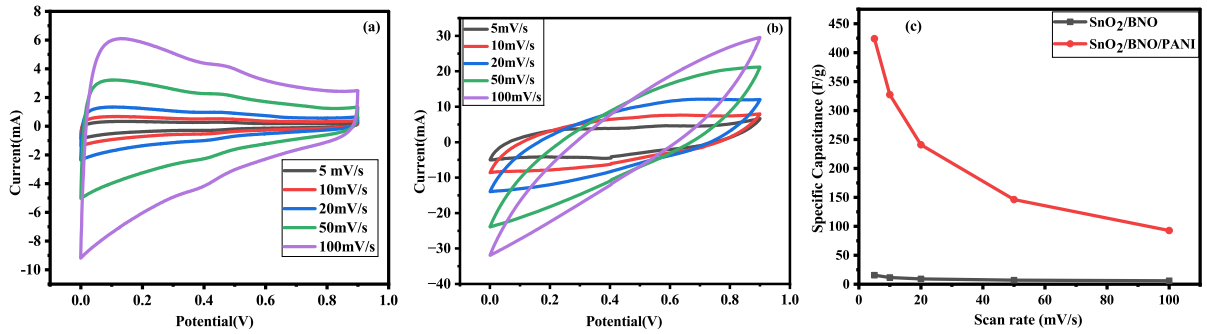

Figure 4.26: A CV curves of a) SnO_2/BNO, b) SnO_2/BNO/PANI; c) specific capacitances of SnO_2/ BNO and SnO_2/BNO/PANI nanocomposites at various scan rates.

4.7.4 Charge Storage Mechanism

The charge storage mechanism of the pristine nanoparticles, binary, and ternary nanocomposites were also examined by carrying out a detailed analysis of their CV curves. The power-law relationship has been used to identify the dominant charge storage process, where peak current (I) is varied with scan rate (ν), according to Eqs. (2.3) and (2.4). The charge–storage parameter b was determined from the slope of the plot of $\log(I)$ versus $\log(\nu)$. A value of $b \approx 1$ indicates a surface–controlled process, whereas $b \approx 0.5$ corresponds to diffusion–limited behavior. Thus, $\log \nu$ was plotted against $\log I$ at a selected potential to obtain the value of b.

The pristine oxides SnO_2 and BNO exhibit primarily capacitive behavior as shown in Fig. 4.27 (a, b), respectively. BNO shows a stronger capacitive nature than SnO_2, which is attributed to its layered perovskite structure that provides abundant surface active sites. SnO_2 also demonstrates significant capacitive contribution, although with some minor influence of diffusion processes due to limited ion insertion into its lattice. When combined with PANI, both SnO_2 and BNO generally shift towards diffusion-controlled charge storage as shown in Fig. 4.28 (a-f).

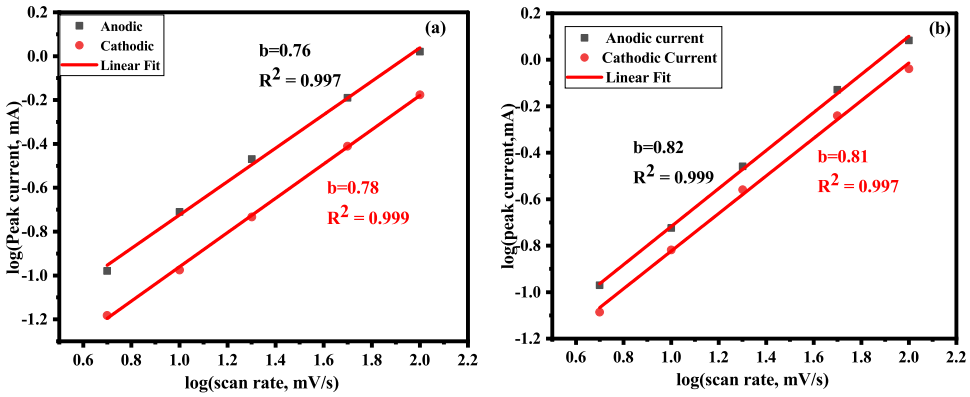

Figure 4.27: Plots of power's law for a) SnO_2, and b) BNO at fixed potential of 0.5V.

At low and moderate PANI contents, the polymer tends to block oxide surfaces and introduce resistive interfaces, leading to slow charge transfer and dominant bulk ion transport. However, in BNO/PANI-20%, the charge storage becomes more balanced, with improved capacitive contributions as shown in Fig. 4.28(e). This indicates that optimized PANI incorporation enhances conductivity and surface redox activity.

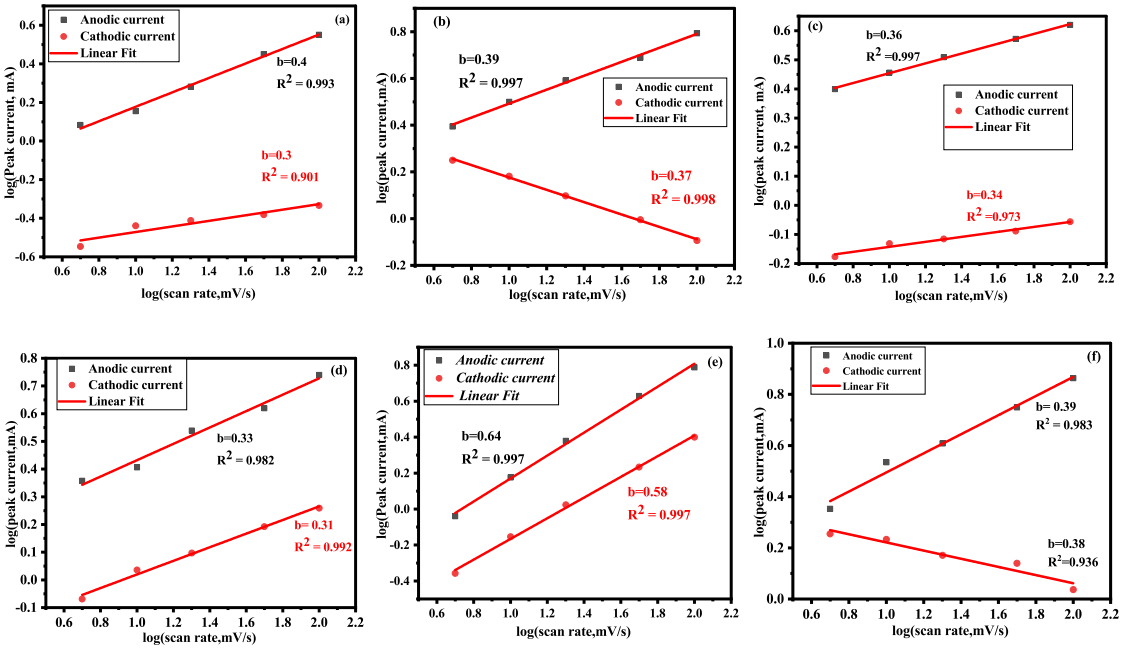

Figure 4.28: Plots of power law fitting for (a) SnO_2/PANI-10%, (b) SnO_2/PANI-20%, (c) SnO_2/PANI-30%, (d) BNO/PANI-10%, (e) BNO/PANI-20%, and (f) BNO/PANI-30% nanocomposites at a fixed potential of 0.5 V.

The binary oxide (SnO_2/BNO) composite demonstrates nearly ideal capacitive behavior as shown

in Fig. 4.29 (a). The strong interfacial synergy between SnO_2 and BNO provides a large number of electroactive sites, improves electronic conductivity, and facilitates rapid ion adsorption/desorption. This results in very fast charge storage dominated by surface-controlled processes. The anodic and cathodic b values of 0.51 and 0.42 for the SnO_2/BNO/PANI nanocomposite indicate that the charge storage process is predominantly diffusion-controlled. Since ideal surface-controlled capacitive behavior shows $b \approx 1$, the much lower values observed here demonstrate that ion diffusion into the electrode bulk governs the electrochemical response, as shown in Fig. 4.29 (b). This behavior is characteristic of faradaic pseudocapacitance, where ions must penetrate the PANI matrix and interact with redox-active sites within the composite. The reduced b values therefore confirm that the SnO_2/BNO/PANI system stores charge mainly through ion-diffusion-limited redox reactions, rather than surface adsorption. Additionally, to further understand the energy storage mechanisms, Dunn's method was used to determine the contributions to the capacitance from diffusion-controlled processes and capacitive-controlled processes at any potential, resulting in Eqs.2.5 and 2.6.

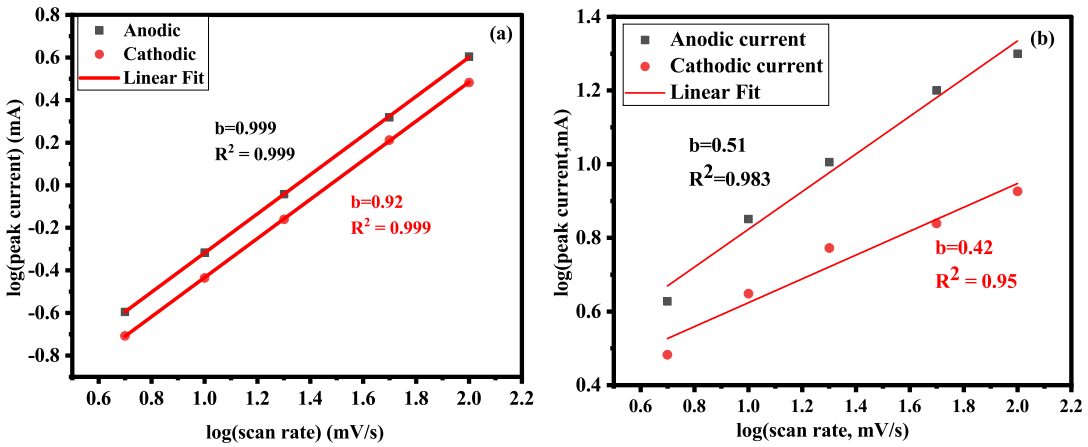

Figure 4.29: Plots of power law fitting for (a) SnO_2/BNO, (b) SnO_2/BNO/PANI nanocomposites at a fixed potential of 0.5 V.

The current response at a fixed potential is considered as the combination of two separate mechanisms, surface capacitive effects, and diffusion-controlled insertion. By plotting the linear fit of $i/\nu^{1/2}$ versus $\nu^{1/2}$, the slope and intercept values of K_1 and K_2 can be obtained, respectively. Thus, the portion of capacitive and diffusion-controlled charge storage contributions was calculated using Eq. 2.5.

Figure 4.30 (a) shows a differentiated CV curve of the SnO_2 at 5 mVs^{-1}, illustrating the capacitive and diffusive contributions to the total capacitance. The results show that 30% of the total capacitance was due to capacitive contributions. Furthermore, Figure 4.30(e) shows the percent-

age contributions at various scan rates. Notably, as the scan rate increased, the contribution of non-diffusion-limited processes increased, reaching 65% at 100 mVs^{-1}.

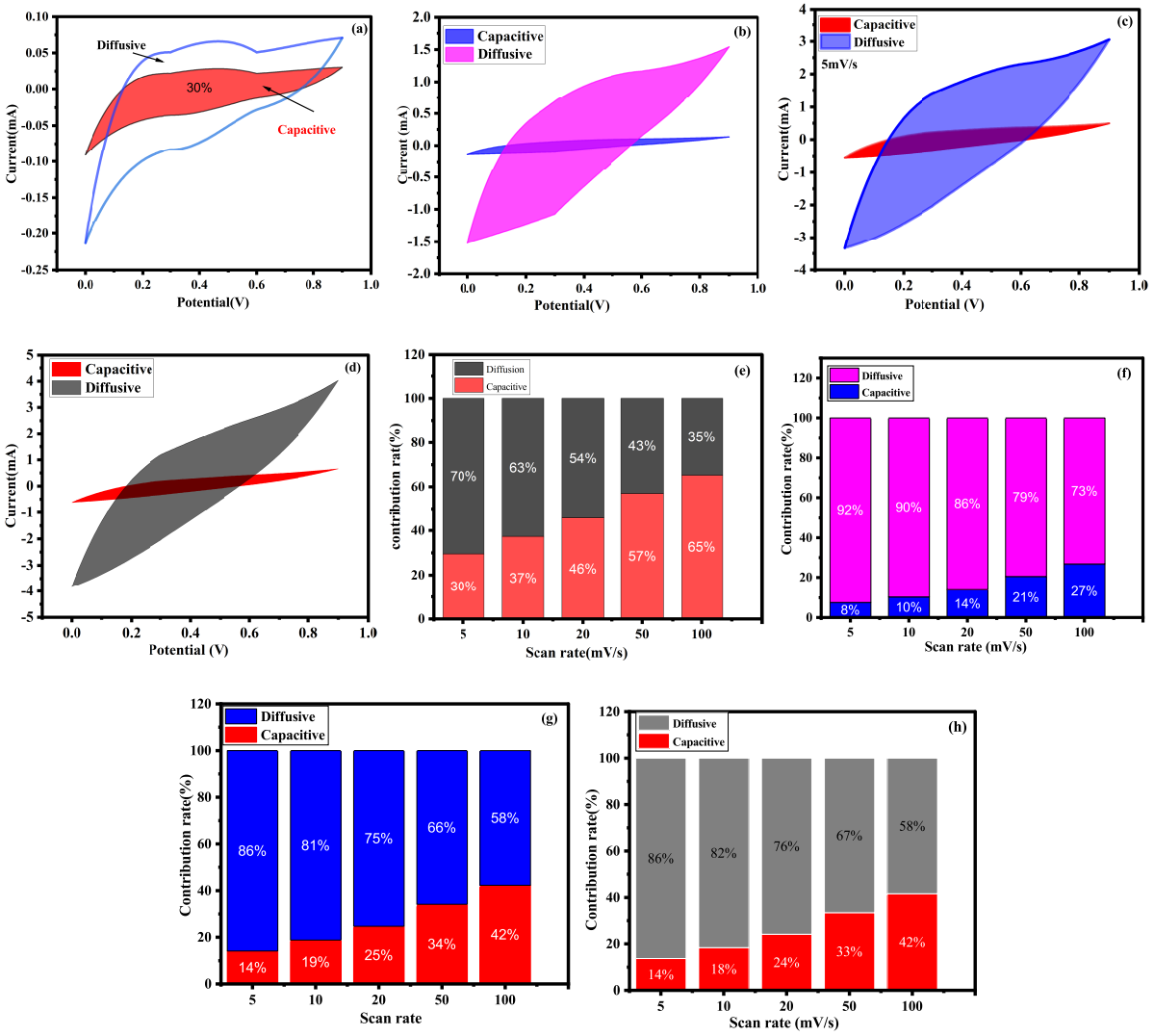

Figure 4.30: (a-d) a capacitive contribution analysis at a scan rate 5 mVs^{-1} for SnO_2, SnO_2/PANI-10%, SnO_2/PANI-20%, SnO_2/PANI-30%, respectively, in various potential (V) and (e-h) Proportional contributions from capacitive and diffusion-controlled capacitances in various scan rates at a fixed potential of 0.5V for SnO_2, SnO_2/PANI-10%, SnO_2/PANI-20%, SnO_2/PANI-30%, respectively.

The observed phenomenon occurs because at low scan rates, electrolyte ions have sufficient time to penetrate deep into the electrode structure, leading to the dominance of Faradaic reactions. However, at higher scan rates, ions lack sufficient time to diffuse into pores. Consequently, charge storage mostly occurs on the electrode surface rather than within the bulk material (Dupont & Donne, 2016). In contrast, for the SnO_2/PANI-10% composite, the capacitive-

controlled contribution accounts for only 8% at 5 mVs^{-1} (see Fig. 4.30(b)), but rises to 27% at 100 mVs^{-1}, suggesting that the incorporation of a small amount of PANI initially limits capacitive activity but improves with increasing scan rate as shown in Fig. 4.30 (f). Similarly, the SnO_2/PANI-20% composite exhibits a capacitive contribution of 14% at 5 mVs^{-1} and 42% at 100 mVs^{-1} as shown in Fig. 4.30 (c, g), while the SnO_2/PANI-30% sample shows a comparable trend, with capacitive contribution values equal to those of the 20% composite as shown in Fig. 4.30 (d,h). Overall, Figure 4.30 (f-h) presents the percentage contributions at various scan rates. These results confirm that higher scan rates favor capacitive-controlled charge storage, and moderate PANI incorporation enhances the surface redox kinetics of SnO_2-based electrodes.

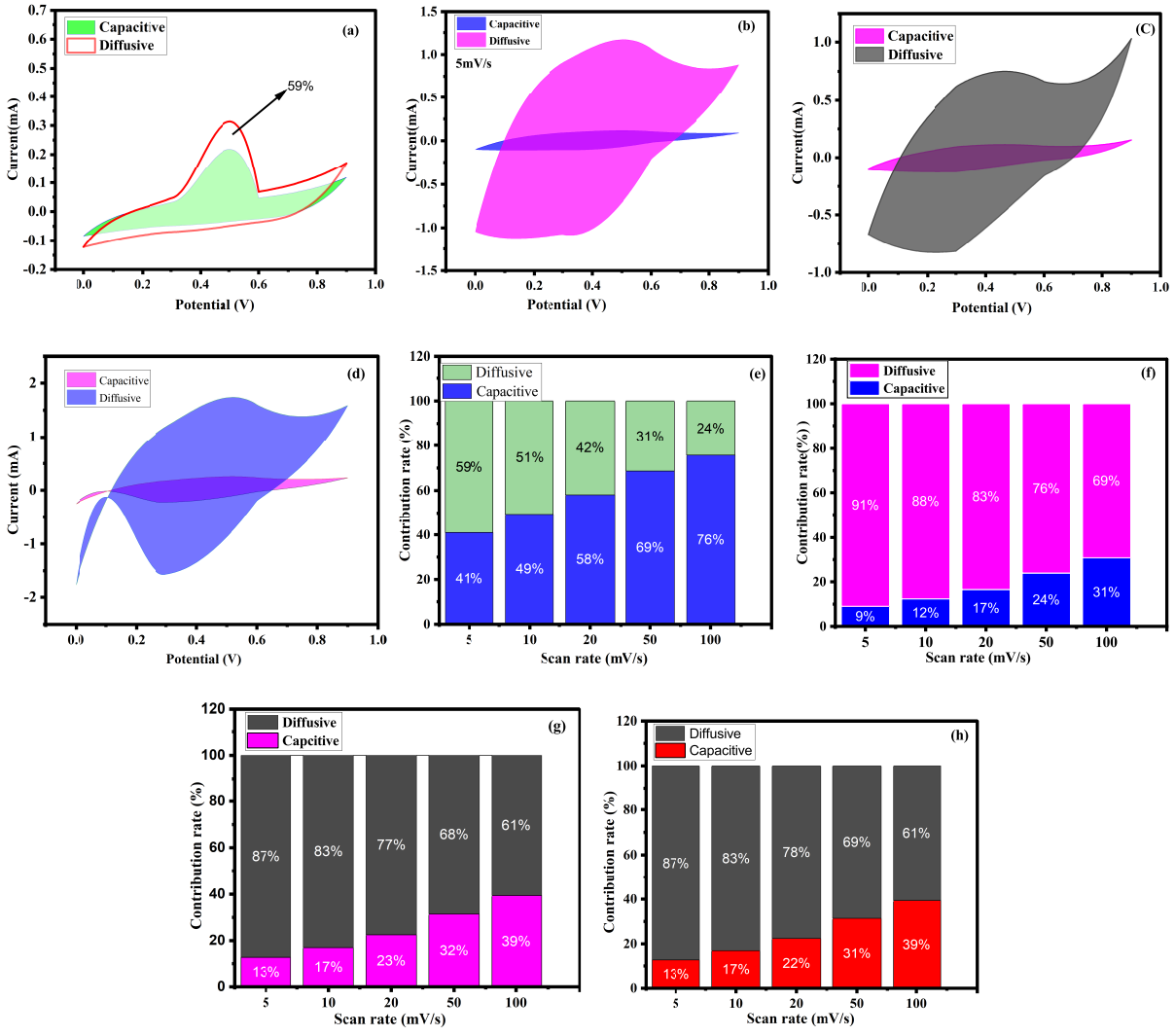

Figure 4.31: (a-d) a capacitive contribution analysis at a scan rate of 5 mVs^{-1}, and (e-h) Proportional contributions from capacitive and diffusion-controlled capacitances in various scan rates at 0.5V for BNO, BNO/PANI-10%, BNO/PANI-20%, BNO/PANI-30%, respectively.

The capacitive contribution of BNO and its PANI-based composites is clearly dependent on scan rate, indicating a balance between diffusion- and surface-controlled charge storage mechanisms as shown in Fig. 4.31. For pure BNO, the capacitive contribution is 41% at 5 mVs^{-1} and increases to 76% at 100 mVs^{-1}, demonstrating that capacitive-controlled behavior takes predominance at higher scan rates due to faster surface redox reactions and increased ion accessibility as shown in Fig. 4.31 (a, e), respectively. In comparison, the BNO/PANI-10% composite has a comparatively low capacitive contribution of 9% at 5 mVs^{-1}, which rises to 31% at 100 mVs^{-1}, as illustrated in Fig. 4.31 (b, f), respectively. Similarly, the BNO/PANI-20% electrode provides capacitive contributions of 13% and 39% at 5 and 100 mVs^{-1}, indicating a balanced improvement in capacitive and diffusion-controlled behavior as shown in Fig. 4.31 (c, g), respectively. Interestingly, the BNO/PANI-30% composite has essentially equal capacitive contributions to the 20% sample, showing that there is no significant gain in capacitive behavior over a specific PANI loading as illustrated in Fig. 4.31 (d, h). The capacitive contribution of SnO_2/BNO and SnO_2/BNO/PANI nanocomposites differs in charge storage behavior depending on scan rate and composite composition.

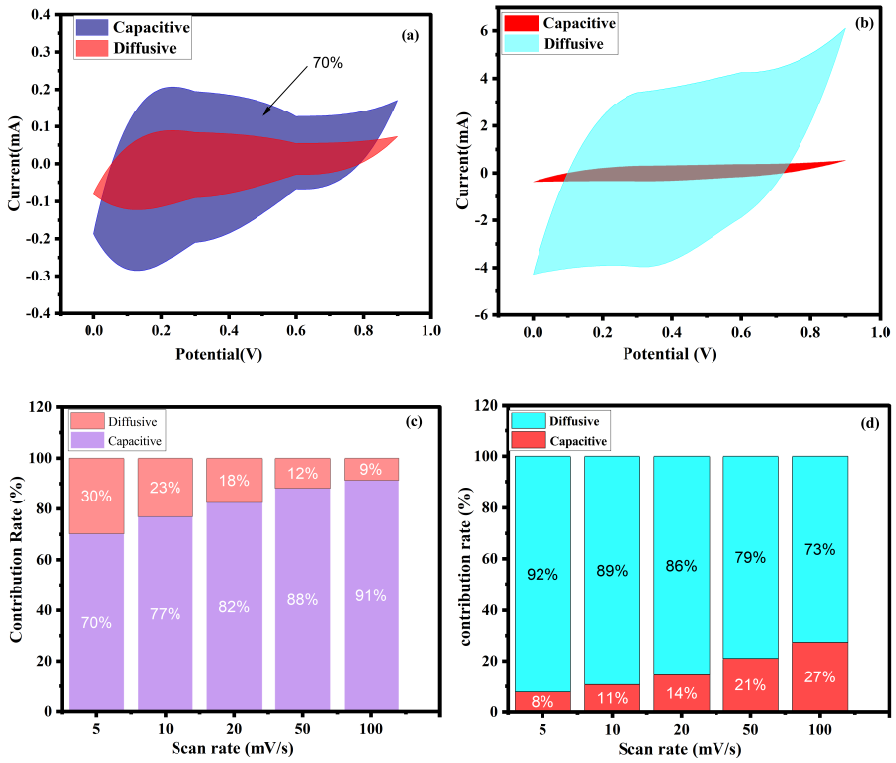

Figure 4.32: (a, b) a capacitive contribution analysis at a scan rate 5 mVs^{-1} for SnO_2/BNO, SnO_2/BNO/PANI, respectively and (c, d) Proportional contributions from capacitive and diffusion-controlled capacitances in various scan rates at 0.5V for SnO_2/BNO, SnO_2/BNO/PANI, respectively.

The capacitive contribution of the SnO_2/BNO electrode reaches 70% at 5 mVs^{-1} as shown in Fig. 4.32(a) and grows to 91% at 100 mVs^{-1}(see Fig. 4.32(c)), demonstrating that the charge storage mechanism is mostly regulated by surface-controlled capacitive behavior, particularly at higher scan rates. This shows that SnO_2 and BNO interact synergistically, resulting in efficient ion transport and quick redox kinetics. In contrast, the SnO_2/BNO/PANI nanocomposite has a comparatively low capacitive contribution of 8% at 5 mVs^{-1} (see Fig. 4.32 (b), which increases to 27% at 100 mVs^{-1} (Fig.4.31 (d) indicating, addition of PANI initially lowers a capacitive behavior.

4.7.5 Galvanostatic Charge-Discharge (GCD) Studies of SnO_2, and SnO_2/PANI-X Nanocomposites

The pure SnO_2 and SnO_2/PANI-X nanocomposite electrodes' GCD behavior were evaluate at a current densties of 0.1, 0.2, 0.3, 0.4, 0.5, 1, and 2 $A.g^{-1}$ in the potential range of 0 to 0.9 V is shown in Fig. 4.33(a-d). Good capacitive behavior is demonstrated by the symmetry of the charge and discharge characteristics. For pure SnO_2, however, GCD measurements were limited to a maximum current density of 1 $A.g^{-1}$, as higher current densities resulted in very short charge and discharge times, making further evaluation impractical.The specific capacitance (C_{SP}) of the nanomaterials were calculated from the charge-discharge curves,using Eq. (2.7). SnO_2/PANI-30% has the highest specific capacitance of about 338 $F.g^{-1}$ at 0.1 $A.g^{-1}$, which is almost 80, 2, and 2.8 times that of pristine SnO_2, SnO_2/PANI-10%, SnO_2/PANI-20%, respectively. This performance is superior to that of other SnO_2-based composites, as illustrated in Table 4.5

Table 4.5: Specific capacitance of the synthesized SnO_2, SnO_2/PANI-10%, SnO_2/PANI-20% and SnO_2/PANI-30% nanocomposites electrodes measured at current densities of 0.1–2 $A.g^{-1}$ in the potential range of 0–0.9 V.

Current densities ($A.g^{-1}$)	**Specific capacitance ($F.g^{-1}$) of the electrode material**			
	SnO_2	**SnO_2/PANI-10%**	**SnO_2/PANI-20%**	**SnO_2/PANI-30%**
0.1	4.2	162	120	338
0.2	3.7	57	64.7	135.8
0.3	3.3	33.3	50.2	100.4
0.4	3.1	22.8	40	61
0.5	2.9	17	33	43.5
1.0	2.4	13.4	15.2	22.7
2.0	–	2.1	2.2	5.6

Figure 4.33 (a-d) shows, the charge-discharge curves of SnO_2 and SnO_2/PANI-X composites at different current densities. These curves are reasonably symmetric and linear, indicating capacitive behavior with minor deviations. The charge-discharge curves of the SnO_2/PANI-

X nanocomposites exhibit an IR drop attributed to the internal resistance of the composites. With increasing PANI content, the SnO_2/PANI samples show a slightly curved charge-discharge profile, reflecting the characteristic redox behavior of pure polyaniline (Eftekhari et al., 2017; Prasanna et al., 2016, 2019).

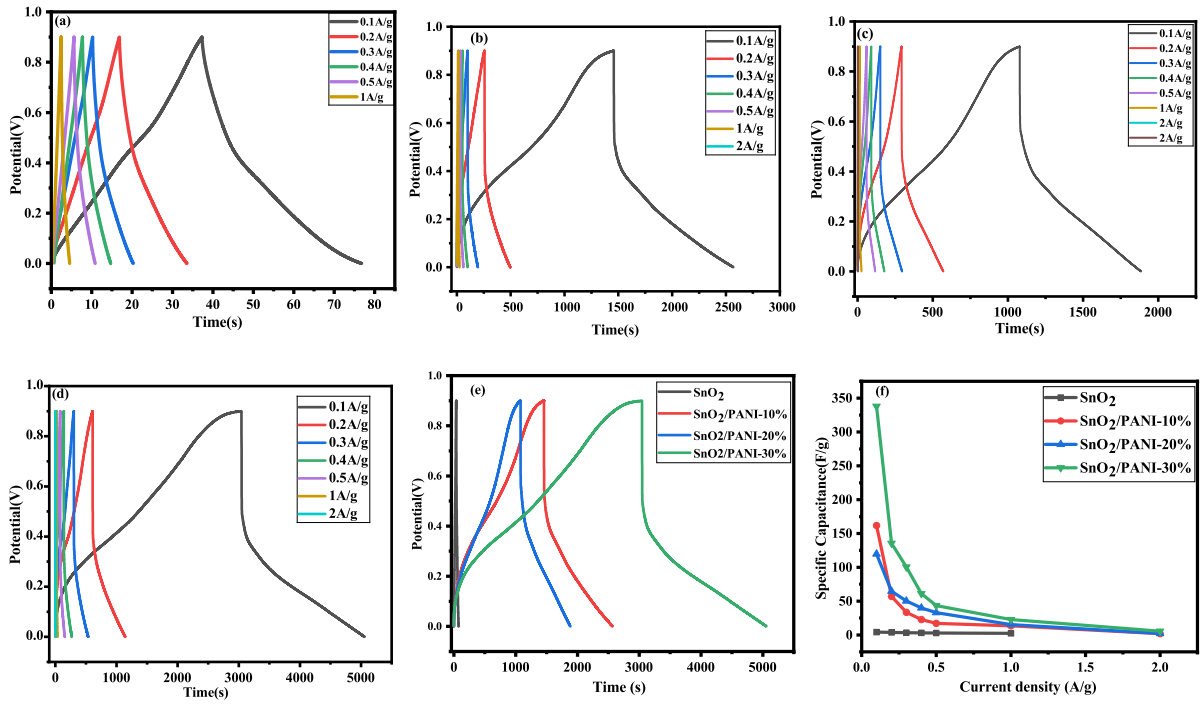

Figure 4.33: GCD of a) pure SnO_2, b) SnO_2/PANI-10%, c) SnO_2/PANI-20%, d) SnO_2/PANI-30%, e) SnO_2 and all composites at a current density of 0.1A.g^{-1}, and f) current density Vs. Specific capacitance in 1M H_2SO_4 aqueous electrolyte.

The SnO_2/PANI exhibits a synergistic effect of both components, complementing qualities. The presence of PANI attached to the surface of SnO_2 is responsible for the enhancement of specific capacitances. This modification of SnO_2 morphology makes both PANI and SnO_2 available for electrochemical reactions, which enhances the composite's efficiency. Additionally, as the weight percentage of PANI on the surface of SnO_2 increases, so does the specific capacitance, as indicated in Table 4.5. The slightly lower specific capacitance of SnO_2/PANI-20% at 0.1 A.g^{-1} is attributed due to partial aggregation of nanoparticles and the blocking of electrochemically active sites, which reduce effective ion accessibility under low-rate conditions. From the composites, SnO_2/PANI-30% has a longer charging and discharging time as shown in Fig. 4.33 (d). The decrease in specific capacitance at higher current densities is primarily due to limitations in electrochemical kinetics. At higher current densities, the rate at which charge and discharge processes occur is much faster (Sheoran et al., 2022). This rapid cycling can limit the time available for the complete redox reactions of polyaniline and the efficient use of SnO_2. As

a result, the overall charge storage efficiency decreases, leading to a reduction in specific capacitance. At lower current densities, the composite material can exhibit more ideal capacitive behavior, with nearly all of the material participating in the charge storage process. However, as the current density increases, the behavior can transition to a more resistive or pseudo-capacitive nature, where only the surface or near-surface regions of the material contribute effectively to capacitance. At high current densities, the rapid consumption of ions in the electrolyte near the electrode surface can lead to localized depletion zones, where the ion concentration is insufficient to sustain the maximum possible redox reactions. This effect further limits the overall capacitance (Pal et al., 2019).

4.7.6 Galvanostatic Charge-Discharge (GCD) Studies of BNO, and BNO/PANI-X Nanocomposites

Figure 4.34 (a-d) shows the GCD behavior of the pure BNO and BNO/PANI-X composite electrodes at current densities of 0.1, 0.2, 0.3, 0.4, 0.5, 1, and 2 Ag^{-1} in the potential range between 0 and 0.9 V. However, the GCD evaluation of BNO was performed only up to a current density of 1 Ag^{-1}. The charge and discharge characteristics of a BNO/PANI-X show good pseudocapacitive behavior. The specific capacitance was calculated from the charge-discharge curves, using Eq. (2.7). The highest specific capacitance calculated from the GCD curves for BNO, BNO/PANI-10%, BNO/PANI-20%, and BNO/PANI-30% is 9.69, 77.9, 161.5, and 211.11 Fg^{-1}, respectively, at a current density of $0.1Ag^{-1}$, as shown in Table 4.6. The charge-discharging specific capacitance of BNO/PANI-10%, BNO/PANI-20%, and BNO/PANI-30% is around 8, 16, and 21 times greater than the charge-discharge specific capacitance of pure BNO. Figure 4.34 (a-d) shows the charge-discharge curves of BNO and BNO/PANI-X composites at different current densities. These curves are reasonably symmetric and linear, indicating capacitive behavior with minor deviations. The charge-discharge curves of BNO/PANI-X nanocomposites display an IR drop due to the internal resistance of the composites. BNO/PANI-30% exhibits charge-discharge profiles that combine the characteristics of both BNO and PANI, delivering the longest discharge time compared to BNO/PANI-10% and BNO/PANI-20% at the same current density, as shown in Fig. 4.34 (e). The synergistic effect of BNO nanoparticles within the conductive PANI matrix enhances electrolyte ion diffusion, providing a larger surface area for effective utilization, resulting in the high specific capacitance.

Table 4.6: Specific capacitance of the synthesized BNO, BNO/PANI-10%, BNO/PANI-20%, and BNO/PANI-30% nanocomposite electrodes measured at current densities of 0.1–2 A.g^{-1} in the potential range of 0–0.9 V.

Current density (A.g^{-1})	Specific capacitance (F.g^{-1}) of the electrode material						
	0.1	**0.2**	**0.3**	**0.4**	**0.5**	**1.0**	**2.0**
BNO	9.69	3.15	2.06	1.66	1.47	1.45	–
BNO/PANI-10%	77.91	54.34	44.33	37.72	32.82	18.88	7.02
BNO/PANI-20%	161.40	85.52	64.19	52.09	44.57	25.30	11.51
BNO/PANI-30%	211.11	110.96	78.93	58.44	45.92	16.41	2.29

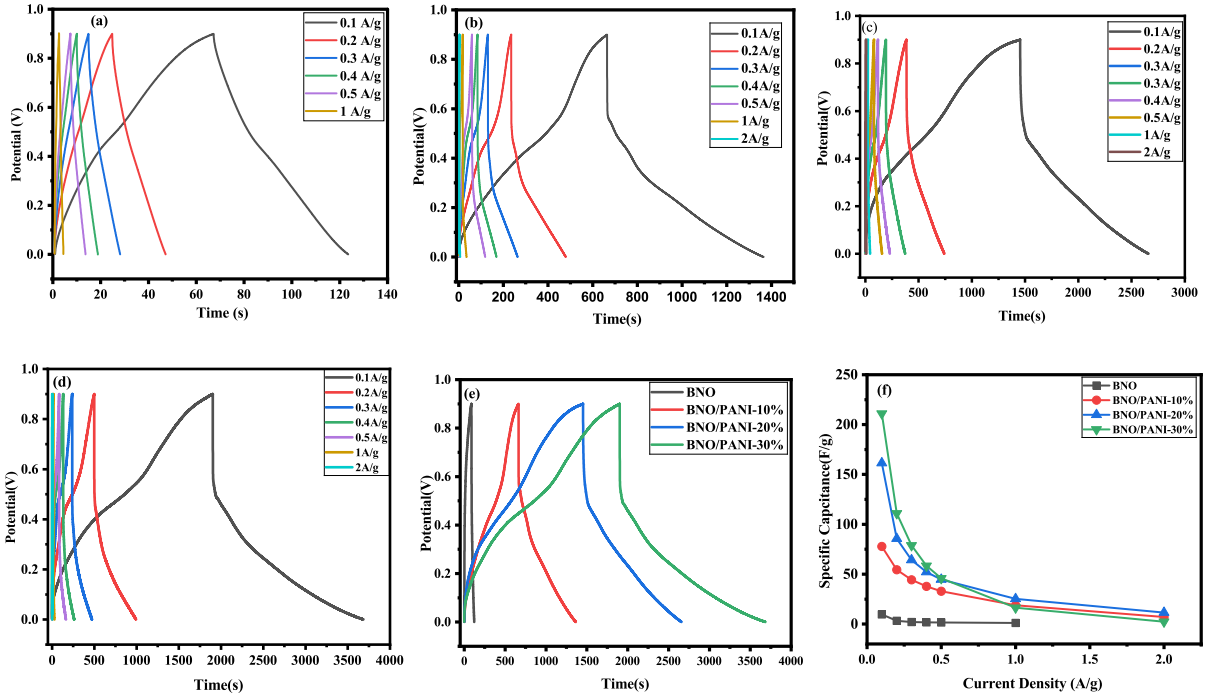

Figure 4.34: (a-d) GCD characteristics of pure BNO, BNO/PANI-10%, BNO/PANI-20%, and BNO/PANI-30% nanocomposites, respectively, and (e) comparison of charge-discharge properties of bare BNO and BNO/PANI-X nanocomposites at a current density of 0.1 Ag^{-1}, (f) specific capacitances of pure BNO and BNO/PANI-X nanocomposites at different current densities by charge-discharge analysis 1M H_2SO_4 aqueous electrolyte.

4.7.7 GCD Studies of SnO_2/BNO, SnO_2/BNO/PANI Nanocomposites

The GCD behavior of SnO_2/BNO composite electrodes was evaluated at current densities of 0.1, 0.2, 0.3, 0.4, 0.5, and 1A.g^{-1} within a potential range of 0-0.9 V, as shown in Fig. 4.35 (a), While, GCD testing of the SnO_2/BNO/PANI nanocomposite electrodes was extended to current densities up to 2 A.g^{-1} in the same potential range, as shown in Fig. 4.35 (b). For the pristine nanoparticles, measurements beyond 1A.g^{-1} were not feasible due to excessively short

charge/discharge times at higher current densities.

The specific capacitance (C_{SP}) values were determined from the GCD test using Eq. (2.7). The SnO_2/BNO nanocomposite exhibited specific capacitances of 5.22, 4.03, 3.40, 3.06, 2.85, and 2.35 $F\,g^{-1}$ at current densities of 0.1, 0.2, 0.3, 0.4, 0.5, and 1 $A\,g^{-1}$, respectively. In contrast, the ternary SnO_2/BNO/PANI nanocomposite showed significantly enhanced performance, delivering specific capacitances of 280.03, 164.18, 135.9, 119.5, 106.96, 66.0, and 20.6 $F\,g^{-1}$ at current densities of 0.1, 0.2, 0.3, 0.4, 0.5, 1, and 2 $A\,g^{-1}$, respectively. The GCD test reveal that SnO_2/BNO/PANI exhibits significantly higher specific capacitances, 280.03 $F.g^{-1}$, compared to SnO_2, BNO, and SnO_2/BNO (5.22 Fg^{-1}) at 0.1 $A.g^{-1}$, indicating that PANI incorporation greatly enhances charge storage capacity due to its conductive and pseudocapacitive properties. This analysis suggests that PANI plays a crucial role in boosting electrochemical performance, likely through enhanced conductivity and faradaic reactions.

The SnO_2/BNO/PANI ternary composite exhibits a slightly lower specific capacitance compared to the SnO_2/PANI-30% binary composite, which is unexpected since the inclusion of BNO was anticipated to further enhance capacitance due to synergistic effects. This discrepancy may arise from inefficient charge transfer between the three components, partial agglomeration of BNO, or reduced PANI accessibility for redox reactions during charge-discharge. However, the ternary composite still demonstrates a significant improvement over pristine SnO_2 and BNO, confirming that PANI remains the dominant contributor to capacitance.

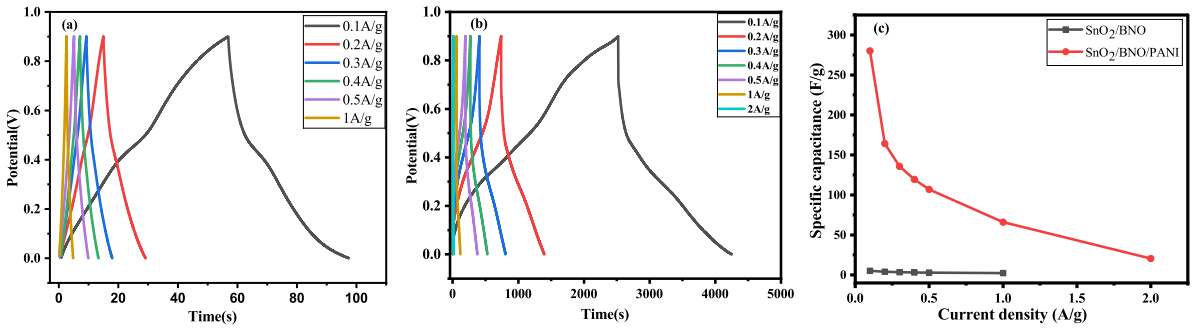

Figure 4.35: (GCD of a) SnO_2/BNO, b) SnO_2/BNO/PANI, and c) current density Vs. Specific capacitance in 1M H_2SO_4 aqueous electrolyte.

4.7.8 Cyclic Stability of Pure SnO_2, SnO_2/PANI-X Nanocompostes

Cyclic stability is the capability of a supercapacitor electrode or device to maintain its electrochemical performance during repeated charge-discharge cycling. It is one of the most important parameters for evaluating long-term reliability (Q. Wu et al., 2021). As shown in Fig. 4.36 (a-c), the cyclic stability of pristine SnO_2 was assessed at a current density of 1 $A.g^{-1}$, while the

cyclic stability of SnO_2/PANI-X was examined at a greater current density of 2 A.g^{-1} for 5000 cycles. After completing 5000 cycles, the pristine SnO_2 electrode maintained 95.04% of its original capacitance. In contrast, the SnO_2/PANI nanocomposite materials exhibited lower retention rates, with SnO_2/PANI-10% preserving 66.87%, SnO_2/PANI-20% maintaining 76.05%, and SnO_2/PANI-30% holding onto 61.35% of their original capacitance values, as shown in Fig. 4.36 (c). This variation in cyclic stability may arise from the increased current density applied to the SnO_2/PANI composites.

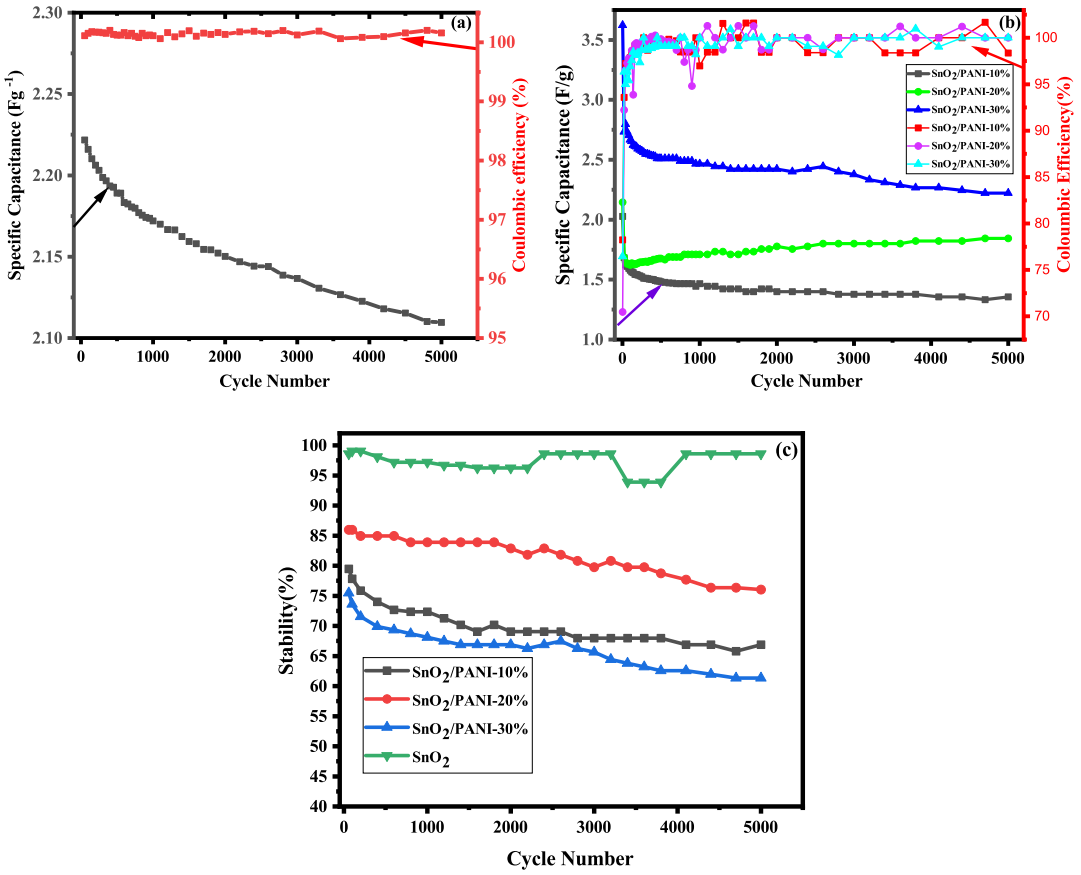

Figure 4.36: Cycling performance of a) Pristine SnO_2 at a current density of 1 A.g^{-1}, b) SnO_2/PANI-10%, SnO_2/PANI-20%, and SnO_2/PANI-30% nanocomposites at a current density of 2 A.g^{-1}, c) stability of the pristine SnO_2, and SnO_2/PANI-X nanocomposites for 5000 Cycles.

The initial decrease in capacitance retention at 10% PANI content is attributed to insufficient and non-uniform polymer coverage, which leads to interfacial instability and faster degradation of PANI during repeated redox cycling. Increasing the PANI content to 20% results in a more continuous and well integrated conductive network that enhances mechanical stabilization, charge-transfer stability, and electrode integrity, thereby improving cycling stability. However,

further increase of PANI loading to 30% causes a decline in retention due to an increase in the polymer content, which undergoes a gradual degradation during long term cycling, leading to loss of electrical contact and partial blockage of active sites. Additionally, the mechanical stress resulting from reduction-oxidation processes in conducting polymers (PANI) restricts stability over multiple charge-discharge cycles (Mujawar et al., 2011). Additionally, for 5000 charge-discharge cycles, the SnO_2/PAN-10%, SnO_2/PAN-20%, and SnO_2/PANI-30% nanocomposite electrodes demonstrated average Coulombic efficiency of 98.71%, 98.69%, and 98.59% (Fig. 4.36 (b)), which are less efficient than that of the pristine SnO_2 electrode, which demonstrated 100% of Coulombic efficiency.

4.7.9 Cyclic Stability of BNO, and BNO/PANI Nanocomposites

A life cycle test is a crucial additional metric used to determine the electrode materials' stability. As shown in Fig. 4.37 (a-d), the cyclic stability of BNO was evaluated at a current density of 1 Ag^{-1}, and the cyclic stability of BNO/PANI-X was examined at a current density of 2 Ag^{-1} for 5000 cycles. The bare BNO electrode was only able to retain 60% of its initial capacitance for the same number of cycles, while BNO/PANI-10%, BNO/PANI-20%, and BNO/PANI-30% nanocomposite materials were able to retain 45, 72, and 69% of the initial capacitance value after 5000 cycles, respectively. The mechanical stress resulting from reduction-oxidation processes in conducting polymers restricts stability over multiple charge-discharge cycles. The relatively poor cycling stability of the pristine BNO electrode originates from its low electrical conductivity and structural instability during repeated charge-discharge cycles. Continuous ion insertion/extraction induces mechanical stress and partial cracking, leading to the loss of electrochemically active sites and specific capacitance reduction. In the BNO/PANI composites, the conductive PANI network improves electron transport and serves as a flexible matrix that minimizes volume changes and prevents structural degradation. However, at low PANI loading (BNO/PANI-10%), insufficient and non-uniform polymer coverage results instability and accelerated polymer degradation, leading to lower capacitance retention compared to pristine BNO. Increasing the PANI content to 20% and 30% forms a more continuous conductive network, significantly improving cycling stability. However, excessive PANI may undergo shrinkage and gradual backbone degradation, which explains the slightly reduced retention of BNO/PANI-30% compared to BNO/PANI-20%. Moreover, for 5000 charge-discharge cycles, the BNO/PANI-10%, BNO/PANI-20%, and BNO/PANI-30% nanocomposite electrodes demonstrated average Coulombic efficiency of 97.13%, 98.32%, and 98.84%, respectively, as shown in Fig. 4.37 (b-d), which are more efficient than that of the pure BNO electrode, which only demonstrated 95.3% of Coulombic efficiency.

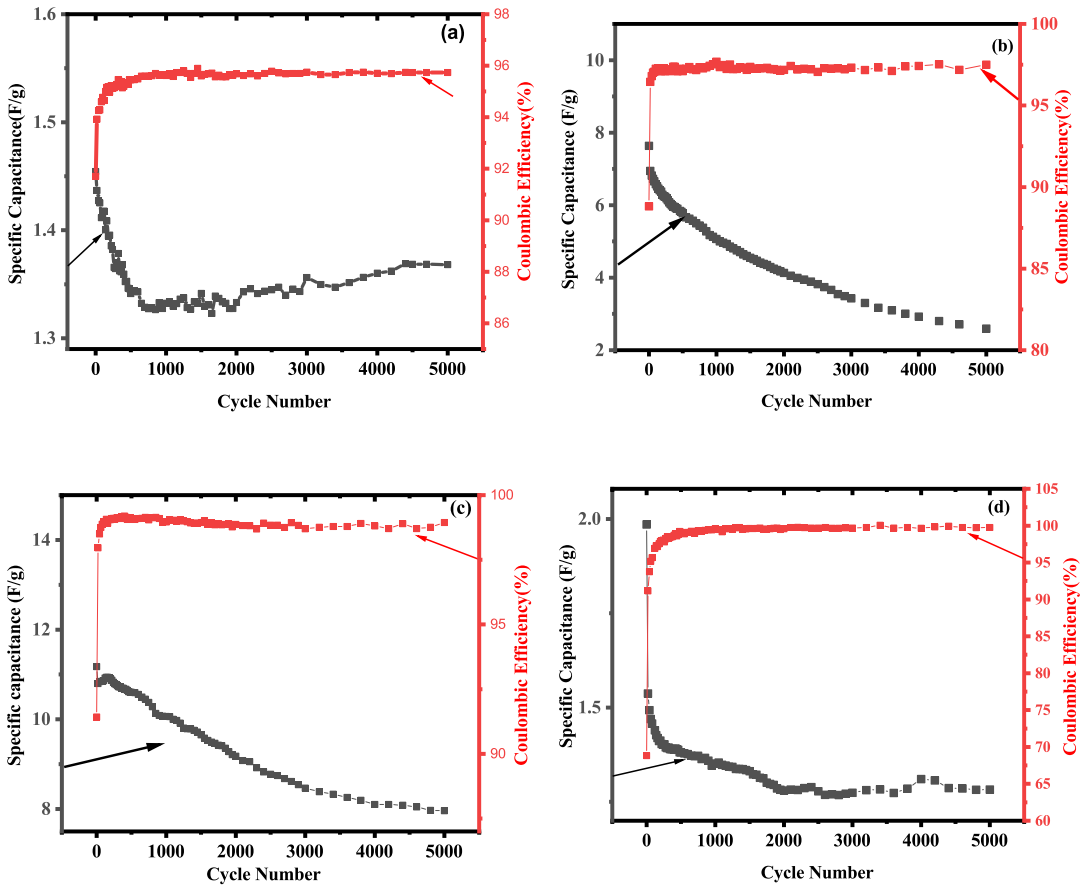

Figure 4.37: Extended cycling performance of a) BNO at a current density of 1 Ag^{-1}, b) BNO/PANI-10%, c) BNO/PANI-20%, d) BNO/PANI-30% nanocomposites at a current density of 2 Ag^{-1} for 5000 cycles, respectively.

4.7.10 Cyclic Stability of SnO_2/BNO and SnO_2/BNO/PANI Nanocomposites

The cyclic stability data reveal critical insights into the performance of each electrode material under the specified experimental conditions (0 to 0.9 V potential window in H_2SO_4 electrolyte). The SnO_2/BNO and SnO_2/BNO/PANI electrodes were found to have an average Coulombic efficiency of 100% and 99.25%, respectively, as shown in Fig. 4.38 (a, b). These numbers show low energy loss during cycling and outstanding charge/discharge reversibility. The SnO_2/BNO electrode's slightly higher efficiency can be due to its simpler structure, but the ternary nanocomposite's near unity efficiency nevertheless demonstrates its electrochemical stability and efficient charge storage behavior.

The cycling stability of the electrodes was evaluated at different current densities, with SnO_2/BNO tested at 1 $A.g^{-1}$ and SnO_2/BNO/PANI at 2 $A.g^{-1}$, as shown in Fig. 4.38(c). Despite the higher current density, the SnO_2/BNO/PANI ternary nanocomposite exhibited superior capacitance re-

tention compared to the binary SnO_2/BNO composite. Specifically, the SnO_2/BNO electrode retained 81%, 71%, 68%, 62%, and 59% of its initial capacitance after 100, 500, 1000, 2000, and 5000 cycles, respectively. In contrast, the SnO_2/BNO/PANI composite maintained higher retention values of 91%, 87%, 78%, 69%, and 64% at the same cycle numbers. The improved performance of the ternary composite, even under more demanding conditions, highlights the beneficial role of PANI in enhancing structural integrity and electrical conductivity, resulting in better long-term electrochemical stability.

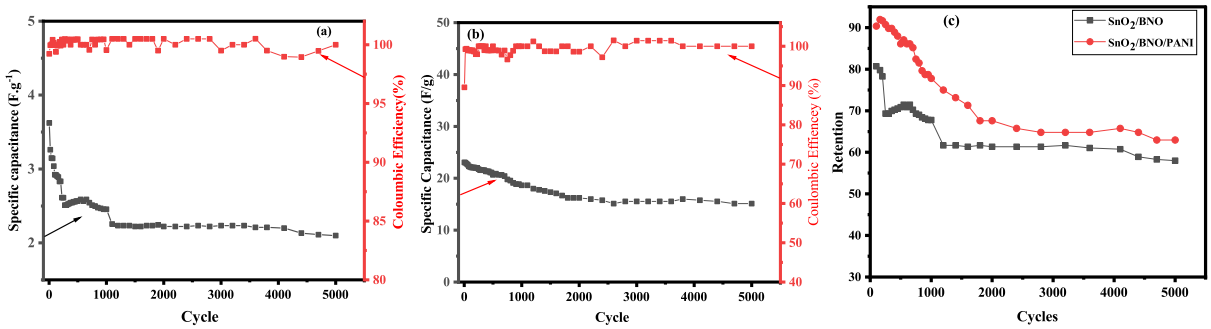

Figure 4.38: Cycling performance of a) SnO_2/BNO at a current density of 1 $A.g^{-1}$, b) SnO_2/BNO/PANI, nanocomposites at a current density of 2$A.g^{-1}$, c) retention of SnO_2/BNO and SnO_2/BNO/PANI nanocomposites for 5000 cycles.

4.7.11 Electrochemical Impedance Spectroscopy (EIS) Analysis of SnO_2, SnO_2/PANI-X Nanocomposites

EIS is frequently used to predict the dynamic properties of electrode materials during electrochemical reactions, focusing on aspects related to charge transfer and ion diffusion. An alternative method for assessing the electrochemical performance of supercapacitor materials is to qualitatively analyze the charge transfer resistance of the electrodes using electrochemical impedance spectroscopy (EIS) (Mirmohseni et al., 2012). EIS measurements were conducted in the frequency range of 0.01 Hz to 100 kHz and an open-circuit amplitude potential of 10 mV. The inset of Fig. 4.39 (a, b) illustrates a detailed view of the Nyquist plots for the SnO_2 and the SnO_2/PANI-X composites, respectively. The associated equivalent circuit model for the materials is shown in the inset of Fig. 4.39 (b). The major charge transfer process is indicated by a semicircle in the high-frequency region of the Nyquist plots for all the electrodes, while the main ionic diffusion process is indicated by a sloping line (Warburg-type element) in the low-frequency zone. The equivalent circuit diagram consists of elements such as the ohmic (solution) resistance (R_s), the charge transfer resistance (R_{ct}), a constant phase element (Q), Warburg impedance (W), and pseudo capacitance or additional capacitance (C).

The solution resistances for SnO_2, SnO_2/PANI-10%, SnO_2/PANI-20%, and SnO_2/PANI-30% are 0.67, 1.03, 0.58, and 0.78 Ω, respectively. These values account for the ionic resistance of the electrolyte, the intrinsic resistance of the active materials, and the contact resistance at the material interfaces. The relatively low resistance in SnO_2/PANI-20% (0.58 Ω) suggests improved conductivity and optimized interaction between SnO_2 and PANI at this composition, likely facilitating charge transfer. In contrast, the slightly higher resistance in SnO_2/PANI-10% (1.03 Ω) could result from limited PANI integration, while SnO_2/PANI-30% (0.78 Ω) may exhibit increased resistance due to potential aggregation or less effective ion diffusion pathways at higher PANI content. These differences highlight how the balance of components in the composites influences overall conductivity and the electrochemical performance of the materials (Xie & Ji, 2016).

The values presented in Table 4.7 demonstrate that the charge transfer resistances (R_{ct}) for SnO_2, SnO_2/PANI-10%, SnO_2/PANI-20%, and SnO_2/PANI-30% are 2.23, 6.43, 10.43, and 5.76 Ω, respectively. This shows that the SnO_2/PANI composites typically have higher R_{ct} values than pure SnO_2. The increase in charge transfer resistance (R_{ct}) with the addition of PANI, despite its inherently high conductivity, can be attributed to structural and interfacial factors introduced in the SnO_2/PANI composites. These interfaces can impede efficient electron transfer due to imperfect contact or localized charge trapping. Additionally, as the PANI content increases, the composite may develop a more disordered structure or reduced connectivity, leading to higher resistance paths for charge transfer. Thus, while PANI itself is conductive, the way it interacts with SnO_2 and the resulting composite morphology can introduce obstacles to charge transfer, increasing the R_{ct}. Notably, SnO_2/PANI-30% exhibits a reduction in R_{ct} to 5.76 Ω, suggesting that this particular composition strikes an optimal balance between improved capacitance and manageable charge transfer resistance. The constant phase element (Q) values for SnO_2, SnO_2/PANI-10%, SnO_2/PANI-20%, and SnO_2/PANI-30% are 55.092, 190.35, 524.74, and 700.73 $\mu F \cdot s^{(a-1)}$, respectively. The observed increase in Q values with greater PANI percentages indicates an improvement in surface heterogeneity and arise in effective capacitance due to the inclusion of PANI. This pattern may suggest that the SnO_2/PANI composites offer a greater number of active sites for charge storage, likely as a result of PANI's conductive properties, which enhance the electrochemical performance of the composites. However, the high Q values in the SnO_2/PANI-20% and SnO_2/PANI-30% composites might also point to potential aggregation at higher PANI content, which could impact long-term stability and charge transport efficiency.

The Warburg impedance (W) measurements for SnO_2, SnO_2/PANI-10%, SnO_2/PANI-20%, and SnO_2/PANI-30% are recorded as 41.54, 18.04, 5.92, and 5.56 $\Omega.s^{(-1/2)}$, respectively. These

values represent the Warburg impedance related to the ion diffusion within the electrochemical system. The observed pattern indicates a decline in Warburg impedance with an increase in PANI content. For SnO_2, the elevated W value signifies a considerable resistance to ion diffusion, implying that the material's structure does not promote efficient ion transport. As the PANI ratio rises from 10% to 30%, the W values diminish, reflecting enhanced ion diffusion characteristics. This enhancement is likely attributed to the greater amount of PANI, which offers improved conductive pathways for ion mobility. Therefore, the lower Warburg impedance values for SnO_2/PANI-20% and SnO_2/PANI-30% imply that these composites are more effective in promoting ion diffusion, thereby improving the overall electrochemical efficacy of the material (Y. Li et al., 2018).

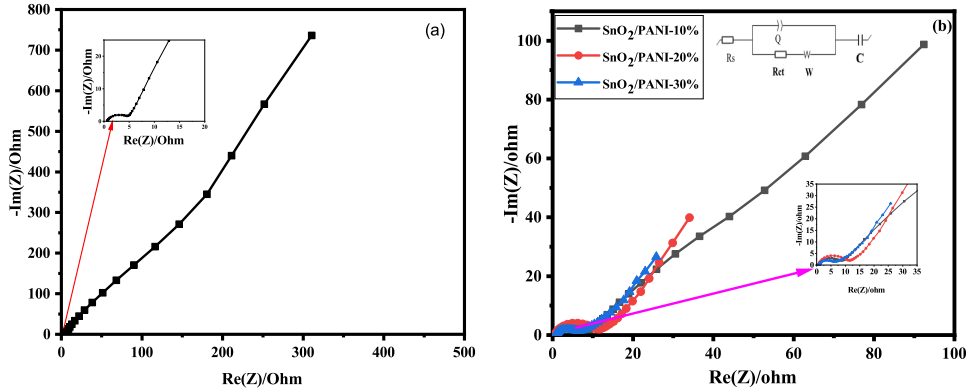

Figure 4.39: Nyquist plots of (a) SnO_2 Nanoparticles and (b) SnO_2/PANI-X. Nanocomposites

Table 4.7: EIS best fitting data of SnO_2, SnO_2/PANI-10%, SnO_2/PANI-20%, and SnO_2/PANI-30% nanocomposites

Electrodes	R_s (Ω)	R_{ct} (Ω)	Q ($\mu F.s^{(a-1)}$)	W ($\Omega.s^{1/2}$)	C (F)	a
SnO_2	0.67	2.29	55.092	41.54	0.0193	1.00
SnO_2/PANI-10%	1.03	6.43	190.35	18.04	0.5536	0.87
SnO_2/PANI-20%	0.58	10.29	524.74	5.92	0.9324	0.84
SnO_2/PANI-30%	0.78	5.76	700.73	5.56	4.3614	0.79

4.7.12 Electrochemical Impedance Spectroscopy (EIS) studies of BNO, and BNO/PANI-X Nanocomposites

The Nyquist plots for all electrodes display a semicircle in the high-frequency region, which represents the primary charge transfer process, and a straight line in the low-frequency region,

representing the capacitive behavior of the prepared electrode materials, as shown in Fig. 4.40. The equivalent circuit diagram comprises equivalent elements, such as the ohmic resistance (R_1), the charge transfer resistance (R_{ct}) or (R_2), and the constant phase element (CPE) (Q), as shown in Fig. 4.40 (c).

The ohmic resistances (R1) of BNO, BNO/PANI-10%, BNO/PANI-20%, and BNO/PANI-30% are 1.508, 1.343, 0.943, and 0.615 Ω, respectively, as shown in Table 4.8. These resistance values encompass the ionic resistance of the electrolyte, the intrinsic resistance of active materials, and contact resistance at the interfaces. This consistent pattern demonstrates that PANI enhances the conductivity of the composite material and the electrolyte system, thereby contributing to the enhanced electrochemical performance of the BNO/PANI-X composites. According to the fitting values as shown in Table 4.8, R_2 (R_{ct}) of BNO, BNO/PANI-10%, BNO/PANI-20%, and BNO/PANI-30% are 17.034, 9.262, 5.722, and 4.721 Ω, respectively. This indicates that BNO/PANI-X composites have less charge transfer resistance than the pristine BNO. There is a significant decrease in R_{ct} with increasing PANI content in the composites, further underscoring the effect of PANI in enhancing the conductivity of the materials. This tendency indicates that PANI significantly enhances the electrochemical performance by facilitating more efficient charge transfer. The low values of R_1 and R_2 (R_{ct}) are attributed to the PANI dispersed in the BNO nanoparticle, which facilitates the efficient access of electrolyte ions to the BNO surface. Therefore, BNO/PANI-30% shows good electrochemical performance for supercapacitor applications.

The fitting values of the Constant Phase Element (CPE) for BNO and its composites with PANI (10%, 20%, and 30%) reveal significant variations in capacitive behavior due to the incorporation of PANI. The CPE coefficient (Q) increases with higher PANI content, indicating enhanced capacitive characteristics. For pure BNO, Q_2 is 30.2 ($\mu F{\cdot}s^{(a-1)}$), which rises to 371.8 ($\mu F{\cdot}s^{(a-1)}$) for the 30% PANI composite, suggesting improved charge storage capability. Similarly, Q_3 increases from 4757.5 ($\mu F{\cdot}s^{(a-1)}$) to 70340.8 ($\mu F{\cdot}s^{(a-1)}$), reflecting a more pronounced non-ideal capacitive behavior, likely resulting from the increased surface roughness or porosity introduced by PANI. The exponent α values, all ranging between 0 and 1, confirm the non-ideal nature of the capacitance, with deviations from ideal behavior becoming more pronounced as the PANI content increases. This trend highlights the role of PANI in modifying the electrochemical characteristics of the composites, thereby enhancing their suitability for energy storage and other electrochemical applications.

The magnitudes of total impedance ($|Z_{\text{total}}|$) for BNO and its PANI composites decrease significantly with increasing PANI content, from 2.91 Ω (BNO) to 0.68 Ω (30% PANI) at 100 kHz, as presented in Table 4.8. This reduction indicates that the incorporation of PANI enhances

the electrical conductivity and charge-transfer characteristics of the composites. The improved performance can be attributed to the formation of a conductive PANI network, which reduces ohmic resistance and facilitates faster electron transport throughout the electrode structure.

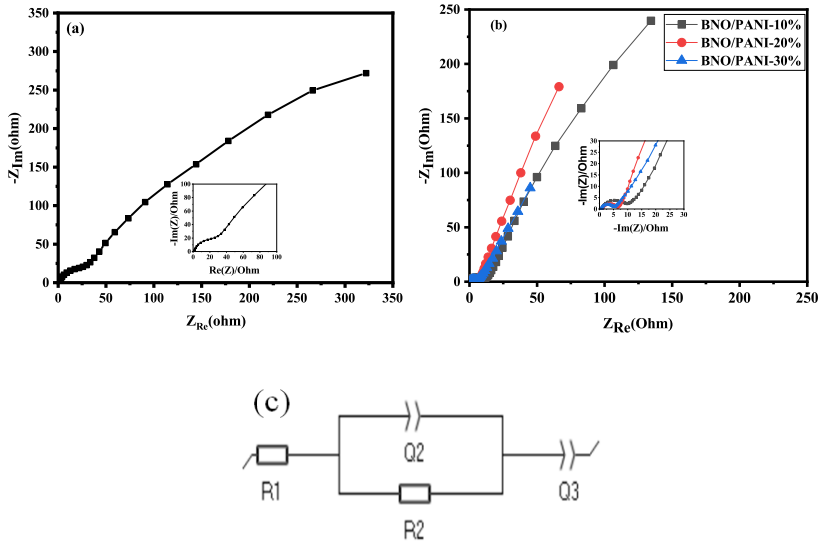

Figure 4.40: Nyquist plots of (a) BNO, (b) BNO/PANI-X, and (c) the electrical equivalent circuit model.

Table 4.8: EIS best fitting data of BNO, BNO/PANI-10%, BNO/PANI-20%, and BNO/PANI-30% nanocomposites

Electrodes	$\mathbf{R}_1$ (Ω)	$\mathbf{R}_2$ (Ω)	$\mathbf{Q}_2$ (μF·s$^{(a_2-1)}$)	$\mathbf{Q}_3$ (μF·s$^{(a_3-1)}$)	$\mathbf{a}_2$	$\mathbf{a}_3$	$\lvert Z_{\text{total}}\rvert$ (Ω)
BNO	1.508	17.034	30.2	4757.5	0.922	0.768	2.91
BNO/PANI-10%	1.343	9.262	198.5	23341.0	0.847	0.700	1.46
BNO/PANI-20%	0.943	5.722	219.0	45502.2	0.846	0.787	1.04
BNO/PANI-30%	0.615	4.721	371.8	70340.8	0.856	0.676	0.68

4.7.13 EIS Studies of SnO_2/BNO and SnO_2/BNO/PANI Nanocomposites

The dynamic characteristics of electrode materials (SnO_2/BNO and SnO_2/BNO/PANI) in electrochemical reactions are frequently estimated using EIS, as shown in Fig. 4.41(a). The inset of Fig. 4.41(a) displays zoomed-in EIS Nyquist graphs, whereas Fig.4.41(b) displays the materials equivalent circuit model. The Nyquist plots of all electrodes show a straight line in the low-frequency region, indicative of capacitive behavior, and a semicircle in the high-frequency zone, indicating dominant charge transfer mechanisms. As shown in Fig.4.41(b), the analogous circuit design comprises equivalent components, including the constant phase element (CPE)

(Q), the charge transfer resistance (R_2) (R_{ct}), and the ohmic resistance (R_1). According to Table 4.9, the relative solution resistances (R_1) for SnO_2/BNO and SnO_2/BNO/PANI are 0.558 and 0.695 Ω, respectively. These resistance values include the electrolyte ionic resistance, the active materials' intrinsic resistance, and the interface's contact resistance. The EIS results indicate that the SnO_2/BNO/PANI composite exhibits the lowest charge transfer resistance (2.354 Ω), suggesting superior electrochemical conductivity and interfacial charge transfer efficiency compared to pristine and binary composites. The lowest resistance in the ternary SnO_2/BNO/PANI composite indicates that the incorporation of PANI with SnO_2 and BNO further enhances charge separation and transport, making it the most efficient among the tested materials for potential applications in energy storage.

Table 4.9: EIS fitting data of the synthesized nanomaterials

Electrodes	**(R_1)(Ω)**	**(R_2)(Ω)**	**Q_2(μF·s$^{(a_2-1)}$)**	**Q_3(μF·s$^{(a_3-1)}$)**	**a_2**	**a_3**	**—Z_{total}—(Ω)**
SnO_2/BNO	0.558	4.228	400.935	13996.29	0.852	0.934	25.1
SnO_2/BNO/PANI	0.695	2.354	582.36	231462.16	0.813	0.697	1.95

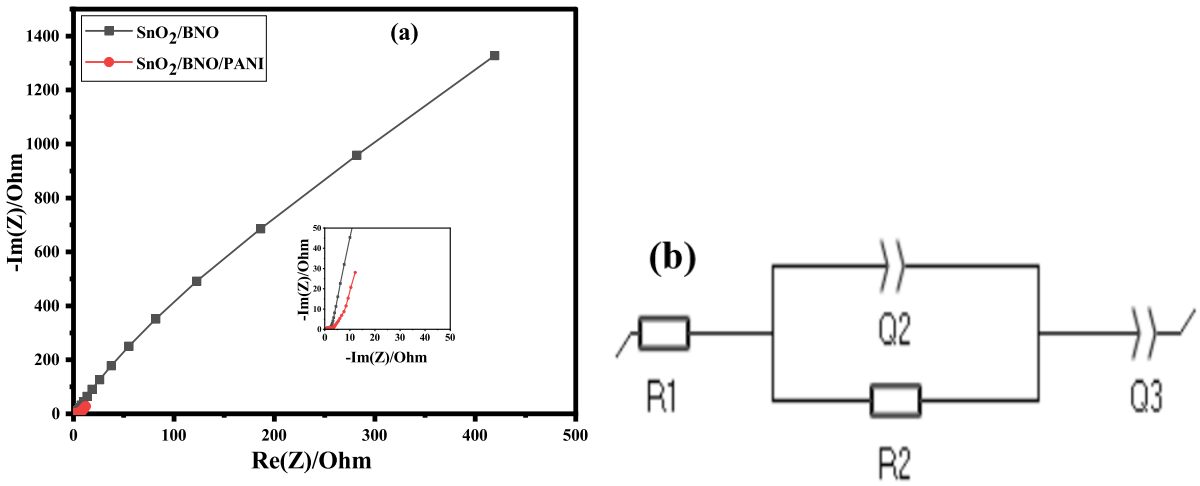

Figure 4.41: Nyquist plots of (a) SnO_2/BNO and SnO_2/BNO/PANI, and (b) corresponding electrical circuit model.

The higher Q_2 (CPE_{dl}) values for SnO_2/BNO/PANI (582.36 $\mu F \cdot s^{(\alpha-1)}$) indicate improved double-layer capacitance, attributed to PANI pseudocapacitive contribution and increased electroactive surface area. Meanwhile, the exceptionally high Q_3 (CPE_{dl} values for SnO_2/BNO/PANI 231462.16 $\mu F \cdot s^{(\alpha-1)}$) suggest enhanced ion diffusion and bulk charge storage, likely due to PANI's redox-active sites and the porous structure facilitating electrolyte penetration. Overall, SnO_2/BNO/PANI demonstrates the best performance with low R_{ct}, moderate CPE_{dl}, and

efficient bulk storage, making it a promising electrode for high-performance supercapacitors. The SnO_2/BNO/PANI composite exhibits the lowest total impedance (1.95 Ω), demonstrating superior charge transport and conductivity compared to pure SnO_2, BNO, SnO_2/BNO, and SnO_2/PANI, as shown in Table 4.9. The high impedance of BNO alone confirms its insulating nature, while the significant reduction in SnO_2/BNO suggests improved interfacial charge transfer due to the composite. The further decrease in impedance for SnO_2/BNO/PANI highlights the crucial role of PANI in enhancing conductivity through its redox-active and conductive polymer properties. The ternary SnO_2/BNO/PANI composite achieves the best performance, combining low resistance and efficient charge storage, making it an excellent candidate for high-performance supercapacitor electrodes.

Table 4.10: Comparative literature results of SnO_2 and Bismuth-based electrodes from earlier reports with those of the present work.

Electrode Materials	Electrolyte	$C_{SP}\,(Fg^{-1})$	Scan rate / Current density	References
Chitosan-SnO_2–PANI	1M H_2SO_4	179.2	10 mV s^{-1}	(Karpuraranjith et al., 2016)
SnO_2/rGO	1M Na_2SO_4	262.2	0.1 A g^{-1}	(Y. Zhang et al., 2020)
SnO_2@C	1M KOH	28.5	0.1 A g^{-1}	(Ren et al., 2014)
$ZnWO_4/SnO_2$	2 M KOH	56.7	1 mV s^{-1}	(Vinayaraj et al., 2020)
MoS_2/SnO_2	2 M KOH	61.6	10 mV s^{-1}	(Prabukumar et al., 2019)
SnO_2/g-C_3N_4	3MNa_2SO_4	302.7	1 A g^{-1}	(R. Kumar et al., 2024)
SnS_2–SnO_2	1 M KOH	149	2 A g^{-1}	(Asen et al., 2019)
SnO_2/PANI	1 M H_2SO_4	335.5	0.1 A g^{-1}	(Wang et al., 2014)
$BiFeO_3$	1 M NaOH	101.65	10 mV s^{-1}	(Jadhav et al., 2016)
Bi_3YO_6	3 MNa_2SO_4	66	4 mA cm^{-2}	(Sajjad et al., 2021)
Graphene/Bi_2O_3	6 M KOH	255	1 A g^{-1}	(H.-W. Wang et al., 2010)
WO_3/PANI	0.5 M H_2SO_4	96	5 mV s^{-1}	(Amaechi et al., 2015)
rGO/Bi_2O_3	1 M KOH	216	10 mV s^{-1}	(W.-D. Yang & Yu-Jiang, 2019)
Bi_2O_3/MnO_2	1 M NaOH	161	1 A g^{-1}	(Singh et al., 2019)
$BiVO_4$–Ag	3 M Na_2SO_4	109	1 A g^{-1}	(Z. J. Zhang et al., 2017)
Bi_2O_3/Bi_2WO_6	1 MKOH	148.81	1 A g^{-1}	(Gote et al., 2019)
SnO_2/PANI–30%	1 M H_2SO_4	338	0.1 A g^{-1}	**This work**
$Bi_5Nb_3O_{15}$/PANI–30%	1 M H_2SO_4	216	5 mV s^{-1}	**This work**
SnO_2/BNO/PANI	1 M H_2SO_4	424	5 mV s^{-1}	**This work**

4.8 Electrochemical Characterization of Assembled Asymmetric Supercapacitor (ASC) Devices

4.8.1 CV Analysis of Assembled Asymmetric Supercapacitor Devices

In the three-electrode configuration, SnO_2/PANI-30% demonstrated the highest specific capacitance when compared to its lower PANI content counterparts, SnO_2/PANI-10% and SnO_2/PANI-20%. Similarly, BNO/PANI-30% exhibited superior capacitive performance relative to BNO/PANI-10% and BNO/PANI-20%. This enhanced electrochemical behavior confirmed the effectiveness of the 30% PANI-loaded composites, leading to the selection of SnO_2/PANI-30% and BNO/PANI-30% as the optimal positive electrode materials for subsequent device fabrication.

The energy storage performance of SnO_2/PANI-30%, BNO/PANI-30%, and SnO_2/BNO/PANI nanocomposites was systematically evaluated through the fabrication of ASC devices. Each device was assembled in a Swagelok cell configuration, using the respective nanocomposite as the positive electrode and activated carbon (AC) as the negative electrode. All devices employed 1M H_2SO_4 as the electrolyte. As shown in Fig. 4.42 (b, d), SnO_2/PANI-30% and SnO_2/BNO/PANI operated efficiently within the potential window of 0-1.4 V, whereas BNO/PANI-30% was restricted to a smaller window of 0-0.9 V. CV measurements for AC (see Fig. 4.42 (a)), SnO_2/PANI-30%, BNO/PANI-30%, and SnO_2/BNO/PANI electrodes were recorded at scan rates of 5, 10, 20, 50, and 100 mVs^{-1}, like in the three-electrode configuration. These CV curves were instrumental in determining the optimal potential windows and capacitive behavior of each electrode material. The AC electrode, tested in the potential window of -0.3 to 0.4 V, exhibited electric double layer capacitance (EDLC), primarily driven by electrostatic ion adsorption at the electrode-electrolyte interface (Ndipingwi et al., 2022).

Consequently, an ASC voltage window of 1.4 V was adopted for all devices, except for BNO/PANI-30%, which remained stable only up to 0.9 V. To ensure efficient charge transfer and maximize electrochemical performance, mass balance between the positive and negative electrodes was achieved using the mass-charge balance equation (Eq. 2.10).

The CV profiles of the assembled ASC devices (AC//SnO_2/PANI-30%, AC//BNO/PANI-30%, and AC//SnO_2/BNO/PANI), presented in Fig.4.42 (b-d), demonstrated quasi-rectangular shapes across varying scan rates, indicating predominant pseudocapacitive behavior. This hybrid configuration combines EDLC from the AC electrode and pseudocapacitance from the nanocomposites, enabling the device to exploit broader potential windows and enhancing energy density.

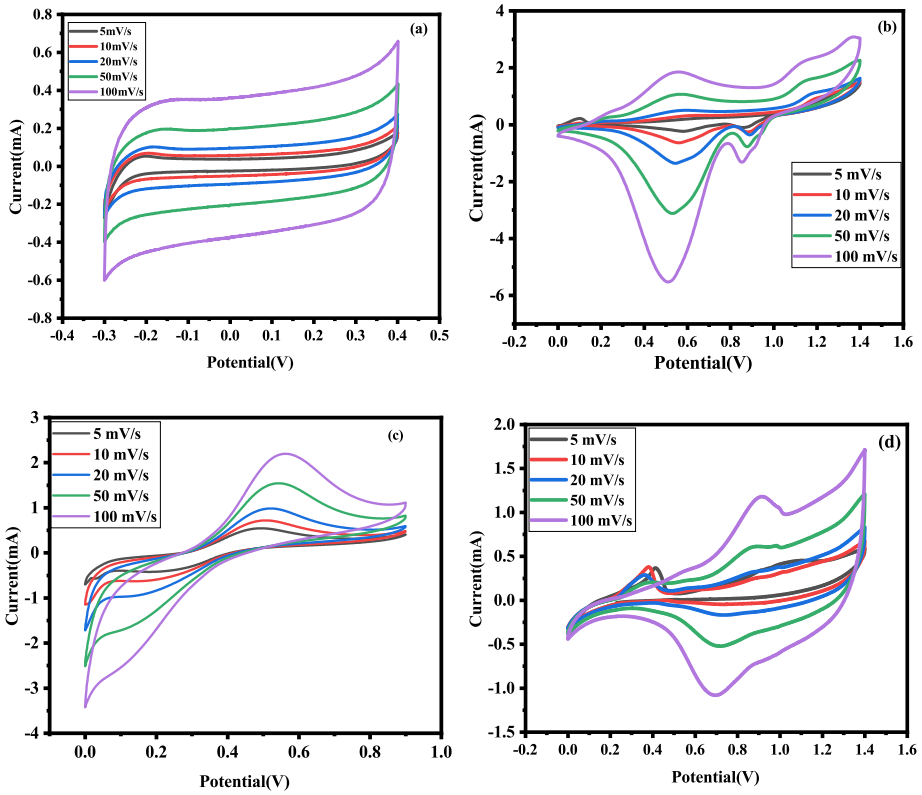

Figure 4.42: a) CV curves of Activated carbon (AC), (b) CV curves of AC/SnO_2/PANI-30%, (c) CV curves of AC/BNO/PANI-30%, and d) CV curves of AC/SnO_2/BNO/PANI for supercapacitor device in 1M H_2SO_4 aqueous electrolyte.

4.8.2 GCD Analysis of Assembled Asymmetric Supercapacitor(ASC) Devices

Galvanostatic charge/discharge (GCD) measurements were performed to evaluate the specific capacitance of the asymmetric supercapacitor (ASC) devices composed of activated carbon (AC) as the negative electrode and nanocomposite materials as the positive electrodes. The specific capacitance (C_{SP}) was calculated from the discharge curves using the following Eq. 2.11. The GCD curves for the AC//SnO_2/PANI-30% device were recorded at current densities of 0.3, 0.5, 0.6, 0.8, and 1 A.g^{-1} within a voltage window of 1.4 V, as shown in Fig. 4.43 (a). The calculated specific capacitance values were 237.38, 229.22, 193.59, 152.22, and 153.43 Fg^{-1}, respectively. These results show a consistent decrease in capacitance with increasing current, which is attributed to reduced ion diffusion and limited utilization of active sites at higher rates.

For the AC//BNO/PANI-30% device, GCD measurements were conducted at 0.1, 0.2, 0.3, 0.4, 0.5, and 1A.g^{-1} using a 0.9 V cell voltage as shown in Fig. 4.43 (b). The corresponding specific capacitances were found to be 475.44, 334.24, 283.86, 243.13, 207.06, and 84.38 Fg^{-1}, respectively. A sharp decline in capacitance at higher current densities suggests a drop in charge

storage efficiency, which is likely due to polarization effects and slower ion transport kinetics at elevated currents.

The ternary AC//SnO_2/BNO/PANI device was tested at relatively higher current loads of 0.2, 0.3, 0.4, 0.5, 0.8, 1, and 2 $A.g^{-1}$ under a voltage window of 1.4 V, as shown in Fig. 4.43 (c). The calculated specific capacitances were $247.52, 190.67, 161.55, 142.09, 118.96, 104.62,$ and $87.75\ Fg^{-1}$, respectively. These values demonstrate a moderate decrease in performance with increasing current, indicating stable and efficient charge-discharge behavior, even under high rate conditions. Among the tested configurations, the AC//BNO/PANI-30% device exhibited the highest specific capacitance at low current density ($475.44\ F.g^{-1}$ at $0.1\ A.g^{-1}$), though it showed significant loss at higher loads. In contrast, AC//SnO_2/PANI-30% and especially AC//SnO_2/BNO/PANI displayed better capacitance retention across a broad range of current densities.

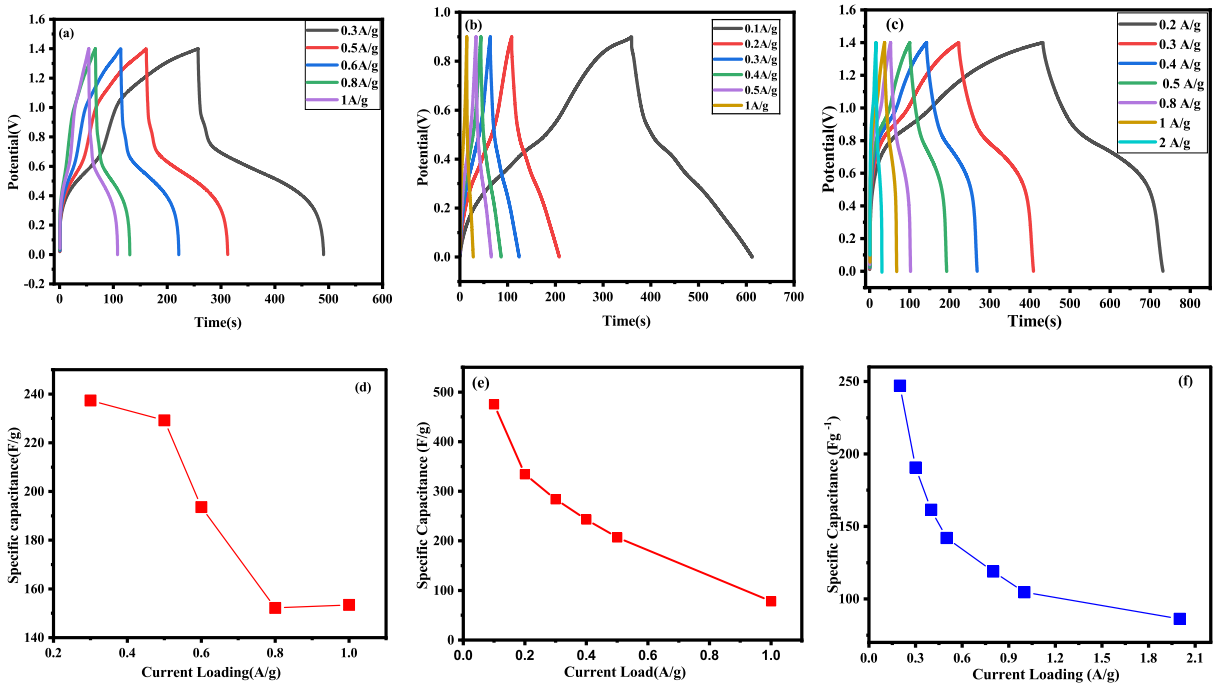

Figure 4.43: (a) GCD of AC//SnO_2/PANI-30%, (b) GCD of AC//BNO/PANI-30%, (c) GCD of AC//SnO_2/BNO/PANI, and (d) Specific capacitance Vs current load of AC//SnO_2/PANI-30%, (e) Specific capacitance vs current load of AC//BNO/PANI-30%, (f) Specific capacitance Vs current load of AC//SnO_2/BNO/PANI calculated from GCD of the supercapacitor device in 1M H_2SO_4 electrolyte.

4.8.3 Specific Energy and Power Density Analysis of the Fabricated Asymmetric Supercapacitors (ASCs)

Specific energy and power are key factors in supercapacitor applications that show the device's effectiveness and applicability for various uses. The energy and power density of the ASCs AC//SnO_2/PANI-30%, AC//BNO/PANI-30%, and AC//SnO_2/BNO/PANI were determined using Eq. (2.12) and (2.13). For the AC//SnO_2//PANI-30% ASC, the energy densities were $64.62, 62.40, 52.70, 41.44$, and 41.76 Wh.$kg^{-1}$ at current densities of 0.3, 0.5, 0.6, 0.8, and 1 A.g^{-1}, respectively. The corresponding power densities reached 840, 1400, 1680, 2240, and 2800 W.kg^{-1} at the same current densities as shown in Fig. 4.44 (a). For the AC//BNO/PANI-30% ASC, the energy densities were 53.49, 37.61, 32, 27.35, 23.30, and 9.4 Wh.kg^{-1} at current densities of 0.1, 0.2, 0.3, 0.4, 0.5, and 1A.g^{-1}, respectively. The corresponding power densities reached 180, 359.72, 540.09, 720, 900, and 1947.62 W.kg^{-1} at the same current densities, as shown in Fig. 4.44 (b). Meanwhile, the AC//SnO_2/BNO/PANI ASC demonstrated energy densities of 67.27, 51.90, 43.98, 38.68, 32.38, 28.48, and 24.20 Wh.kg^{-1} at current densities of 0.2, 0.3, 0.4, 0.5, 0.8, 1, and 2 A.g^{-1}, respectively, with power densities of 560, 840, 1120, 1400, 2240, 2800, and 5600 W.kg^{-1}, as shown in Fig. 4.44(c). These findings reveal the differences in energy storage and power delivery between the two ASC configurations under varying current loads. The AC//SnO_2/BNO/PANI assembly achieved a significantly higher maximum power density of 5600 W.kg^{-1} at 2 A.g^{-1}, compared to 2800 W.kg^{-1} at 1 A.g^{-1} for AC//SnO_2/PANI. This suggests that while the BNO-modified device sacrifices some energy retention at high currents, it offers superior power capability at extreme current loads.

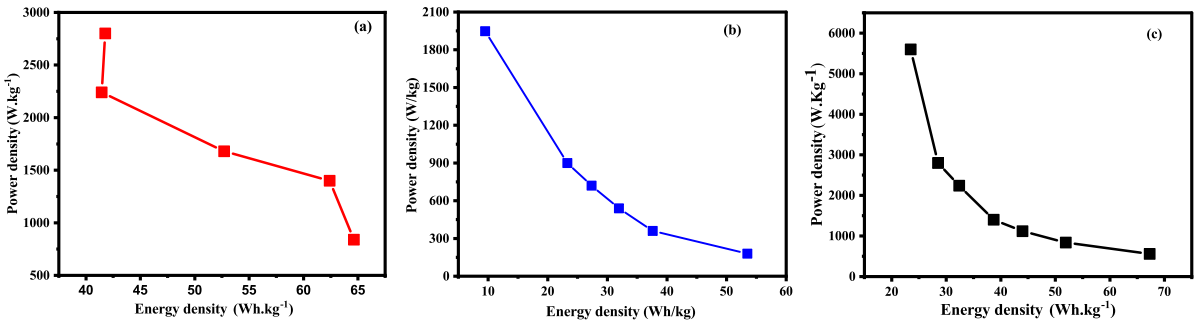

Figure 4.44: Ragone plot of a) AC//SnO_2/PANI-30%, b) AC//BNO/PANI-30% and c) AC//SnO_2/BNO/PANI Supercapacitor devices in 1M H_2SO_4 electrolyte.

4.8.4 Electrochemical Cycling Stability for the Fabricated Supercapacitor Devices

The device stability was first evaluated for the binary composite devices AC//SnO_2/PANI-30% and AC//BNO/PANI-30% at a current load of 1 A.g^{-1}. The AC//SnO_2/PANI-30% device showed

capacitance retention of 41.54% after 500 cycles, which slightly decreased to 41.17% after 1000 cycles and further declined to 38.7% by the end of 2000 cycles, as shown in Fig. 4.45 (a). Notably, the AC//SnO_2/PANI-30% fabricated supercapacitor demonstrated a remarkable Coulombic efficiency of 99.85% after 2000 cycles, as depicted in Fig. 4.45 (d), indicating that it is a highly efficient device.

Similarly, the AC//BNO/PANI-30% device initially exhibited an improvement in capacitance retention, reaching 99.41% after 200 cycles. However, this value dropped to 91.97% after 500 cycles and eventually decreased to only 52.87% after 5000 cycles, as shown in Fig. 4.45 (b). The significant capacitance loss observed in AC//BNO/PANI-30% between 200 and 5000 cycles is likely due to mechanical stresses leading to electrode cracking, which reduces ion transport and active surface area during prolonged charge/discharge processes. Nevertheless, this device exhibited exceptional Coulombic efficiency, increasing from 97.40% in the initial cycle to 100% after 5000 cycles (Fig. 4.45 (e)), indicating high reversibility of the electrochemical reactions.

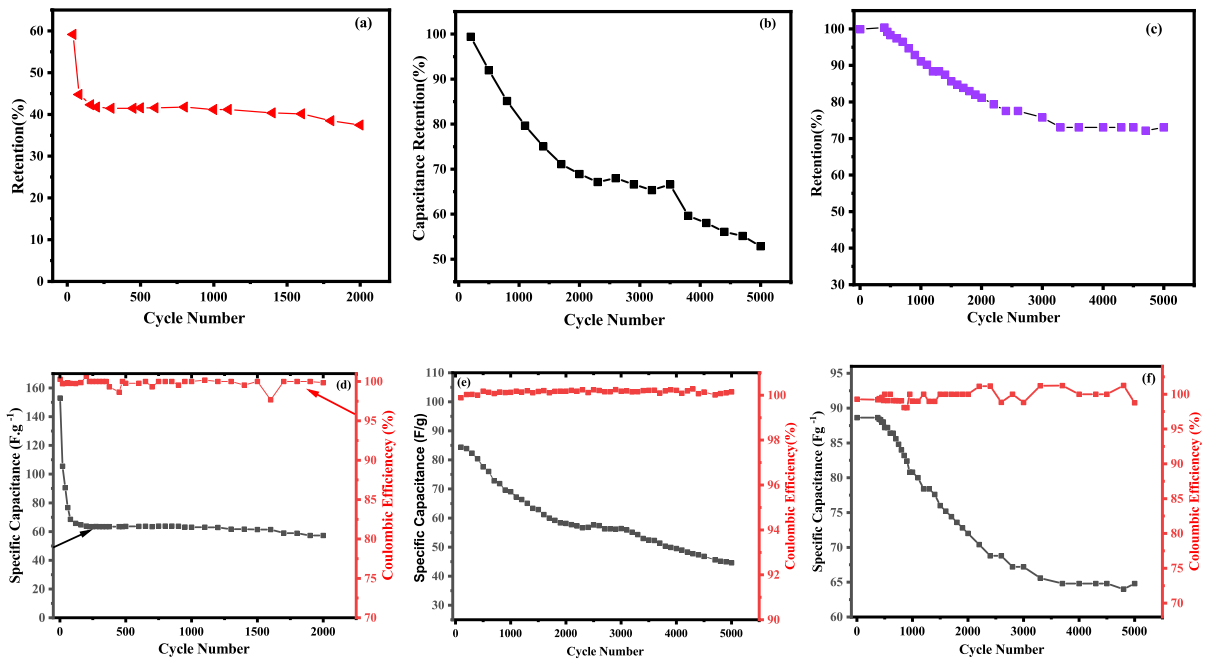

Figure 4.45: Cycling stability of capacitance retention for (a) AC//SnO_2/PANI-30%,(b) AC//BNO/PANI-30% and (c) AC//SnO_2/BNO/PANI; Coulombic efficiency of the devices (d) AC//SnO_2/PANI-30% over 2000 charge-discharge cycles and (e) AC//BNO/PANI-30%, (f) AC//SnO_2/BNO/PANI over 5000 charge-discharge cycles in 1 M H_2SO_4 aqueous electrolyte.

In contrast, the ternary composite device AC//SnO_2/BNO/PANI demonstrated a remarkable improvement in electrochemical stability when cycled at a higher current load of 2 $A.g^{-1}$. This device retained 98.29%, 91.07%, 81.15%, 75.74%, and 73.03% of its initial capacitance after

500, 1000, 2000, 3000, and 5000 cycles, respectively, as shown in Fig. 4.45 (c). Additionally, it maintained a Coulombic efficiency of 98.76% after 5000 cycles, as shown in Fig. 4.45 (f), indicating excellent charge/discharge reversibility. Compared to the binary composites, the ternary device demonstrates superior capacitance retention and long-term cycling stability, which can be attributed to the synergistic effects of the SnO_2, BNO, and PANI components that enhance structural integrity, ion transport, and electro-active surface area during extended cycling.

4.8.5 Electrochemical Impedance Spectroscopy (EIS) Analysis of the Assembled Supercapacitor Devices

The EIS measurements were conducted on AC//SnO_2/PANI-30%, AC//BNO/PANI-30% and AC//SnO_2/BNO/PANI supercapacitor devices (Fig.4.46) to investigate their interfacial electrochemical properties. The impedance spectra were recorded over a wide frequency range (10 mHz to 100 kHz) using the same electrolyte as in previous CV and GCD characterization. The impedance spectra and their corresponding equivalent circuit models were obtained using EC-lab software, as illustrated in Fig. 4.46 (a-c), along with the fitted circuit parameters. The key circuit parameters include solution resistance (R_s), charge transfer resistance (R_{ct}), constant phase elements (Q), and Warburg impedance (W), and they comprehensively describe the devices' electrochemical behavior.

The AC//SnO_2/PANI-30% device, shown in Figure 4.46 (a), exhibited a solution resistance (R_s) of 0.81 Ω, reflecting low internal resistance and efficient ionic conductivity. However, the device presented a relatively high charge transfer resistance (R_{ct}) of 66.49 Ω, indicating a limitation in electron transport at the electrode-electrolyte interface, which could hinder overall performance. The constant phase element (Q = 0.000707 $F.S^{-1}$) suggests surface roughness or inhomogeneity, likely attributed to the structural features of the SnO_2/PANI-30% nanocomposite. The Warburg impedance (W = 19.78 ΩS^{-1}) indicates that ion diffusion also contributes significantly to the total impedance, especially at lower frequencies, potentially affecting rate capability.

For the AC//BNO/PANI-30% device, as depicted in Fig. 4.46 (b), the solution resistance was slightly higher at 3.792 Ω, but still within a favorable range for effective ionic transport. The charge transfer resistance (R_{ct}) was reduced to 44.801 Ω compared to the SnO_2-based system, indicating improved electron transfer kinetics. The lower constant phase element (Q = 0.000155 $F.S^{-1}$) reflects a more uniform electrode surface. However, the Warburg impedance (W = 24.147 $\Omega.S^{-1/2}$) was somewhat greater, suggesting that ion diffusion resistance plays a more prominent role in limiting performance in this configuration.

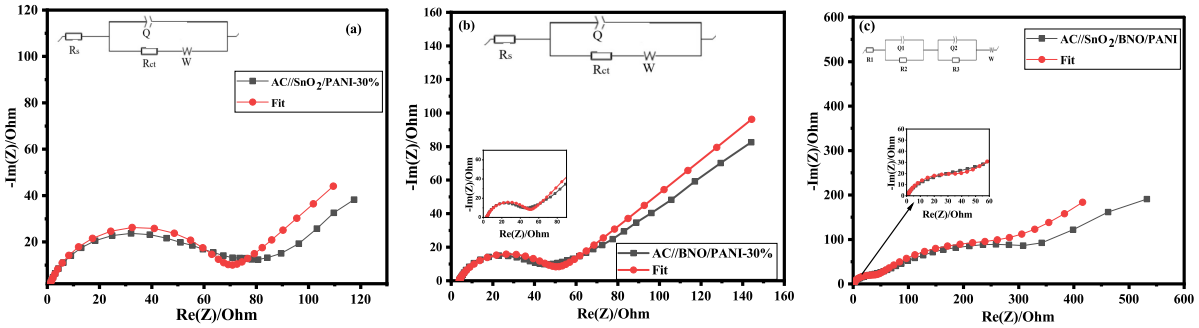

Figure 4.46: Nyquist plots along with the corresponding equivalent circuit models used to fit the EIS data for (a) AC//SnO_2/PANI-30%, (b) AC//BNO/PANI-30% and (c) AC//SnO_2/BNO/PANI devices, in 1 M H_2SO_4 aqueous electrolyte. .

The AC//SnO_2/BNO/PANI ternary device demonstrated the most favorable electrochemical characteristics, as shown in Fig. 4.46 (c). It exhibited the lowest solution resistance (R1 = 0.33 Ω) and a significantly reduced charge transfer resistance (R_2 = 20.17 Ω), indicating enhanced charge transport and interfacial conductivity. The equivalent circuit includes two constant phase elements of Q_1 = 22.12 $\mu F.S^{-1}$ corresponding to double-layer capacitance, and Q_2 = 0.00206 $F.S^{-1}$ representing pseudocapacitive behavior. This dual behavior confirms the presence of a hybrid charge storage mechanism in the ternary composite. Despite the higher Warburg impedance (W = 44.92 $\Omega.S^{-1/2}$, which indicates some ion diffusion limitations, the combined improvements in resistance and capacitance characteristics contribute to the superior electrochemical performance of the ternary system compared to its binary counterparts. These findings demonstrate how ternary composites overcome binary system limitations through synergistic effects. While the binary composites shows inherent conductivity constraints (evident in its single Q value and high R_{ct}), the ternary system's dual Q components and lower R_{ct} enable superior charge transfer and energy storage. The results emphasize that strategic material combinations in ternary systems can significantly enhance supercapacitor performance. The distinct Q_1 and Q_2 values in the ternary system particularly highlight its ability to combine both double-layer and pseudocapacitive storage mechanisms effectively.

CHAPTER 5

CONCLUSIONS AND RECOMMENDATIONS

5.1 Conclusions

In conclusion, this study demonstrates that combining green synthesis of SnO_2 and BNO nanoparticles with the strategic design of SnO_2/$Bi_5Nb_3O_{15}$/PANI nanocomposites offers an effective approach for developing high-performance supercapacitor electrode. Incorporating $Bi_5Nb_3O_{15}$ and the conducting polymer PANI effectively addresses the inherent limitations of SnO_2, such as poor conductivity and limited ion transport, thereby enhancing its electrochemical functionality. This study confirms the strong influence of PANI on improving the charge-storage behavior of both SnO_2 and $Bi_5Nb_3O_{15}$ nanoparticles. The SnO_2/PANI nanocomposites, particularly SnO_2/PANI-30%, demonstrated a remarkable increase in specific capacitance,achieving 338 $F.g^{-1}$ at 0.1 $A.g^{-1}$, along with good cycling stability and high Coulombic efficiency. Likewise, the $Bi_5Nb_3O_{15}$/PANI-30% nanocomposite showed significant enhancement over pristine $Bi_5Nb_3O_{15}$, achieving a good capacitance retention and stable long-term performance.

The ternary SnO_2/$Bi_5Nb_3O_{15}$/PANI nanocomposite delivered the greatest overall electrochemical improvement, reaching a specific capacitance of 424 $F.g^{-1}$ at 5 mVs^{-1} and maintaining a remarkable Coulombic efficiency after 5000 cycles, highlighting the strong synergistic interaction among the three components.The integration of PANI with SnO_2 and $Bi_5Nb_3O_{15}$ substantially improved conductivity, ion diffusion, and redox activity, resulting in superior electrochemical behavior across all composite systems. These enhancements demonstrate the effectiveness of polymer-oxide hybridization in producing efficient and high-performing electrode materials suitable for supercapcitor applications. The consistent improvements in specific capacitance, specific energy,and power densities, and cycling stability across all composite types confirm the promising potential of these materials for practical supercapacitor applications.

This improved electrochemical response was further validated by the performance of the asymmetric supercapacitor (ASC) devices assembled with activated carbon (AC) as the negative electrode. The AC//SnO_2/BNO/PANI device exhibited superior specific energy and power densities, achieving 67.27 $Wh\,kg^{-1}$ at 0.2 $A\,g^{-1}$ and a maximum specific power density of 5600 $W\,kg^{-1}$, outperforming AC//SnO_2/PANI-30% and AC//BNO/PANI-30%, which showed lower values across comparable current densities. Moreover, this device displayed excellent cycling stability, with Coulombic efficiency exceeding 98% and capacitance retention up to 73% after 5000

cycles. These results indicate that the ternary SnO_2/BNO/PANI nanocomposite provides a synergistic combination of high energy, high power, and long-term stability, making it a highly promising electrode material for advanced supercapacitor applications.

5.2 Recommendations

For future research, it is recommended to further optimize the synthesis of the ternary nanocomposite SnO_2/BNO/PANI to enhance conductivity, structural uniformity, and long-term electrochemical stability, while exploring alternative electrolytes, electrode configurations, and active material loadings to improve device performance. It is also strongly recommended to continue with the facile synthesis and further exploration of SnO_2/BNO/PANI nanocomposites for photocatalytic applications. Each constituent of the composite contributes distinct advantages: SnO_2 offers excellent chemical stability, BNO provides a layered perovskite structure with a suitable band gap and ferroelectric properties that enhance charge separation, and PANI introduces outstanding electrical conductivity and environmental resilience. The integration of these components is expected to generate a synergistic effect, improving overall photocatalytic performance through efficient charge separation and reduced recombination of photogenerated electron–hole pairs. It is therefore advisable to evaluate its photocatalytic activity under various illumination conditions and to assess its long-term structural stability and functional durability, ensuring its practical applicability and reliability for sustainable environmental remediation technologies.

List of Publications

Throughout my Ph.D. studies, I have authored two articles in reputable journals, which are listed below.

A. Published Articles

1. **Niguss Awoke**, Gashaw Beyene, Fekadu Tolassa, Mesfin Asfaw, Paul M. Ejikeme, Assumpta C. Nwanya, and Fabian I. Ezem: Facile Synthesis and Characterizations of SnO_2/PAN Nanocomposites for High-Performance Supercapacitors, **ChemistrySelect**, 2025. 10(23): p.e01289 .

2. **Niguss Awoke**, Gashaw Beyene, Fekadu Tolassa, Mesfin Asfaw, Paul M. Ejikeme, Assumpta C. Nwanya, and Fabian I. Ezem: Facile synthesis and characterizations of $Bi_5Nb_3O_{15}$/PANI nanocomposite for supercapacitor application, **Applied Physics A**, 2025. 131(5): p.367.

B. Manuscript under Review

1. Niguss Awoke, Gashaw Beyene, Fekadu Tolassa, Mesfin Asfaw, Paul M. Ejikeme, Assumpta C. Nwanya, and Fabian I. Ezem Gelanu: Facile Synthesis and Electrochemical Characterization of Novel SnO_2/$Bi_5Nb_3O_{15}$/PANI Ternary Nanocomposite as Electrodes for Supercapacitor Applications.

Awards

I have participated in international conferences and received certificates for each as listed below:

1. Certificate of Attendance for the successful completion of the 2024 Hands-On Training/-Workshop titled: **"Recent Advances in Nanotechnology and Applications"**, held from 22^{nd}–28^{th} July 2024 at the University of Nigeria, Nsukka.

2. Certificate of Presentation from the University of Nigeria for presenting the paper titled: **"Facile synthesis and characterization of Bi_5NbO_{15}/PANI nanocomposite for supercapacitor applications"** during the **6^{th} Biennial Conference/Workshop on Applications of Nanotechnology to Energy, Environment, Agriculture, and Health (Hybrid International Conference 2025)**, held from 14^{th}–19^{th} July 2025.

References

Abdelkader, E., Nadjia, L., & Ahmed, B. (2015). Preparation and characterization of novel cubi2o4/sno2 p–n heterojunction with enhanced photocatalytic performance under uva light irradiation. *Journal of King Saud University-Science*, *27*(1), 76–91.

Abdel Maksoud, M., Fahim, R. A., Shalan, A. E., Abd Elkodous, M., Olojede, S., Osman, A. I., ... others (2021). Advanced materials and technologies for supercapacitors used in energy conversion and storage: a review. *Environmental Chemistry Letters*, *19*(1), 375–439.

Abdolahi, A., Hamzah, E., Ibrahim, Z., & Hashim, S. (2012). Synthesis of uniform polyaniline nanofibers through interfacial polymerization. *Materials*, *5*(8), 1487–1494.

AbdulAlmohsin, S., Li, Z., Mohammed, M., Wu, K., & Cui, J. (2012). Electrodeposited polyaniline/multi-walled carbon nanotube composites for solar cell applications. *Synthetic Metals*, *162*(11-12), 931–935.

Abernathy, H., Gemmen, R., Gerdes, K., Koslowske, M., & Tao, T. (2011). Basic properties of a liquid tin anode solid oxide fuel cell. *Journal of Power Sources*, *196*(10), 4564–4572.

ABID, M. A. M., Radzi, M. I., Mupit, M., Osman, H., Munawar, R. F., Samat, K. F., ... Islam, M. R. (2020). Cyclic voltammetry and galvanostatic charge-discharge analyses of polyaniline/graphene oxide nanocomposite based supercapacitor. *Malaysian Journal on Composites Science and Manufacturing*, *3*(1), 14–26.

Ahmed, F., Kumar, S., Shaalan, N. M., Arshi, N., Dalela, S., & Chae, K. H. (2023). Fabrication of high-performance asymmetric supercapacitors using rice husk-activated carbon and mnfe2o4 nanostructures. *Nanomaterials*, *13*(12), 1870.

Allagui, A., Freeborn, T. J., Elwakil, A. S., & Maundy, B. J. (2016). Reevaluation of performance of electric double-layer capacitors from constant-current charge/discharge and cyclic voltammetry. *Scientific reports*, *6*(1), 38568.

Al-Maswari, B. M., Ahmed, J., Alzaqri, N., Ahamad, T., Mao, Y., Hezam, A., & Venkatesha, B. (2021). Synthesis of perovskite bismuth ferrite embedded nitrogen-doped carbon (bifeo3-nc) nanocomposite for energy storage application. *Journal of Energy Storage*, *44*, 103515.

Alonzo, S. M. M., Bentley, J., Desai, S., & Bastakoti, B. P. (2023). Hydrothermal synthesis of hierarchical microstructure tungsten oxide/carbon nanocomposite for supercapacitor application. *Scientific Reports*, *13*(1), 21732.

Alshoaibi, A. (2025). Phase evolution of electrodeposited manganese oxidefor supercapacitor applications. In *248th ecs meeting (october 12-16, 2025)*.

Amaechi, I. C., Nwanya, A. C., Ekwealor, A. B., Asogwa, P. U., Osuji, R. U., Maaza, M., & Ezema, F. I. (2015). Electronic thermal conductivity, thermoelectric properties and supercapacitive behaviour of conjugated polymer nanocomposite (polyaniline-wo3) thin film. *The European Physical Journal Applied Physics*, *69*(3), 30901.

An, C., Zhang, Y., Guo, H., & Wang, Y. (2019). Metal oxide-based supercapacitors: progress and prospectives. *Nanoscale Advances*, *1*(12), 4644–4658.

Asaithambi, S., Sakthivel, P., Karuppaiah, M., Yuvakkumar, R., Balamurugan, K., Ahamad, T., ... Ravi, G. (2021). Preparation of fe-sno2@ ceo2 nanocomposite electrode for asymmetric supercapacitor device performance analysis. *Journal of Energy Storage*, *36*, 102402.

Asen, P., Haghighi, M., Shahrokhian, S., & Taghavinia, N. (2019). One step synthesis of sns2-sno2 nano-heterostructured as an electrode material for supercapacitor applications. *Journal of Alloys and Compounds*, *782*, 38–50.

Atay, F., & Akyuz, I. (2022). Structural, optical, surface, and photocatalytic properties of sno2 films produced by ultrasonic spray pyrolysis. *Journal of Sol-Gel Science and Technology*, *102*(2), 303–312.

Aziz, M., Abbas, S. S., & Baharom, W. R. W. (2013). Size-controlled synthesis of sno2 nanoparticles by sol–gel method. *Materials Letters*, *91*, 31–34.

Bahrulolum, H., Nooraei, S., Javanshir, N., Tarrahimofrad, H., Mirbagheri, V. S., Easton, A. J., & Ahmadian, G. (2021). Green synthesis of metal nanoparticles using microorganisms and their application in the agrifood sector. *Journal of Nanobiotechnology*, *19*(1), 86.

Bhardwaj, N., & Mohapatra, S. (2016). Structural, optical and gas sensing properties of ag-sno2 plasmonic nanocomposite thin films. *Ceramics International*, *42*(15), 17237–17242.

Bresser, D., Buchholz, D., Moretti, A., Varzi, A., & Passerini, S. (2018). Alternative binders for sustainable electrochemical energy storage–the transition to aqueous electrode processing and bio-derived polymers. *Energy & Environmental Science*, *11*(11), 3096–3127.

Chen, D., Li, J., & Wu, Q. (2019). Review of v2o5-based nanomaterials as electrode for supercapacitor. *Journal of Nanoparticle Research*, *21*(9), 201.

Chen, G. Z. (2017). Supercapacitor and supercapattery as emerging electrochemical energy stores. *International Materials Reviews*, *62*(4), 173–202.

Chen, S.-M., Ramachandran, R., Mani, V., & Saraswathi, R. (2014). Recent advancements in electrode materials for the highperformance electrochemical supercapacitors: a review. *International Journal of Electrochemical Science*, *9*(8), 4072–4085.

Cheng, Q., Tang, J., Ma, J., Zhang, H., Shinya, N., & Qin, L.-C. (2011). Graphene and nanostructured mno2 composite electrodes for supercapacitors. *Carbon*, *49*(9), 2917–2925.

Chetri, P., & Choudhury, A. (2013). Investigation of optical properties of sno2 nanoparticles. *Physica E: Low-dimensional Systems and Nanostructures*, *47*, 257–263.

Chitrada, K. C., & Raja, K. S. (2014). Nanoporous anodic bismuth oxide for electrochemical energy storage. *ECS Transactions*, *61*(18), 55.

Chodankar, N. R., Pham, H. D., Nanjundan, A. K., Fernando, J. F., Jayaramulu, K., Golberg, D., ... Dubal, D. P. (2020). True meaning of pseudocapacitors and their performance metrics: asymmetric versus hybrid supercapacitors. *Small*, *16*(37), 2002806.

Choi, H., & Yoon, H. (2015). Nanostructured electrode materials for electrochemical capacitor applications. *Nanomaterials*, *5*(2), 906–936.

Cholewinski, A., Si, P., Uceda, M., Pope, M., & Zhao, B. (2021). Polymer binders: Characterization and development toward aqueous electrode fabrication for sustainability. *Polymers*, *13*(4), 631.

Choudhary, N., Li, C., Chung, H.-S., Moore, J., Thomas, J., & Jung, Y. (2016). High-performance one-body core/shell nanowire supercapacitor enabled by conformal growth of capacitive 2d ws2 layers. *ACS nano*, *10*(12), 10726–10735.

Ciszewski, M., Mianowski, A., Szatkowski, P., Nawrat, G., & Adamek, J. (2015). Reduced graphene oxide–bismuth oxide composite as electrode material for supercapacitors. *Ionics*, *21*(2), 557–563.

Czagany, M., Hompoth, S., Keshri, A. K., Pandit, N., Galambos, I., Gacsi, Z., & Baumli, P. (2024). Supercapacitors: An efficient way for energy storage application. *Materials*, *17*(3), 702.

Dadkhah, M., & Salavati-Niasari, M. (2014). Dye-sensitized solar cells based on tin dioxide nanoparticles prepared by a facile hydrothermal method. *Materials science in semiconductor processing*, *20*, 41–48.

Danamah, H. M., Raut, S. D., Shaikh, Z. A., & Mane, R. S. (2023). Chemical synthesis of bismuth oxide and its ionic conversion to bismuth sulphide for enhanced electrochemical supercapacitor energy storage performance. *Journal of The Electrochemical Society*, *169*(12), 120537.

Davies, A., & Yu, A. (2011). Material advancements in supercapacitors: from activated carbon to carbon nanotube and graphene. *The Canadian Journal of Chemical Engineering*, *89*(6), 1342–1357.

Deepi, A., Srikesh, G., & Nesaraj, A. S. (2018). Electrochemical performance of bi2o3 decorated graphene nano composites for supercapacitor applications. *Nano-Structures & Nano-Objects*, *15*, 10–16.

Deng, D., & Lee, J. Y. (2008). Hollow core–shell mesospheres of crystalline sno2 nanoparticle aggregates for high capacity li+ ion storage. *Chemistry of Materials*, *20*(5), 1841–1846.

De Santillana, G. (1965). Alessandro volta. *Scientific American*, *212*(1), 82–91.

Du, D., Wu, X., Li, S., Zhang, Y., Xing, W., Li, L., ... Yan, Z. (2017). Remarkable supercapacitor performance of petal-like ldhs vertically grown on graphene/polypyrrole nanoflakes. *Journal of Materials Chemistry A*, *5*(19), 8964–8971.

Dubal, D. P., Chodankar, N. R., Gomez-Romero, P., & Kim, D.-H. (2017). Fundamentals of binary metal oxide–based supercapacitors. In *Metal oxides in supercapacitors* (pp. 79–98). Elsevier.

Dunn, B., Kamath, H., & Tarascon, J.-M. (2011). Electrical energy storage for the grid: a battery of choices. *Science*, *334*(6058), 928–935.

Dupont, M. F., & Donne, S. W. (2016). Charge storage mechanisms in electrochemical capacitors: Effects of electrode properties on performance. *Journal of Power Sources*, *326*, 613–623.

Eftekhari, A., Li, L., & Yang, Y. (2017). Polyaniline supercapacitors. *Journal of Power Sources*, *347*, 86–107.

Elgrishi, N., Rountree, K. J., McCarthy, B. D., Rountree, E. S., Eisenhart, T. T., & Dempsey, J. L. (2018). A practical beginner's guide to cyclic voltammetry. *Journal of chemical education*, *95*(2), 197–206.

Elmanfaloty, R. A., Shokry, E., Abou-bakr, E., Ebrahim, S., & Elshaer, A. (2024). Electrochemical measurements, structural and morphological studies of electrodeposited polypyrrole supercapacitor electrode. *Alexandria Engineering Journal*, *107*, 867–877.

Endo, M., Takeda, T., Kim, Y., Koshiba, K., & Ishii, K. (2001). High power electric double layer capacitor (edlc's); from operating principle to pore size control in advanced activated carbons. *Carbon letters*, *1*(3_4), 117–128.

Fatimah, I., Purwiandono, G., Sahroni, I., Sagadevan, S., & Doong, R.-a. (2022). Flower-like hierarchical sn3o4/montmorillonite nanostructure for the enhanced microwave-induced degradation of rhodamine b. *Advanced Powder Technology*, *33*(6), 103623.

Gao, M., Wang, W.-K., Rong, Q., Jiang, J., Zhang, Y.-J., & Yu, H.-Q. (2018). Porous zno-coated co3o4 nanorod as a high-energy-density supercapacitor material. *ACS applied materials & interfaces*, *10*(27), 23163–23173.

Garima, Choudhary, A., Kumar, M., Sharma, A., Kumar, R., & Sheel, V. (2025). Enhanced supercapacitor performance using graphene based bismuth–niobium nanocomposites: A review. *Materials Chemistry and Physics*, *346*, 131311. Retrieved from https://www.sciencedirect.com/science/article/pii/S0254058425009575 doi: https://doi.org/10.1016/j.matchemphys.2025.131311

Gholivand, M. B., Heydari, H., Abdolmaleki, A., & Hosseini, H. (2015). Nanostructured cuo/pani composite as supercapacitor electrode material. *Materials Science in Semiconductor Processing*, *30*, 157–161.

Ginley, D., Green, M. A., & Collins, R. (2008). Solar energy conversion toward 1 terawatt. *MRS bulletin*, *33*(4), 355–364.

Gospodinova, N., & Terlemezyan, L. (1998). Conducting polymers prepared by oxidative polymerization: polyaniline. *Progress in polymer science*, *23*(8), 1443–1484.

Gote, G. H., Pathak, M., More, M. A., Late, D. J., & Rout, C. S. (2019). Development of pristine and au-decorated bi 2 o 3/bi 2 wo 6 nanocomposites for supercapacitor electrodes. *RSC advances*, *9*(56), 32573–32580.

Gu, D., Ding, C., Qin, Y., Jiang, H., Wang, L., & Shen, L. (2017). Behavior of electrical charge storage/release in polyaniline electrodes of symmetric supercapacitor. *Electrochimica Acta*, *245*, 146–155.

Guan, L., Guo, L., Yao, H., Cai, J., Dong, X., Wang, R., ... others (2025). Redox additive electrolytes for supercapacitors: A mini-review on recent developments and future directions. *Molecules*, *30*(8), 1764.

Guo, Y., Chen, L., Ma, F., Zhang, S., Yang, Y., Yuan, X., & Guo, Y. (2011). Efficient degradation of tetrabromobisphenol a by heterostructured ag/bi5nb3o15 material under the simulated sunlight irradiation. *Journal of Hazardous Materials*, *189*(1-2), 614–618.

Gurunathan, K., & Maruthamuthu, P. (1998). Bi5nb3o15 as a photocatalyst: photocatalytic and photoelectrochemical studies. *Journal of Solid State Electrochemistry*, *2*(3), 176–180.

Hong, X., Liu, Y., Li, Y., Wang, X., Fu, J., & Wang, X. (2020). Application progress of polyaniline, polypyrrole and polythiophene in lithium-sulfur batteries. *Polymers*, *12*(2), 331.

Huang, H., Zhou, C., Jiao, X., Yuan, H., Zhao, J., He, C., ... Steele, J. A. (2019). Subsurface defect engineering in single-unit-cell bi2wo6 monolayers boosts solar-driven photocatalytic performance. *Acs Catalysis*, *10*(2), 1439–1443.

Huang, J. (2006). Syntheses and applications of conducting polymer polyaniline nanofibers. *Pure and applied chemistry*, *78*(1), 15–27.

Imran, M., Waris, M. H., Khan, R., Afzal, A. M., Iqbal, M. W., Mumtaz, M. A., ... Hussain, Z. (2023). High-performance energy storage hybrid supercapacitor device based on nicos@ cnt@ graphene composite electrode material. *Physica Scripta*, *98*(11), 115981.

Iravani, S. (2011). Green synthesis of metal nanoparticles using plants. *Green chemistry*, *13*(10), 2638–2650.

Iro, Z. S., Subramani, C., & Dash, S. (2016). A brief review on electrode materials for supercapacitor. *International Journal of Electrochemical Science*, *11*(12), 10628–10643.

Isacfranklin, M., Deepika, C., Ravi, G., Yuvakkumar, R., Velauthapillai, D., & Saravanakumar, B. (2020). Nickel, bismuth, and cobalt vanadium oxides for supercapacitor applications. *Ceramics International*, *46*(18), 28206–28210.

Ismail, Vigneshwaran, J., Arunbalaji, S., Mani, D., Arivanandhan, M., Jose, S. P., & Jayavel, R. (2020). Antimonene nanosheets with enhanced electrochemical performance for energy storage applications. *Dalton Transactions*, *49*(39), 13717–13725.

Ismail, K. B. M., Kumar, M. A., Jayavel, R., Arivanandhan, M., & Ismail, M. A. M. (2023). Enhanced electrochemical performance of the mos 2/bi 2 s 3 nanocomposite-based electrode

material prepared by a hydrothermal method for supercapacitor applications. *RSC advances*, *13*(35), 24272–24285.

Jacob, R., Nair, H. G., & Isac, J. (2015). Structural and morphological studies of nano-crystalline ceramic basr 0.9 fe 0.1 tio 4. *international Letters of chemistry, physics and Astronomy*, *41*.

Jadhav, V. V., Zate, M. K., Liu, S., Naushad, M., Mane, R. S., Hui, K., & Han, S.-H. (2016). Mixed-phase bismuth ferrite nanoflake electrodes for supercapacitor application. *Applied nanoscience*, *6*(4), 511–519.

Jalal, N. I., Ibrahim, R. I., & Oudah, M. K. (2021). A review on supercapacitors: Types and components. In *Journal of physics: Conference series* (Vol. 1973, p. 012015).

Jariwala, S., Desai, Y., & Gupta, R. K. (2023). Polymer-based nanocomposites for supercapacitors. In *Recent advancements in polymeric materials for electrochemical energy storage* (pp. 93–111). Springer.

Jayakumar, S., Santhosh, P. C., Mohideen, M. M., & Radhamani, A. (2024). A comprehensive review of metal oxides (ruo2, co3o4, mno2 and nio) for supercapacitor applications and global market trends. *Journal of Alloys and Compounds*, *976*, 173170.

Jayalakshmi, M., Rao, M. M., Venugopal, N., & Kim, K.-B. (2007). Hydrothermal synthesis of sno2–v2o5 mixed oxide and electrochemical screening of carbon nano-tubes (cnt), v2o5, v2o5–cnt, and sno2–v2o5–cnt electrodes for supercapacitor applications. *Journal of Power Sources*, *166*(2), 578–583.

Jia, B., & Zhang, W. (2016). Preparation and application of electrodes in capacitive deionization (cdi): a state-of-art review. *Nanoscale research letters*, *11*(1), 64.

Joshi, N. C., Rawat, B., Bisht, H., Gajraj, V., Kumar, N., Chetana, S., & Gururani, P. (2022). Synthesis and supercapacitive behaviour of sno2/r-go nanocomposite. *Synthetic Metals*, *289*, 117132.

Kaky, K. M., Sayyed, M., Hamad, M. K., Biradar, S., Mhareb, M., Altimari, U., & Taki, M. M. (2024). Bismuth oxide effects on optical, structural, mechanical, and radiation shielding features of borosilicate glasses. *Optical Materials*, *155*, 115853.

Karadurmus, L., Kurbanoglu, S., Uslu, B., & Ozkan, S. A. (2022). An efficient, simultaneous electrochemical assay of rosuvastatin and ezetimibe from human urine and serum samples. *Methods and Protocols*, *5*(6), 90.

Karden, E., Ploumen, S., Fricke, B., Miller, T., & Snyder, K. (2007). Energy storage devices for future hybrid electric vehicles. *Journal of Power Sources*, *168*(1), 2–11.

Karmakar, S. (2024). Impedance spectroscopy for electroceramics and electrochemical system. *arXiv preprint arXiv:2406.15467*.

Karpuraranjith, M., Thamb, T., & M, J. (2016). Twist fibrous structure of cs–sno 2–pani ternary hybrid composite for electrochemical capacitance performance. *Rsc Advances*, *6*(46), 40567–40576.

Karthikeyan, S., Narenthiran, B., Sivanantham, A., Bhatlu, L. D., & Maridurai, T. (2021). Supercapacitor: Evolution and review. *Materials Today: Proceedings*, *46*, 3984–3988.

Khan, F., Shahid, A., Zhu, H., Wang, N., Javed, M. R., Ahmad, N., ... Mehmood, M. A. (2022). Prospects of algae-based green synthesis of nanoparticles for environmental applications. *Chemosphere*, *293*, 133571.

Kim, B. K., Sy, S., Yu, A., & Zhang, J. (2015). Electrochemical supercapacitors for energy storage and conversion. *Handbook of clean energy systems*, 1–25.

Konikkara, N., & Kennedy, L. J. (2017). Electrochemical properties of solid leather wastes based supercapacitor electrodes using h2so4 electrolyte. *Materials Letters*, *205*, 56–61.

Koventhan, C., & Lo, A.-Y. (2024). Morphology engineering of novel mnmoo4@ nimoo4 core–shell nanostructure as an electrode material for asymmetric supercapacitor device. *Chemical Engineering Journal*, *485*, 149950.

Kumar, G., Reddy, S., Maseed, H., & Reddy, N. (2020). *Facile hydrothermal synthesis of ternary ceo2–sno2/rgo nanocomposite for supercapacitor application. funct mater lett 13: 1–7.*

Kumar, M. S., Das, P., Yasoda, K. Y., Kothurkar, N. K., Malik, S., & Batabyal, S. K. (2020). Fabrication of organic nanocomposite of polyaniline for enhanced electrochemical performance. *Journal of Energy Storage*, *31*, 101700.

Kumar, R., Gokul, S., Ran, F., Sambasivam, S., Alrashidi, K. A., & Thangappan, R. (2024). Green synthesis of g-c3n4 decorated with sno2 nanocomposites using a novel ananas comosus crown extract for boosted performance of asymmetric supercapacitors. *Journal of Energy Storage*, *98*, 113231.

Kuo, S.-L., Lee, J.-F., & Wu, N.-L. (2006). Study on pseudocapacitance mechanism of aqueous mnfe2o4 supercapacitor. *Journal of the Electrochemical Society*, *154*(1), A34.

Laheäär, A., Przygocki, P., Abbas, Q., & Béguin, F. (2015). Appropriate methods for evaluating the efficiency and capacitive behavior of different types of supercapacitors. *Electrochemistry Communications*, *60*, 21–25.

Lakra, R., Kumar, R., Thatoi, D., Soam, A., et al. (2023). Synthesis of tio2 nanoparticles as electrodes for supercapacitor. *Materials Today: Proceedings*, *74*, 863–866.

Laska, J., Widlarz, J., & Woźny, E. (2002). Precipitation polymerization of aniline in the presence of water-soluble organic acids. *Journal of Polymer Science Part A: Polymer Chemistry*, *40*(21), 3562–3569.

Lee, K. T., Lidie, A. A., Jeon, S. Y., Hitz, G. T., Song, S. J., & Wachsman, E. D. (2013). Highly functional nano-scale stabilized bismuth oxides via reverse strike co-precipitation for solid oxide fuel cells. *Journal of Materials Chemistry A*, *1*(20), 6199–6207.

Lei, J., & Chen, X. (2015). Ruo2/mno2 composite materials for high-performance supercapacitor electrodes. *Journal of Semiconductors*, *36*(8), 083006.

Le Minh, H. (2013). *Electrodéposition de film de sno2 nanostructurés pour la détection électrochimique sans marquage d'adn*. Unpublished doctoral dissertation, Grenoble.

Li, Zhang, N., Wu, Y.-R., Lai, Q.-Z., Zhu, Y.-R., Zhang, J.-H., … Yi, T.-F. (2022). Interconnected bi5nb3o15@ cnts network as high-performance anode materials of li-ion battery. *Rare Metals*, *41*(10), 3401–3411.

Li, B., Zhou, Q., Peng, S., & Liao, Y. (2020). Recent advances of sno2-based sensors for detecting volatile organic compounds. *Frontiers in chemistry*, *8*, 321.

Li, Y., Zheng, R., Yu, H., Cheng, X., Liu, T., Peng, N., … Shu, J. (2019). Fabrication of one-dimensional architecture bi5nb3o15 nanowires by electrospinning for lithium-ion batteries with enhanced electrochemical performance. *Electrochimica Acta*, *299*, 894–901.

Li, Y., Zheng, R., Yu, H., Cheng, X., Zhu, H., Bai, Y., … Shu, J. (2018). Carbon-coated bi5nb3o15 as anode material in rechargeable batteries for enhanced lithium storage. *Ceramics International*, *44*(10), 11505–11511.

Liang, R., Du, Y., Xiao, P., Cheng, J., Yuan, S., Chen, Y., … Chen, J. (2021). Transition metal oxide electrode materials for supercapacitors: a review of recent developments. *Nanomaterials*, *11*(5), 1248.

Lim, S., Huang, N., & Lim, H. (2013). Solvothermal synthesis of sno2/graphene nanocomposites for supercapacitor application. *Ceramics International*, *39*(6), 6647–6655.

Liu, L., Zhang, X., Liu, Y., & Gong, X. (2025). Electrochemical energy storage devices-batteries, supercapacitors, and battery–supercapacitor hybrid devices. *ACS Applied Electronic Materials*, *7*(6), 2233–2270.

Liu, Y., Koep, E., & Liu, M. (2005). A highly sensitive and fast-responding sno2 sensor fabricated by combustion chemical vapor deposition. *Chemistry of materials*, *17*(15), 3997–4000.

Lokhande, P. E., Chavan, U. S., & Pandey, A. (2020). Materials and fabrication methods for electrochemical supercapacitors: overview. *Electrochemical Energy Reviews*, *3*(1), 155–186.

Lopa, N. S., Akbari, M. K., Wu, D., Verpoort, F., & Zhuiykov, S. (2023). Two-dimensional sno2-zno nanohybrid electrode fabricated via atomic layer deposition for electrochemical supercapacitors. *Energy & Fuels*, *37*(4), 3142–3151.

Magar, H. S., Hassan, R. Y., & Mulchandani, A. (2021). Electrochemical impedance spectroscopy (eis): Principles, construction, and biosensing applications. *Sensors*, *21*(19), 6578.

Maliszewska, I., Juraszek, A., & Bielska, K. (2014). Green synthesis and characterization of silver nanoparticles using ascomycota fungi penicillium nalgiovense aj12. *Journal of Cluster Science*, *25*(4), 989–1004.

Manikandan, E., Kannan, J., Devabharathi, V., Pushpa, S., & Mala, N. A. (2023). Structural, optical, photoluminescence, magnetic and electrochemical supercapacitor application of tin oxide nanoparticles. *Materials Today: Proceedings*, *80*, 1591–1598.

Matinise, N., Botha, N., Madiba, I., & Maaza, M. (2023). Mixed-phase bismuth ferrite oxide (bifeo3) nanocomposites by green approach as an efficient electrode material for supercapacitor application. *MRS Advances*, *8*(12), 703–707.

Meher, S. K., & Rao, G. R. (2011). Ultralayered co3o4 for high-performance supercapacitor applications. *The Journal of Physical Chemistry C*, *115*(31), 15646–15654.

Mehra, P., Saxena, S., & Bhullar, S. (2024). A comprehensive analysis of supercapacitors and their equivalent circuits—a review. *World Electric Vehicle Journal*, *15*(8), 332.

Meng, Q., Cai, K., Chen, Y., & Chen, L. (2017). Research progress on conducting polymer based supercapacitor electrode materials. *Nano Energy*, *36*, 268–285.

Mirmohseni, A., Dorraji, M. S., & Hosseini, M. (2012). Influence of metal oxide nanoparticles on pseudocapacitive behavior of wet-spun polyaniline-multiwall carbon nanotube fibers. *Electrochimica Acta*, *70*, 182–192.

Mohamed, M. A., Jaafar, J., Ismail, A., Othman, M., & Rahman, M. (2017). Fourier transform infrared (ftir) spectroscopy. In *Membrane characterization* (pp. 3–29). Elsevier.

Mohammed, A., & Abdullah, A. (2018). Scanning electron microscopy (sem): A review. In *Proceedings of the 2018 international conference on hydraulics and pneumatics—hervex, băile govora, romania* (Vol. 2018, pp. 7–9).

Momma, T., Liu, X., Osaka, T., Ushio, Y., & Sawada, Y. (1996). Electrochemical modification of active carbon fiber electrode and its application to double-layer capacitor. *Journal of power sources*, *60*(2), 249–253.

Moniruzzaman, M., Akib, A., Shakil, R., Khatun, S., Roy, C. K., & Chowdury, A.-N. (2022). Influence of binder in the fabrication of ac-based high-performance electrochemical supercapacitors. *ECS Transactions*, *107*(1), 18357.

Mujawar, S. H., Ambade, S. B., Battumur, T., Ambade, R. B., & Lee, S.-H. (2011). Electropolymerization of polyaniline on titanium oxide nanotubes for supercapacitor application. *Electrochimica Acta*, *56*(12), 4462–4466.

Nasir, F., & Mohammad, M. A. (2020). Investigation of device dimensions on electric double layer microsupercapacitor performance and operating mechanism. *IEEE Access*, *8*, 28367–28374.

Nath, A. R., Garlapati, K. K., Yatheendran, A., & Sandhyarani, N. (2022). Asymmetrical supercapacitor fabricated using sodium nickel phosphate and transition metal-carbon nitride nanocomposite as electrodes. *Energy & Fuels*, *36*(22), 13882–13893.

Navale, Y., Navale, S., Chougule, M., Ingole, S., Stadler, F., Mane, R. S., ... Patil, V. (2017). Electrochemical synthesis and potential electrochemical energy storage performance of nodule-type polyaniline. *Journal of Colloid and Interface Science*, *487*, 458–464.

Ndipingwi, M. M., Ikpo, C. O., Hlongwa, N. W., Myalo, Z., Ross, N., Masikini, M., ... Iwuoha, E. I. (2018). Orthorhombic nanostructured li2mnsio4/al2o3 supercapattery electrode with efficient lithium-ion migratory pathway. *Batteries & Supercaps*, *1*(6), 223–235.

Ndipingwi, M. M., Ikpo, C. O., Nwanya, A. C., Januarie, K. C., Ramoroka, M. E., Uhuo, O. V., ... Iwuoha, E. I. (2022). Engineering the chemical environment of lithium manganese silicate by mn ion substitution to boost the charge storage capacity for application in high efficiency supercapattery. *Electrochimica Acta*, *414*, 140180.

Nguyen-Dinh, M.-T., Bui, T. S., Bansal, P., Jourshabani, M., & Lee, B.-K. (2021). Photocatalytic and photo-electrochemical behavior of novel sno2-modified-g-c3n4 for complete elimination of tetracycline under visible-light irradiation: slurry and fixed-bed approach. *Separation and Purification Technology*, *267*, 118607.

Nie, G., Lu, X., Lei, J., Yang, L., & Wang, C. (2015). Facile and controlled synthesis of bismuth sulfide nanorods-reduced graphene oxide composites with enhanced supercapacitor performance. *Electrochimica Acta*, *154*, 24–30.

Niu, Z., Zhang, Y., Zhang, Y., Lu, X., & Liu, J. (2020). Enhanced electrochemical performance of three-dimensional graphene/carbon nanotube composite for supercapacitor application. *Journal of Alloys and Compounds*, *820*, 153114.

Nwanya, A. C., Jafta, C. J., Ejikeme, P. M., Ugwuoke, P. E., Reddy, M., Osuji, R. U., ... Ezema, F. I. (2014). Electrochromic and electrochemical capacitive properties of tungsten oxide and its polyaniline nanocomposite films obtained by chemical bath deposition method. *Electrochimica Acta*, *128*, 218–225.

Obodo, R. M., Chime, U., Nkele, A. C., Nwanya, A. C., Bashir, A., Madiba, I., ... others (2021). Effect of annealing on hydrothermally deposited co3o4-zno thin films for supercapacitor applications. *Materials Today: Proceedings*, *36*, 374–378.

Obodo, R. M., Nsude, H. E., Ezike, S. C., Anosike, J. N., Ugwuanyi, S. E., Eze, C. U., ... Ahmad, I. (2025). Exploring the potential of co3o4@ mno2@ zno enhanced with vitex doniana leaf extract for supercapacitor electrode applications. *Nano-Horizons: Journal of Nanosciences and Nanotechnologies*, *4*, 26–pages.

Obodo, R. M., Nwanya, A. C., Arshad, M., Iroegbu, C., Ahmad, I., Osuji, R. U., ... Ezema, F. I. (2020). Conjugated nio-zno/go nanocomposite powder for applications in supercapacitor electrodes material. *International Journal of Energy Research*, *44*(4), 3192–3202.

Oyedotun, K. O., Ighalo, J. O., Amaku, J. F., Olisah, C., Adeola, A. O., Iwuozor, K. O., ... Adegoke, K. A. (2023). Advances in supercapacitor development: materials, processes, and applications. *Journal of Electronic Materials*, *52*(1), 96–129.

Pal, B., Yang, S., Ramesh, S., Thangadurai, V., & Jose, R. (2019). Electrolyte selection for supercapacitive devices: a critical review. *Nanoscale advances*, *1*(10), 3807–3835.

Palagonia, M. S., Erinmwingbovo, C., Brogioli, D., & La Mantia, F. (2019). Comparison between cyclic voltammetry and differential charge plots from galvanostatic cycling. *Journal of Electroanalytical Chemistry*, *847*, 113170.

Peringath, A. R., Bayan, M. A., Beg, M., Jain, A., Pierini, F., Gadegaard, N., ... Manjakkal, L. (2023). Chemical synthesis of polyaniline and polythiophene electrodes with excellent performance in supercapacitors. *Journal of Energy Storage*, *73*, 108811.

Picollo, M., Aceto, M., & Vitorino, T. (2019). Uv-vis spectroscopy. *Physical sciences reviews*, *4*(4), 20180008.

Pipitone, E., & Vitale, G. (2020). A regenerative braking system for internal combustion engine vehicles using supercapacitors as energy storage elements-part 1: System analysis and modelling. *Journal of Power Sources*, *448*, 227368.

Prabukumar, C., Sadiq, M. M. J., Bhat, D. K., & Bhat, K. U. (2019). Sno2 nanoparticles functionalized mos2 nanosheets as the electrode material for supercapacitor applications. *Materials Research Express*, *6*(8), 085526.

Prasanna, B., Avadhani, D., Muralidhara, H., Chaitra, K., Thomas, V. R., Revanasiddappa, M., & Kathyayini, N. (2016). Synthesis of polyaniline/zro2 nanocomposites and their performance in ac conductivity and electrochemical supercapacitance. *Bulletin of materials science*, *39*(3), 667–675.

Prasanna, B., Avadhani, D., Raj, V., Kumar, K. Y., & Raghu, M. (2019). Fabrication of pani/sno2 hybrid nanocomposites via interfacial polymerization for high performance supercapacitors applications. *Surface Engineering and Applied Electrochemistry*, *55*(4), 463–471.

Qin, Z., Xu, Y., Liu, L., Liu, M., Zhou, H., Xiao, L., ... Chen, C. (2022). Ni-mof composite polypyrrole applied to supercapacitor energy storage. *RSC advances*, *12*(45), 29177–29186.

Rafique, A., Zubair, U., Serrapede, M., Fontana, M., Bianco, S., Rivolo, P., ... Lamberti, A. (2020). Binder free and flexible asymmetric supercapacitor exploiting mn3o4 and mos2 nanoflakes on carbon fibers. *Nanomaterials*, *10*(6), 1084.

Rahman, M. M., Joy, P. M., Uddin, M. N., Mukhlish, M. Z. B., & Khan, M. M. R. (2021). Improvement of capacitive performance of polyaniline based hybrid supercapacitor. *Heliyon*, *7*(7).

Rajkumar, C. M. P., Ezhilarasi. (2022). Fabrication of cowo4/pani composite as electrode material for energy storage applications. *Journal of Physics and Chemistry of Solids*, *162*, 110500.

Ramanathan, G., & Murali, K. (2022). Photocatalytic activity of sno2 nanoparticles. *Journal of Applied Electrochemistry*, *52*(5), 849–859.

Rand, D. (1997). The lead/acid battery—a key technology for global energy management. *Journal of power sources*, *64*(1-2), 157–174.

Rao, M. M., Jayalaksmi, M., Reddy, B. R., Madhavendra, S., & Kantam, M. L. (2005). Recognizing nano sno as an electrode material for electrochemical double layer capacitors. *Chemistry letters*, *34*(5), 712–713.

Reddy, A. L. M., & Ramaprabhu, S. (2007). Nanocrystalline metal oxides dispersed multiwalled carbon nanotubes as supercapacitor electrodes. *The Journal of Physical Chemistry C*, *111*(21), 7727–7734.

Ren, S., Yang, Y., Xu, M., Cai, H., Hao, C., & Wang, X. (2014). Hollow sno2 microspheres and their carbon-coated composites for supercapacitors. *Colloids and Surfaces A: Physicochemical and Engineering Aspects*, *444*, 26–32.

Roohi, Z., Mighri, F., & Zhang, Z. (2024). Conductive polymer-based electrodes and supercapacitors: Materials, electrolytes, and characterizations. *Materials*, *17*(16), 4126.

Roy, H. S., Islam, M. M., Mollah, M. Y. A., & Susan, M. A. B. H. (2020). Polyaniline-mno2 composites prepared in-situ during oxidative polymerization of aniline for supercapacitor applications. *Materials Today: Proceedings*, *29*, 1013–1019.

Sagadevan, S., Marlinda, A., Chowdhury, Z. Z., Wahab, Y. B. A., Hamizi, N. A., Shahid, M., ... Johan, M. R. (2021). Fundamental electrochemical energy storage systems. In *Advances in supercapacitor and supercapattery* (pp. 27–43). Elsevier.

Sajjad, M., Asif, S. U., Guan, L., Jiao, Y., Jiang, Y., Zhang, L., ... others (2021). Bismuth yttrium oxide (bi3yo6), a new electrode material for asymmetric aqueous supercapacitors. *Journal of Inorganic and Organometallic Polymers and Materials*, *31*(3), 1260–1270.

Sakaushi, K., Oaki, Y., Uchiyama, H., Hosono, E., Zhou, H., & Imai, H. (2010). Synthesis and applications of sno nanosheets: parallel control of oxidation state and nanostructure through an aqueous solution route. *Small*, *6*(6), 776–781.

Sakita, A. M., Della Noce, R., & Lavall, R. L. (2021). Potential-dependent electrochemical impedance spectroscopy as a powerful tool for evaluating supercapacitor electrode performance. *Journal of The Electrochemical Society*, *168*(8), 080525.

Saleem, A. M., Desmaris, V., & Enoksson, P. (2016). Performance enhancement of carbon nanomaterials for supercapacitors. *Journal of Nanomaterials*, *2016*(1), 1537269.

Sanches, E. A., Carolino, A. d. S., Santos, A. L. d., Fernandes, E. G., Trichês, D. M., & Mascarenhas, Y. P. (2015). The use of le bail method to analyze the semicrystalline pattern of a nanocomposite based on polyaniline emeraldine-salt form and α-al2o3. *Advances in Materials Science And Engineering*, *2015*(1), 375312.

Sangiorgi, N., Aversa, L., Tatti, R., Verucchi, R., & Sanson, A. (2017). Spectrophotometric method for optical band gap and electronic transitions determination of semiconductor materials. *Optical Materials*, *64*, 18–25.

San Martin, I., San Martin, J., Aperribay, V., & Eguia, P. (2011). European association for the development of renewable energies. *Environment and Power Quality, Energy Storage Technologies for Electric Applications, Spain*.

Selvamani, T., Anandan, S., Granone, L., Bahnemann, D. W., & Ashokkumar, M. (2018). Phase-controlled synthesis of bismuth oxide polymorphs for photocatalytic applications. *Materials Chemistry Frontiers*, *2*(9), 1664–1673.

Seman, R., Azam, M., Mohamed, M., & Ani, M. (2022). Effect of polytetrafluoroethylene binder content on gravimetric capacitance and life cycle stability of graphene supercapacitor. *International Journal of Automotive & Mechanical Engineering*, *19*(3).

Shah, M. Z. U., Feng, J., Shah, A., Sajjad, M., Tirth, V., & Shah, M. S. (2025). Wet-chemical synthesis of sno2-co3o4 microflower electrode for high energy density in aqueous asymmetric supercapacitors. *Journal of Energy Storage*, *108*, 115081.

Shaikh, Z. A., Shinde, P. V., Shaikh, S. F., Al-Enizi, A. M., & Mane, R. S. (2020). Facile synthesis of bi2o3@ mno2 nanocomposite material: A promising electrode for high performance supercapacitors. *Solid State Sciences*, *102*, 106158.

Shan, D., Zhang, J., Xue, H.-G., Zhang, Y.-C., Cosnier, S., & Ding, S.-N. (2009). Polycrystalline bismuth oxide films for development of amperometric biosensor for phenolic compounds. *Biosensors and Bioelectronics*, *24*(12), 3671–3676.

Sharma, P., & Bhatti, T. (2010). A review on electrochemical double-layer capacitors. *Energy conversion and management*, *51*(12), 2901–2912.

Sharma, S., & Chand, P. (2023). Supercapacitor and electrochemical techniques: A brief review. *Results in Chemistry*, *5*, 100885.

Sheoran, K., Thakur, V. K., & Siwal, S. S. (2022). Synthesis and overview of carbon-based materials for high performance energy storage application: A review. *Materials Today: Proceedings*, *56*, 9–17.

Shinde, P. V., Ghule, B. G., Shaikh, S. F., Shinde, N. M., Sangale, S. S., Jadhav, V., ... Mane, R. S. (2019). Microwave-assisted hierarchical bismuth oxide worm-like nanostructured films as room-temperature hydrogen gas sensors. *Journal of Alloys and Compounds*, *802*, 244–251.

Shulga, Y. M., Baskakov, S., Smirnov, V., Shulga, N. Y., Belay, K., & Gutsev, G. (2014). Graphene oxide films as separators of polyaniline-based supercapacitors. *Journal of Power Sources*, *245*, 33–36.

Simon, P., Taberna, P.-L., & Béguin, F. (2013). Electrical double-layer capacitors and carbons for edlcs. *Edited by Francois Béguin and Elzbieta Fr şackowiak*.

Singh, S., Sahoo, R. K., Shinde, N. M., Yun, J. M., Mane, R. S., & Kim, K. H. (2019). Synthesis of bi2o3-mno2 nanocomposite electrode for wide-potential window high performance supercapacitor. *Energies*, *12*(17), 3320.

Sk, M., Pradhan, P., Patra, B., & Guria, A. (2023). Green biomass derived porous carbon materials for electrical double-layer capacitors (edlcs). *Materials Today Chemistry*, *30*, 101582.

Soam, A., Kumar, R., Singh, B. K., & Saini, D. S. (2025). A comprehensive review on synthesis of nanocomposites for supercapacitor. *Journal of Inorganic and Organometallic Polymers and Materials*, 1–29.

Soam, A., Kumar, R., Singh, M., Thatoi, D., Dusane, R. O., et al. (2020). Development of paper-based flexible supercapacitor: bismuth ferrite/graphene nanocomposite as an active electrode material. *Journal of Alloys and Compounds*, *813*, 152145.

Srinivasan, R., Elaiyappillai, E., Anandaraj, S., kumar Duvaragan, B., & Johnson, P. M. (2020). Study on the electrochemical behavior of bivo4/pani composite as a high performance supercapacitor material with excellent cyclic stability. *Journal of Electroanalytical Chemistry*, *861*, 113972.

Srivastava, G., Dalela, S., Gautam, N. K., Kumar, S., Hashmi, S., Ahmad, M. A., ... others (2025). Synthesis and characterizations of mno2/cnt nanocomposite for usage as electrodes in high-performance supercapacitor. *Nano Trends*, *9*, 100067.

Sun, W., Xiao, L., & Wu, X. (2019). Facile synthesis of nio nanocubes for photocatalysts and supercapacitor electrodes. *Journal of Alloys and Compounds*, *772*, 465–471.

Sunil, V., Pal, B., Misnon, I. I., & Jose, R. (2021). Characterization of supercapacitive charge storage device using electrochemical impedance spectroscopy. *Materials Today: Proceedings*, *46*, 1588–1594.

Suthakaran, S., Dhanapandian, S., Krishnakumar, N., & Ponpandian, N. (2019). Hydrothermal synthesis of sno2 nanoparticles and its photocatalytic degradation of methyl violet and electrochemical performance. *Materials Research Express*, *6*(8), 0850i3.

Teli, A. M., Bhat, T. S., Beknalkar, S. A., Mane, S. M., Chaudhary, L. S., Patil, D. S., ... Shin, J. C. (2022). Bismuth manganese oxide based electrodes for asymmetric coin cell supercapacitor. *Chemical Engineering Journal*, *430*, 133138.

Tomboc, G. M., & Kim, H. (2019). Derivation of both edlc and pseudocapacitance characteristics based on synergistic mixture of nico2o4 and hollow carbon nanofiber: an efficient electrode towards high energy density supercapacitor. *Electrochimica Acta*, *318*, 392–404.

Trindade, T. N., & Silva, L. A. (2018). Cd-doped sno2/cds heterostructures for efficient application in photocatalytic reforming of glycerol to produce hydrogen under visible light irradiation. *Journal of Alloys and Compounds*, *735*, 400–408.

Trivedi, H., Verma, K. D., Sinha, P., & Kar, K. K. (2021). Current collector material selection for supercapacitors. In *Handbook of nanocomposite supercapacitor materials iii: Selection* (pp. 271–311). Springer.

Uddin, M. T., Mukhlish, M. Z. B., & Patwary, M. R. H. (2021). A novel magnetically separable cofe2o4/sno2 composite photocatalyst for the degradation of methylene blue dye from aqueous solution. *Desalination and Water Treatment*, *212*, 311–322.

Vadiraj, K., & Belagali, S. (2015). Characterization of polyaniline for optical and electrical properties. *IOSR J. Appl. Chem*, *8*(1), 53–56.

Vaghela, P., Pandey, V., Sircar, A., Yadav, K., Bist, N., & Kumari, R. (2023). Energy storage techniques, applications, and recent trends: A sustainable solution for power storage. *MRS Energy & Sustainability*, *10*(2), 261–276.

Varshney, B., Siddiqui, M., Anwer, A. H., Khan, M. Z., Ahmed, F., Aljaafari, A., ... Azam, A. (2020). Synthesis of mesoporous sno2/nio nanocomposite using modified sol–gel method and its electrochemical performance as electrode material for supercapacitors. *Scientific reports*, *10*(1), 11032.

Veerakumar, P., Sangili, A., Manavalan, S., Thanasekaran, P., & Lin, K.-C. (2020). Research progress on porous carbon supported metal/metal oxide nanomaterials for supercapacitor electrode applications. *Industrial & Engineering Chemistry Research*, *59*(14), 6347–6374.

Velmurugan, V., Srinivasarao, U., Ramachandran, R., Saranya, M., & Grace, A. N. (2016). Synthesis of tin oxide/graphene (sno2/g) nanocomposite and its electrochemical properties for supercapacitor applications. *Materials Research Bulletin*, *84*, 145–151.

Verma, K. D., Sinha, P., Banerjee, S., & Kar, K. K. (2020). Characteristics of current collector materials for supercapacitors. In *Handbook of nanocomposite supercapacitor materials i: Characteristics* (pp. 327–340). Springer.

Vinayaraj, S., Brijesh, K., Dhanush, P., & Nagaraja, H. (2020). Znwo4/sno2 composite for supercapacitor applications. *Physica B: Condensed Matter*, *596*, 412369.

Virji, S., Huang, J., Kaner, R. B., & Weiller, B. H. (2004). Polyaniline nanofiber gas sensors: examination of response mechanisms. *Nano letters*, *4*(3), 491–496.

Wang, Chen, L., Yan, B., Wang, C., Zhu, F., Jiang, X., ... Yang, G. (2014). In situ preparation of sno 2@ polyaniline nanocomposites and their synergetic structure for high-performance supercapacitors. *Journal of Materials Chemistry A*, *2*(22), 8334–8341.

Wang, H., MacDiarmid, A., Wang, Y., Gebier, D., & Epstein, A. (1996). Application of polyaniline (emeraldine base, eb) in polymer light-emitting devices. *Synthetic Metals*, *78*(1), 33–37.

Wang, H.-W., Hu, Z.-A., Chang, Y.-Q., Chen, Y.-L., Lei, Z.-Q., Zhang, Z.-Y., & Yang, Y.-Y. (2010). Facile solvothermal synthesis of a graphene nanosheet–bismuth oxide composite and its electrochemical characteristics. *Electrochimica Acta*, *55*(28), 8974–8980.

Wang, Y., & Lee, J. Y. (2005). Microwave-assisted synthesis of sno2–graphite nanocomposites for li-ion battery applications. *Journal of power sources*, *144*(1), 220–225.

Wang, Z., Liu, S., Cao, X., Wu, S., Liu, C., Li, G., ... Ding, W. (2020). Preparation and characterization of tio2 nanoparticles by two different precipitation methods. *Ceramics International*, *46*(10), 15333–15341.

Wei, D., Kumar, Zhang, L., & Li, J.-F. (2025). Pseudocapacitive materials for energy storage: properties, mechanisms, and applications in supercapacitors and batteries. *Frontiers in Chemistry*, *13*, 1636683.

Wei, T.-T., Wu, Y.-R., Zhao, Y.-S., Zhang, J.-H., Zhu, Y.-R., & Yi, T.-F. (2021). Boosting the li storage performances of bi5nb3o15@ ceo2 composite anode for lithium-ion batteries. *Surface and Coatings Technology*, *423*, 127580.

Wu, F., Wang, X., Gao, H., Hao, C., Ge, C., et al. (2017). Synthesis and characterization of hierarchical bi2moo6/polyaniline nanocomposite for all-solid-state asymmetric supercapacitor. *Electrochimica Acta*, *245*, 685–695.

Wu, H.-C., Lin, Y.-P., Lee, E., Lin, W.-T., Hu, J.-K., Chen, H.-C., & Wu, N.-L. (2009). High-performance carbon-based supercapacitors using al current-collector with conformal carbon coating. *Materials Chemistry and Physics*, *117*(1), 294–300.

Wu, P., Feng, L., Liang, Y., Zhang, X., Li, X., Tian, S., ... Khan, S. (2020). Large-scale synthesis of 2d bismuth-enriched bismuth oxyiodides at low temperatures for high-performance supercapacitor and photocatalytic applications. *Journal of Materials Science: Materials in Electronics*, *31*(7), 5385–5401.

Wu, Q., He, T., Zhang, Y., Zhang, J., Wang, Z., Liu, Y., ... Ran, F. (2021). Cyclic stability of supercapacitors: materials, energy storage mechanism, test methods, and device. *Journal of Materials Chemistry A*, *9*(43), 24094–24147.

Xavier, F. F., Bruziquesi, C. G., Fagundes, W. S., Matsubara, E. Y., Rosolen, J. M., Silva, A. C., ... Amaral, F. A. (2019). New synthesis method for a core-shell composite based on α-bi 2 o 3@ ppy and its electrochemical behavior as supercapacitor electrode. *Journal of the Brazilian Chemical Society*, *30*, 727–735.

Xi, L., Qian, D., Tang, X., & Chen, C. (2008). High surface area sno2 nanoparticles: Synthesis and gas sensing properties. *Materials Chemistry and Physics*, *108*(2-3), 232–236.

Xiao, B.-H., Xiao, K., Li, J.-X., Xiao, C.-F., Cao, S., & Liu, Z.-Q. (2024). Flexible electrochemical energy storage devices and related applications: recent progress and challenges. *Chemical Science*, *15*(29), 11229–11266.

Xiao, H., Yao, S., Qu, F., Zhang, X., & Wu, X. (2017). Electrochemical energy storage performance of heterostructured sno2@ mno2 nanoflakes. *Ceramics International*, *43*(2), 1688–1694.

Xie, Y., & Ji, J. (2016). Synthesis and capacitance performance of mno2/rgo double-shelled hollow microsphere. *Journal of Materials Research*, *31*(10), 1423–1432.

Xing, F., Bi, Z., Su, F., Liu, F., & Wu, Z.-S. (2022). Unraveling the design principles of battery-supercapacitor hybrid devices: From fundamental mechanisms to microstructure engineering and challenging perspectives. *Advanced Energy Materials*, *12*(26), 2200594.

Yang, D. (2012). Application of nanocomposites for supercapacitors: characteristics and properties. *Nanocomposites-New Trends Dev*, 299–328.

Yang, W.-D., & Yu-Jiang, L. (2019). Preparation of rgo/bi2o3 composites by hydrothermal synthesis for supercapacitor electrode. *Journal of Electrical Engineering*, *70*(7S), 101–106.

Yin, H., Li, Q., Cao, M., Zhang, W., Zhao, H., Li, C., ... Zhu, M. (2017). Nanosized-bismuth-embedded 1d carbon nanofibers as high-performance anodes for lithium-ion and sodium-ion batteries. *Nano Research*, *10*(6), 2156–2167.

Yu, & Chen, G. (2020). Supercapatteries as high-performance electrochemical energy storage devices. *Electrochemical Energy Reviews*, *3*(2), 271–285.

Yu, G., Xie, X., Pan, L., Bao, Z., & Cui, Y. (2013). Hybrid nanostructured materials for high-performance electrochemical capacitors. *Nano Energy*, *2*(2), 213–234.

Zamiri, G., Haseeb, A. M. A., Jagadish, P., Khalid, M., Kong, I., & Krishnan, S. G. (2022). Three-dimensional graphene–tio2–sno2 ternary nanocomposites for high-performance asymmetric supercapacitors. *ACS omega*, *7*(48), 43981–43991.

Zhang, J., Cui, Y., & Shan, G. (2019). Metal oxide nanomaterials for pseudocapacitors. *arXiv preprint arXiv:1905.01766*.

Zhang, L. L., Zhou, R., & Zhao, X. (2010). Graphene-based materials as supercapacitor electrodes. *Journal of Materials Chemistry*, *20*(29), 5983–5992.

Zhang, T., He, W., Zhang, W., Wang, T., Li, P., Sun, Z., & Yu, X. (2020). Designing composite solid-state electrolytes for high performance lithium ion or lithium metal batteries. *Chemical Science*, *11*(33), 8686–8707.

Zhang, Y., Liu, M., Sun, S., & Yang, L. (2020). The preparation and characterization of sno2/rgo nanocomposites electrode materials for supercapacitor. *Advanced Composites Letters*, *29*, 2633366X20909839.

Zhang, Z., Liu, J., Gu, J., Su, L., & Cheng, L. (2014). An overview of metal oxide materials as electrocatalysts and supports for polymer electrolyte fuel cells. *Energy & Environmental Science*, *7*(8), 2535–2558.

Zhang, Z. J., Zheng, Q. C., & Sun, L. (2017). Synthesis of 2-d nanostructured bivo4: Ag hybrid as an efficient electrode material for supercapacitors. *Ceramics International*, *43*(18), 16217–16224.

Zhu, J., Wu, Q., & Li, J. (2020). Review and prospect of mn3o4-based composite materials for supercapacitor electrodes. *ChemistrySelect*, *5*(33), 10407–10423.